DISCRETE FREQUENCY MID-INFRARED SPECTROSCOPIC IMAGING USING QUANTUM CASCADE LASERS

BY

KEVIN YEH

DISSERTATION

Submitted in partial fulfillment of the requirements
for the degree of Doctor of Philosophy in Bioengineering
in the Graduate College of the
University of Illinois at Urbana-Champaign, 2019

Urbana, Illinois

Doctoral Committee:

Professor Rohit Bhargava, Chair
Professor Joseph Maria Kumar Irudayaraj
Associate Professor Dipanjan Pan
Professor Andre Kajdacsy-Balla, University of Illinois at Chicago

ABSTRACT

Infrared (IR) spectroscopic imaging is an analytical technique that directly images the spatial distribution of chemical components within a sample in the absence of external contrast agents. This is especially advantageous with biological samples where the mid to far-infrared wavelength range corresponds with the vibrational modes of functional groups in many organic molecules. In recent years, the technology enabling discrete frequency infrared (DFIR) spectroscopic microscopy has undergone many substantive changes due to rapid developments in quantum cascade lasers (QCL) in terms of their output power, beam stability, and wavelength tuning range. In this dissertation, we present the research and development of several state-of-the-art microscopy systems that have advanced what was previously possible with industry standard instruments. Through drastic improvements in imaging speed and resolution, as well as reductions in noise and aberrations, our systems serve as a flexible platform with capabilities that open new avenues for research and clinical interests.

COPYRIGHT

Yeh, K.; Reddy, R. K.; Bhargava, R. Fourier Transform Infrared Spectroscopic Imaging: An Emerging Label-Free Approach for Molecular Imaging. In *Emerging Imaging Technologies in Medicine*; Anastasio, M. A., La Rivière, P. J., Eds.; Taylor & Francis: Boca Raton, FL, **2012**; pp 303–319.

Yeh, K.; Schulmerich, M.; Bhargava, R. Mid-Infrared Microspectroscopic Imaging with a Quantum Cascade Laser. In *SPIE*; Druy, M. A., Crocombe, R. A., Eds.; **2013**; Vol. 8726, p 87260E.

Yeh, K.; Kenkel, S.; Liu, J.-N.; Bhargava, R. Fast Infrared Chemical Imaging with a Quantum Cascade Laser. *Anal. Chem.* **2015**, *87* (1), 485–493.

Yeh, K.; Bhargava, R. Discrete Frequency Infrared Imaging Using Quantum Cascade Lasers for Biological Tissue Analysis. In *SPIE*; Mahadevan-Jansen, A., Petrich, W., Eds.; **2016**; Vol. 9704, p 970406.

Mittal, S.*; **Yeh, K.***; Leslie, L. S.; Kenkel, S.; Kajdacsy-Balla, A.; Bhargava, R. Simultaneous Cancer and Tumor Microenvironment Subtyping Using Confocal Infrared Microscopy for All-Digital Molecular Histopathology. *Proc. Natl. Acad. Sci.* **2018**, *115* (25), E5651–E5660.

Yeh, K.; Lee, D.; Bhargava, R. Multicolor Discrete Frequency Infrared Spectroscopic Imaging. *Anal. Chem.* **2019**, *91* (3), 2177–2185.

TABLE OF CONTENTS

CHAPTER 1: **INTRODUCTION**

Infrared spectroscopic imaging is an analytical technique that provides the spatially resolved infrared absorption spectrum of a sample. It is a promising form of chemical imaging that is well suited for the analysis of biological tissues, being capable revealing important molecular information without the need for stains or dyes. In conjunction with machine learning algorithms, these instruments can provide objective and automated evaluations to aid pathologists improve diagnostic accuracy. Despite these benefits, clinical translation of this technology has been hindered by impractical instrument performance. Current industry standard spectroscopic imaging microscopes can take weeks to image a tissue biopsy's full spectral profile at high resolution, after which the clinical utility of the results becomes uncertain. However, every single spectral data point is often not required to extract useful information from a sample. Measurements of only the data required for analyses drastically reduces the acquisition time and computational costs, representing the unique advantage of discrete frequency (DF) imaging. With traditional extended frequency thermal sources coupled to monochromators, these dispersive infrared instruments suffered from a lack of signal intensity and excessive noise when narrowing the spectral linewidth. Thus, Fourier transform spectroscopy (FT-IR) became dominant due to their spectral multiplexing capabilities and light throughput advantages.

The quantum cascade laser (QCL), with high intensity and narrowband emission, enables competitive discrete frequency approaches by drastically increasing imaging speeds with superior spatial and spectral resolution. The earliest iterations of QCL microscope (QCLM) straightforwardly mated a QCL to an infrared microscope originally developed for FT-IR. Over time, we have purposefully designed newer generations of QCLM to suit the unique characteristics of laser sources. These advanced QCLM typically consist of four individual tuner modules with beams combined into a single collinear output spanning the mid-infrared fingerprint region from 770-1940 cm^{-1}. We have coupled these lasers with optics, electronics and software, many of which has been custom-designed in-house to provide a platform with rapid high-quality imaging performance. In this dissertation, we present the progress of QCLM development to date over several generations, resulting in novel instrumentation that allows for chemical imaging in days as opposed to months with conventional systems with excellent image quality, imaging speed, and flexibility of scale.

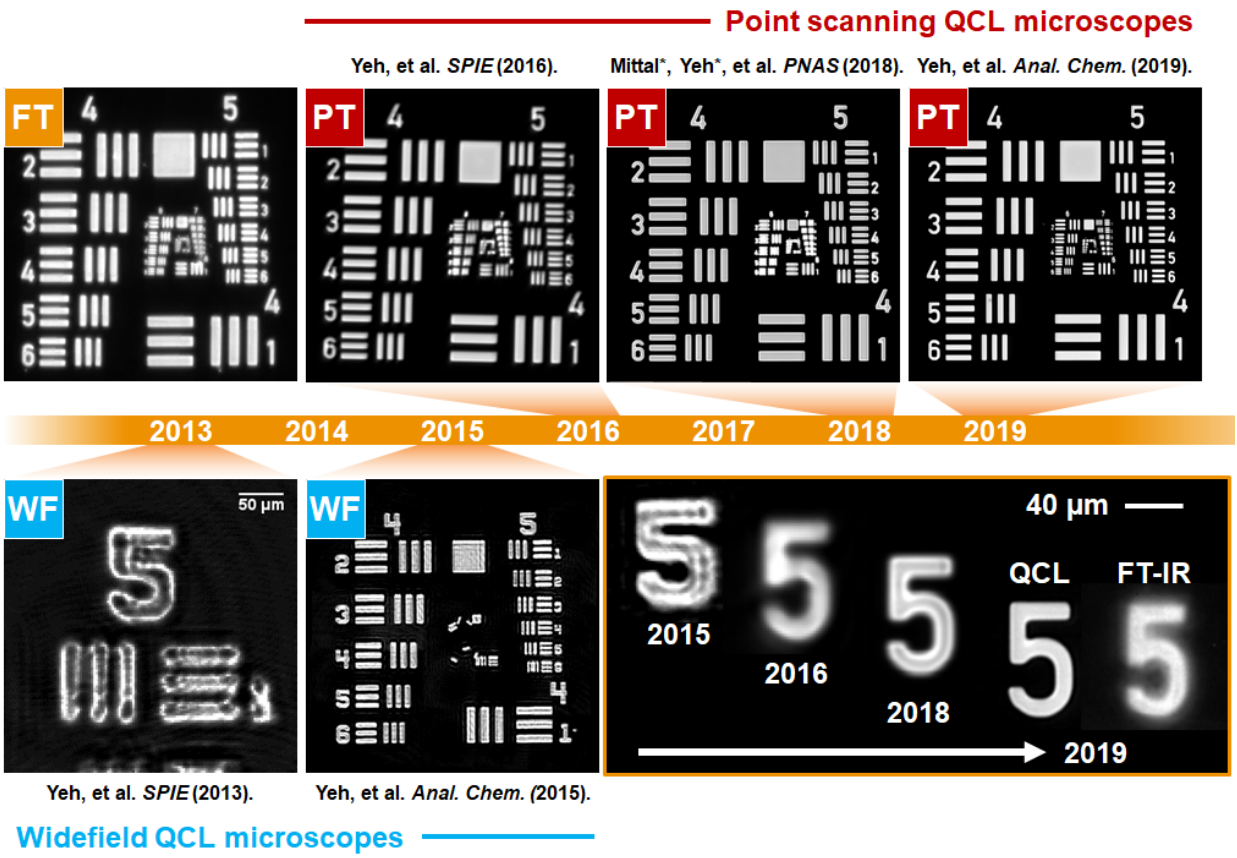

Figure 1.1. Progression of QCL microscopes developed in this manuscript.

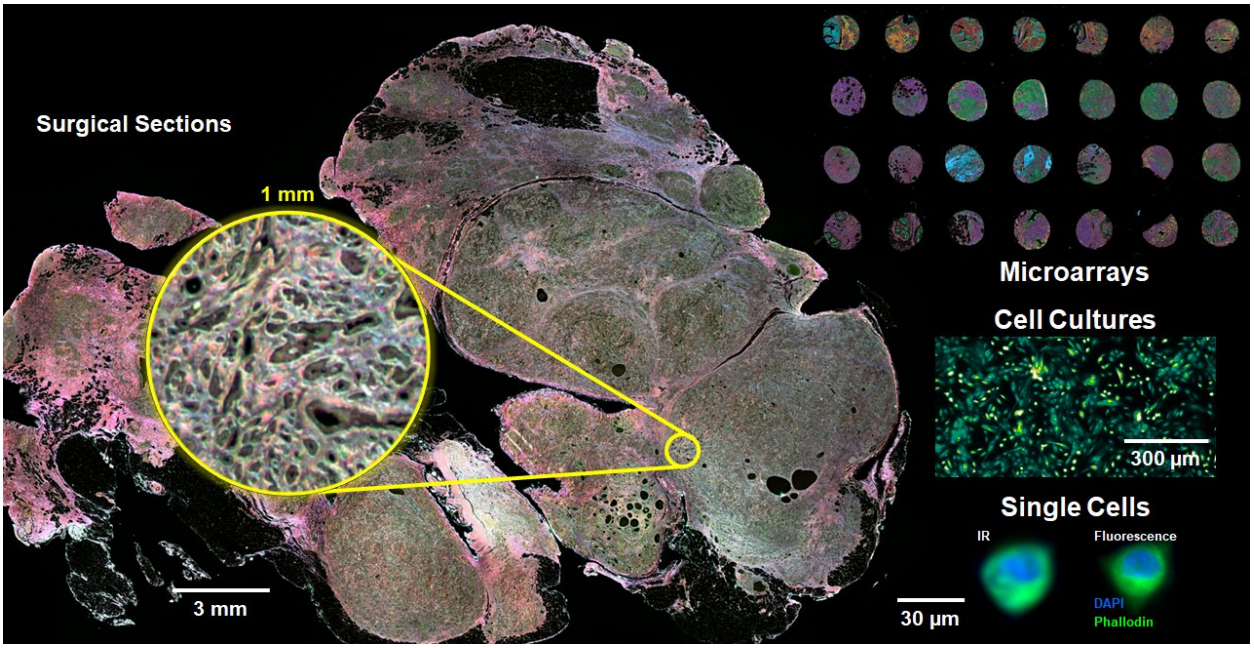

Figure 1.2. Summary of capabilities.

CHAPTER 2: FOURIER TRANSFORM INFRARED SPECTROSCOPIC IMAGING [*]

2.1 Introduction

Fourier transform infrared (FT-IR) spectroscopy is a widely-used technique for measuring the chemical composition of a sample. Different functional groups in molecules have resonant frequencies in the mid-IR spectral range and will absorb light corresponding to their resonant frequencies. The absorption spectrum of a molecule, hence, acts as its chemical signature and will contain contributions from each of the different functional groups constituting the molecule. Even when a mixture of complex composition is used, the chemically-specific spectrum is often termed a "molecular fingerprint" of the material. While the practice of FT-IR spectroscopy is over 100 years old, there has been a recent renaissance in theoretical understanding, instrumentation and applications that has generated considerable interest in scientific study and applications in this area. In particular, coupling infrared spectroscopy with microscopy has significantly advanced with the availability of array detectors. This combination of spectroscopy, microscopy and multichannel detection is often referred to as FT-IR spectroscopic imaging[1] or FT-IR imaging. Since the primary contrast mechanism in FT-IR imaging is intrinsic, molecular and quantitative, it alleviates the need for external contrast agents or chemicals. Consequently they have found a wide variety of applications including those in forensics, cancer histopathology, polymer science, drug diffusion studies, art restoration, and tissue engineering. The fundamentals of instrumentation, theory and applications have been presented in this work.

2.2 History

The theoretical discoveries enabling modern FT-IR spectroscopy and imaging were developed primarily over the past 40 years. In the prior dispersive spectroscopic technology, a prism was used to separate the frequencies in the light source and a small grating would select a

[*] The work in this chapter has previously been published and is partially reprinted with permission here in abbreviated form. Please refer to the citation for the full manuscript.

Yeh, K.; Reddy, R. K.; Bhargava, R. Fourier Transform Infrared Spectroscopic Imaging: An Emerging Label-Free Approach for Molecular Imaging. In *Emerging Imaging Technologies in Medicine*; Anastasio, M. A., La Rivière, P. J., Eds.; Taylor & Francis: Boca Raton, FL, **2012**; pp 303–319.

specific wavelength of light. The resulting monochromatic beam was shone through a sample and the amount of light absorbed was measured. Then the grating would be shifted and the measurement repeated for each individual wavelength. In 1948, P. Jacquinot discovered that the energy throughput using an interferometer is much higher than what could be realized in the dispersive spectrometer where the light intensity is restricted by the slits of the optical grating.[2] This is called the Jacquinot or throughput advantage. By replacing the grating with an interferometer, FT-IR spectrometers have an increased sensitivity of roughly 60 fold for the same resolving power and instrument size. In 1949, a discovery by P.B. Fellgett, now referred to as the Felgett or multiplex advantage, showed that the signal intensity at multiple wavelengths could be simultaneously measured when the interferogram is deconstructed using a Fourier transform. However, a Fourier transform of a spectrum consisting tens of thousands of data points was a prohibitively slow process at that time.

The fast Fourier transform (FFT) algorithm developed by Cooley and Tukey in 1965 dramatically decreased the computational requirements for performing a Fourier transform making modern day FT-IR spectroscopy practical. The combination of the aforementioned three insights allowed an interferometer based spectrometer to achieve SNR comparable to a dispersive instrument while significantly reducing the measurement time. In the ensuing years, interferometers being developed typically involved various configurations of stationary or scanning paradigms. Most stationary interferometers are based on the Sagnac.[3] The beam is split and made to travel in different directions along a common closed loop path. In one example developed by Okamoto et al, the angles of the mirrors along the common path are arranged to disperse the beam such that they form an interferogram upon recombination at the beam splitter.[4] This interferogram is then focused onto a linear array detector. Although this design has the advantage of having no moving parts, it is not as stable as scanning interferometers since the generation of the interferogram is extremely sensitive to the angle of the mirrors along the path. Furthermore, the resolution of the interferogram is limited by the number of detector elements in the array.

Most scanning interferometers using for spectroscopy are based on the basic design by Michelson (details presented in the next section). The vast majority of commercial instruments are based on this design. Cube-corner interferometers were designed to compensate for mirror tilt effects by ensuring that the reflected beam is always parallel to the incident beam and are used in

some commercial implementations. Their performance is nearly identical to a well-aligned basic Michelson interferometer. There are also other designs that may have specific advantages but are not routinely commercially available. Refractively scanned interferometers use prisms in the place of the plane mirrors in order to increase the optical path difference. Lamellar grating interferometers reflect light off of a surface consisting of adjustable parallel interleaved mirrors, where the optical path difference is dependent on the shift between the mirror facets. Interferometers have also been designed to take advantage of polarization, where an optical path difference is introduced by rotating a rocking mirror. The reliability of many of these designs depends heavily on the accuracy of movement of the reference mirror. Other designs have been proposed to be stable or scan rapidly. Precision electromotors and advanced control via computers, however, have made Michelson interferometers the preferred design in modern FT-IR spectroscopy.

While IR spectroscopy technology was developing, significant efforts were also expended in developing IR microscopy. The combination of a microscope and IR spectrometer was reported more than 60 years ago.[5] The instrument, however, relied on dispersion of light and collected on spectral element at a time for one spatial position. To acquire a spectrum at every point, the spectrum at every spatial position had to be serially recorded and the sample had to be raster scanned across many positions, making data acquisition very slow and impractical for most uses. Microscopy is challenging as light throughput for a small spatial region is necessarily small. As opposed to many other optical imaging techniques, mid-IR lasers for the broadband spectra regions were not developed. Hence, only weak thermal sources were available. Since the spectral region was not driven by either consumer demand or visible imaging, detector development was also slow. Hence, microscopy did not make much progress until the advent of FT-IR spectroscopy, better detectors and microcomputer control and processing. Coupling a microscope to an FT-IR spectrometer resulted in significant speed advantages but was commercially available only in the late 80s. The sample was still raster scanned to collect spatial data. The late 90s saw the introduction of wide-field detection with focal plane array (FPA) detectors that were de-classified from military applications.[6] The tremendous multichannel advantage imparted by array detectors provided a speed advantage over the previous point-by-point mapping technology.[7] To distinguish the multichannel detection-based instruments from the point-scanning instruments, the latter are referred to as “imaging” techniques, while the

former are termed “mapping” techniques. A second generation of detectors – both linear array and revamped focal plane arrays – provided further advances in the early 2000s. The period since then was dominated by various applications and data analysis methods. Lately, a focus on quantitative and fundamental understanding has driven both instrumentation and applications. For example, the use of high numerical aperture optics coupled with optimized data sampling has enabled high definition FT-IR spectroscopic imaging.[8–11] These developments have fueled and are re-energizing the use of FT-IR spectroscopic imaging in a wide array of fields including polymeric materials,[12] forensics,[13] art restoration,[14] and tissue histopathology.[15]

2.3 Theory

The spectral diversity and unique light-matter interactions in the mid-IR spectral range both make the theoretical underpinnings and its effect on instrument design interesting for IR microscopy. In this section, we first present the basic theory of a Michelson interferometer which helps understand the trade-offs in spectroscopic acquisition and analysis. Next, we discuss optical theory of IR microscopy, which helps understand the spectral response of heterogeneous systems and spectral recording when using a microscope. Combined, the two aspects afford a full understanding of the data acquisition and aid in the interpretation of recorded data.

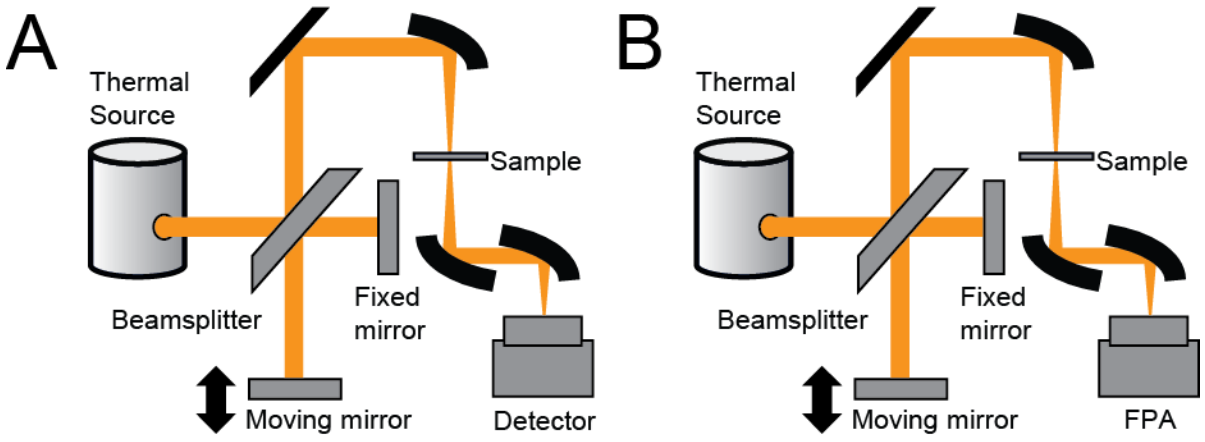

Figure 2.1. Schematic diagram of (A) FT-IR point spectroscopy using far-field apertures, and (B) FT-IR imaging with a multi-element focal plane array (FPA) detector. Note that the interferometer, consisting of the source, beam splitter and mirror with their attendant structural, electrical and control elements are common between instruments and commonly available FT-IR spectrometers. The output of the interferometer is directed to an infrared microscope and detectors can be monolithic or focal plane arrays (FPA).

2.3.1 Interferogram

When two waves propagate along the same path, they interfere with each other, either constructively or destructively depending on their frequency, magnitude, and phase. An interferogram is the signal obtained by superimposing several such waves. In a Michelson interferometer, light for an infrared source is split into two arms using a beam splitter and reflected back to the beam splitter by mirrors in each arm. As opposed to other uses of interferometry, as used in depth ranging for example, this approach has been strictly used for spectral encoding in the mid-IR. The common path of the beam provides for an exceptionally stable signal in which noise sources, including source fluctuations and phase errors among others, that often dominate other applications of interferometry are naturally eliminated. The length of path traversed by light in each arm can be varied by changing the relative positions of the mirrors and the difference in path length is called retardation and denoted by δ. The intensity of light at the detector is recoded as a function of δ and is called an interferogram. The intensity, I, as a function of retardation, δ, for a Michelson interferometer is given by

$$I'(\delta) = 0.5I(\tilde{v}_o)\big(1 + cos(2\pi\tilde{v}_o\delta)\big) \tag{2.1}$$

where $\tilde{v}_o$ is the wavenumber in cm^{-1}. Typically, only the oscillating component (AC signal) is useful for spectrometry and the constant term (average DC signal) is subtracted either in hardware or software. With this simplification, Equation 2.1 can be written as

$$I(\delta) = 0.5I(\tilde{v}_o)cos2\pi\tilde{v}_o\delta \tag{2.2}$$

Instrument parameters including the beam splitter efficiency, detector response, and amplifier characteristics modify the signal and are included into the measurement via a multiplicative term $G(\tilde{v}_o)$.[3] The signal, $S(\delta)$, from the amplifier is

$$S(\delta) = 0.5G(\tilde{v}_o)I(\tilde{v}_o)cos(2\pi\tilde{v}_o\delta) \tag{2.3}$$

All the multiplicative factors can be simplified into the beam spectral intensity, $B(\widetilde{v_o})$ resulting in

$$S(\delta) = B(\tilde{v}_o)cos(2\pi\tilde{v}_o\delta) \tag{2.4}$$

$S(\delta)$ is the Fourier cosine transform of $B(\tilde{v}_o)$. Consequently, the spectrum of the signal can be calculated by computing the inverse Fourier cosine transform of $S(\delta)$. The interferogram and spectrum form a Fourier cosine transform pair and can be computed from one another as shown below.

$$S(\delta) = \int_{-\infty}^{+\infty} B(\tilde{v}_o)cos(2\pi\tilde{v}_o\delta)d\widetilde{v_0} \tag{2.5}$$

$$B(\tilde{v}_o) = \int_{-\infty}^{+\infty} S(\delta)cos(2\pi\tilde{v}_o\delta)d\delta \tag{2.6}$$

2.3.2 Resolution

Consider a spectrum that consists of features, at two distinct wavenumbers, $\tilde{v}_1$ and $\tilde{v}_2$, but with identical magnitudes. The resolution of an interferometer is the minimum difference in these positions, $\Delta\tilde{v}$, such that the corresponding spectral features can still be resolved. In the time domain, when these two beams with distinct wavenumbers are superimposed, the interference pattern will repeat every multiple of $(\Delta\tilde{v})^{-1}$ where the beams are in phase. Therefore, in order to just resolve the two wavenumbers, the maximum travel distance of the movable mirror, Δ_{max} has to be such that

$$\Delta\tilde{v} = (\Delta_{max})^{-1} \tag{2.7}$$

Obviously, the longer distance an interferometer scans, the finer the Restricting the resolution. Longer scanning will also require longer times and result in overall lower signal to noise ratio (SNR) per resolution element. Hence, a resolution that is sufficient for the problem at hand is usually recommended. A finite resolution implies a finite maximum retardation. The effect of this finite maximum retardation is to introduce a truncation function, $D(\delta)$, called the instrument line shape to the beam, where

$$D(\delta) = \begin{cases} 1, & -\Delta \leq \delta \leq +\Delta \\ 0, & |\delta| > |\Delta| \end{cases} \tag{2.8}$$

$$B(\tilde{v}_o) = \int_{-\infty}^{+\infty} S(\delta)D(\delta)cos(2\pi\tilde{v}_o\delta)d\delta \qquad 2.9$$

The resulting spectrum is a convolution of the original spectrum with the Fourier transform of $D(\delta)$. Choosing an appropriate truncation function is important to obtaining useful data. For the boxcar truncation function above, the Fourier transform is a $sinc$ function. The $sinc$ function, however, is not a useful line shape because of its large oscillating amplitudes away from the center. The side lobes of a $sinc$ function can reach negative values with a magnitude 22% of the primary peak and small features that fall in these negative regions will appear omitted from the computed spectrum. Therefore, apodization is used to control the effect of the finite retardation by modulating the instrument line shape in order to minimize these secondary effects.

2.3.3 Apodization

The molecular fidelity of the spectrum and resolution of the interferogram can be improved by controlling appropriately the instrument line shape, $D(\delta)$. When the boxcar apodization function is used to modulate the instrument line shape, a spectrum consisting of two adjacent spectral lines of equal intensity as shown in **Figure 2.2**, the two features cannot be resolved when the separation is less than $0.5/\Delta$. Analogous to the definition of resolution for optical microscopy, the resolution for spectrometers is often defined using the Rayleigh criterion and the full width at half-height criterion.[3] For the Rayleigh criterion, we can consider these lines distinguishable if the resulting curve has a dip of approximately 20% of the maximum intensity, which occurs at $0.73/\Delta$ separation, as shown in **Figure 2.3**. The lines would be considered fully resolved if the separation dips down to the baseline.

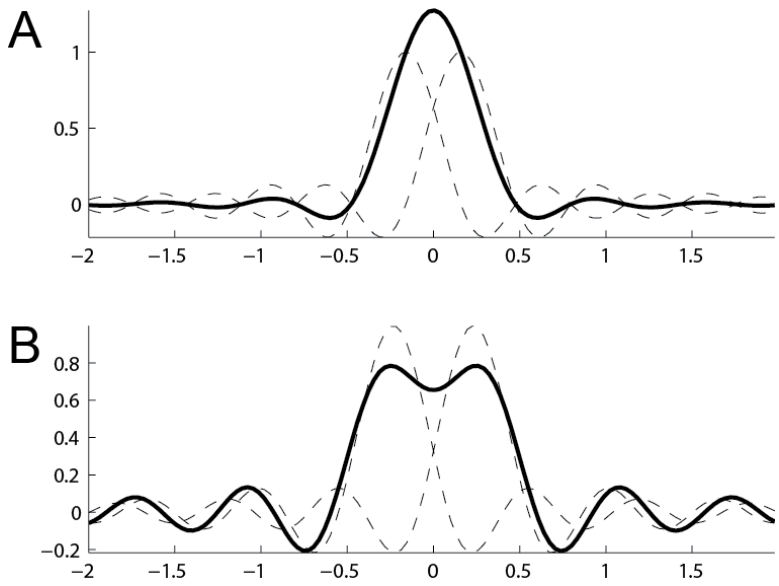

Figure 2.2. $sinc$ functions of a spectrum consisting of two distinct wavenumbers spaced (A) $0.5/\Delta$ and (B) $0.73/\Delta$ apart. The features in the first scenario cannot be resolved.

Several apodization techniques have been proposed to replace the box car function including trapezoidal, triangular, triangular squared, Bessel, sinc squared, and Gaussian functions.[3] All these functions have smaller oscillatory side lobes. The following example illustrates the use of a triangular function (defined below) in apodization. The Fourier transform of a triangular function is a $sinc^2$ function. Using the same separation ($0.5/\Delta$) as **Figure 2.2A** above, the triangular apodization function allows the distinct components of the spectrum to be resolved.

$$T(\delta) = \begin{cases} 1 - \left|\frac{\delta}{\Delta}\right|, & \Delta \leq \delta \leq +\Delta \\ 0 \quad\quad , & \delta > |-\Delta| \end{cases} \qquad 2.10$$

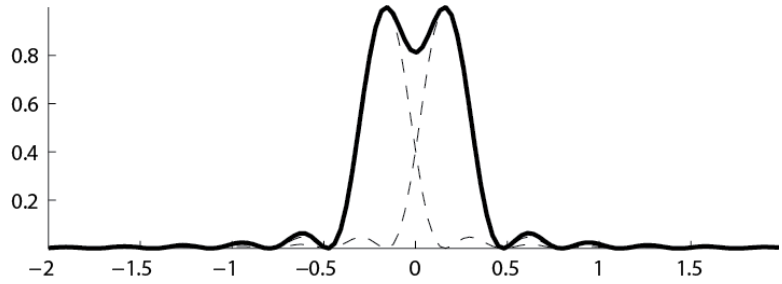

Figure 2.3. $sinc^2$ function of a spectrum consisting of two distinct wavenumbers spaced $0.5/\Delta$ apart. Unlike the $sinc$ function, the triangular apodization function clearly allows the closely spaced features in this spectrum to be resolved.

2.3.4 Sampling

The analog signal that arrives at the detector eventually undergoes a digitization process. While an extremely high sampling rate can better emulate a continuous signal, first, this is not practical because the FFT calculation will take a prohibitively long time. Second, the source, optical components or detector may either be spectrally limited in their response or the throughput in the system can be limited by the use of appropriate optical filters. Hence, the combination of a useful bandpass for the desired spectral analysis and minimal computation can lead to optimal spectral recording and processing. Once the spectral and optical parameters are set, the appropriate sampling rate so as to retain all the information from a band limited signal is given by the Shannon-Nyquist sampling theorem. The theorem states that the sampling rate must be at least twice the bandpass of the system in order to accurately represent the original analog signal. Care must be taken to ensure that a signal being sampled at a rate 2F does not have frequencies above F. The presence of frequencies above F results in aliasing and can potentially affect the entire signal. **Figure 2.4A** shows the Fourier transform of a signal with bandwidth F being sampled at a frequency, $f_s < 2F$. This causes a corruption of the data in the (overlap) frequency range below frequency F. In order to prevent an overlap of frequencies, i.e. aliasing, the data must be sampled at no less than 2F as shown in **Figure 2.4B**.

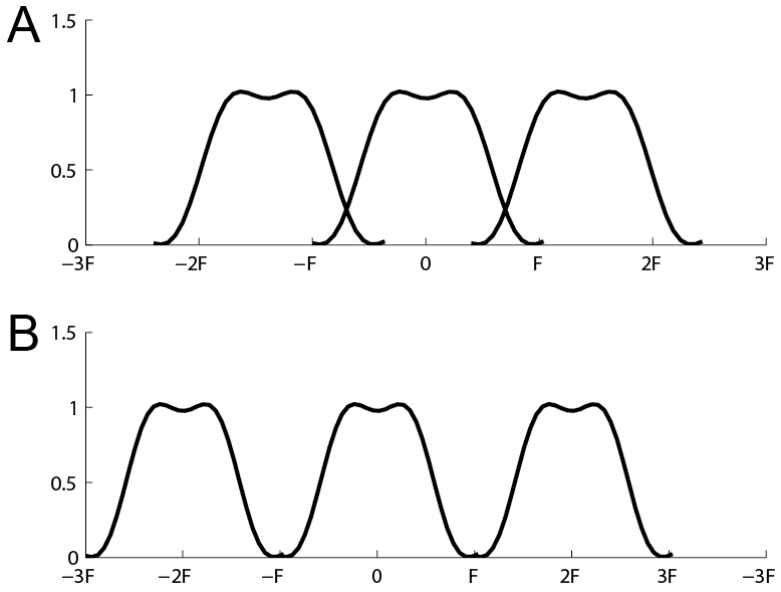

Figure 2.4. A signal sampled at A) $f_s < 2F$ results in aliasing, which can be avoided by sampling at B) $f_s \geq 2F$

The analog optical signal are digitized using an analog-to-digital converter (ADC). Modern ADCs typically have a resolution between 14 to 18 bits which allows the ability to distinguish between 2^{14} to 2^{18}, or respectively 16,384 to 262,144, separate voltage levels. However, at least 1 bit is typically reserved for noise to prevent truncation errors. For a spectrum with a resolution of $\Delta\tilde{\nu}$ and a bandpass between $\tilde{\nu}_{max}$ and $\tilde{\nu}_{min}$, the number of digital levels required to record its interferogram is shown in Equation 2.13 and the dynamic range is approximated by its square root.

$$M = \frac{\tilde{\nu}_{max} - \tilde{\nu}_{min}}{\Delta\tilde{\nu}} \qquad 2.11$$

A common mid-infrared spectrum with a bandpass of 3,600 cm^{-1} at a resolution of 4 cm^{-1}, will required 900 digital levels. The dynamic range of this spectrum is the number of digital levels of the ADC divided by the dynamic range of the interferogram, which in this case is roughly 1000:1 for a 16-bit ADC. Commercial FT-IR instruments can even exceed this spectral dynamic range and use higher resolution ADCs.

2.3.5 Empirical Errors

The prior theoretical analysis assumes a perfectly collimated beam which is difficult to achieve experimentally. Smaller sources are more collimated but have a weaker signal at the detector. A beam traveling through the interferometer with the largest solid angle possible without degrading the resolution will yield the highest signal. A monochromatic beam passing through a Michelson interferometer will create interference fringes, called Hädinger fringes, on the image plane at the detector. These fringes will oscillate sinusoidally when the retardation increases. If the entire beam was measured, an interferogram cannot be generated because there would be no average change in intensity. An aperture, called a Jacquinot stop, limits the beam such that only the central peak of the fringe pattern passes to the detector. The maximum solid angle allowed for the beam is given by

$$\Omega_{max} = 2\pi \frac{\Delta\tilde{\nu}}{\tilde{\nu}_{max}} \tag{2.12}$$

Alignment of the fixed mirror, moving mirror, and beam splitter relative to one another will affect the interferogram. The mirror drive mechanism must be capable of keeping the plane of the moving mirror at a constant angle to the beam path at all points during the scan. A small angle discrepancy of any mirror during the scan will result in a misaligned detector causing a significant reduction of signal intensity. Moreover, fringes can be formed at the detector plane resulting in poor data quality.

2.3.6 Signal to noise ratio (SNR)

The signal to noise ratio of an acquired spectrum is one of the most critical quantities for obtaining the best analytical results. Due to abovementioned considerations, the noise in FT-IR spectrometers is usually dominated by the noise at the detector. Since the noise is random and uncorrelated with the source intensity, signal averaging offers significant advantages. Often, extensive signal averaging is required, especially in microscopy formats. The SNR scales as $t^{1/2}$, ultimately providing a diminishing return and yielding to the effects of other noise sources, including medium term drift and source fluctuations. When all parameters (range, source

intensity and resolution) have been optimized for the experiment and the best possible hardware chosen, signal averaging is the recourse for improving the SNR.

2.3.7 FT-IR Spectroscopic Imaging

FT-IR Spectroscopic imaging couples a Michelson interferometer to an infrared microscope. There have been significant developments in the theory of FT-IR spectroscopic imaging in the past three years. Since its inception, FT-IR imaging data has been treated as a direct extension of FT-IR spectroscopy, with the additionally trivial consideration that data are spatially resolved. Other than reflecting species concentration, the spatial structure of the sample was not thought to play a major role on the recorded data. However, there are fundamental differences in the data recorded between homogeneous and heterogeneous samples that arise because of the microstructure of samples on the scale of the wavelength. Recent work has shown that the recorded spectra can be significantly different in important ways from FT-IR spectroscopy and these differences arise due to the shape and distribution of different chemical species[16–18] as well as the effects of focusing optics, which are considerably less impactful in non-imaging systems. Rigorous electromagnetic models analyzing the interaction of light with heterogeneous samples have quantified the nature of these spectral differences. A systematic and robust difference is indeed observed experimentally, validating the theory.

The theory of interaction of infrared light with layered samples has shown that the recorded data can be distorted from bulk spectra because of sample thickness. If the sample thickness is known a priori, iterative techniques can be used to estimate the bulk spectra from FT-IR imaging data. In the absence of thickness information, co-estimating both geometry and spectra is difficult and convergence to the correct result is not always guaranteed. Extending this model to include both lateral and transverse heterogeneities has also been proposed.[17] Using these models, it is possible to predict the collected spectrum when the infrared optical properties and the geometry of the sample are known. Spectral differences are typically more prominent in transflection FT-IR imaging data relative to transmission data. These spectral differences fundamentally arise due to scattering of light at optical boundaries and the nature of theses distortions can be quantified. This work has demonstrated that distortions are maximum when the point of focus of infrared light is directly at the edge and they reduce as we move away from

the edge. Simultaneously recovering both geometry and spectra of samples using IR imaging is an open problem and the subject of current research.

2.4 Instrumentation

2.4.1 Hardware

The optical system in an FT-IR spectrometer primarily consists of a Michelson interferometer. This is a device that creates interference between a beam of light and its time delayed counterpart. Light from an IR source is directed toward a beam splitter which reflects about half the incident beam while transmitting the remaining half. The first half of the beam, having reflected off the splitter causing a half wavelength phase shift, then reflects off a fixed mirror causing another half wavelength shift, and straight back through the splitter to the detector. Concurrently, the remaining half first passed through the splitter, reflects off a moving mirror, and then travels back to the beam splitter which reflects the beam toward the detector resulting in an identical net phase shift relative to the first half. The moving mirror is used to change the distance travelled by the beam. When both path lengths are equal, at zero optical path difference (OPD) or retardation, the beams recombine constructively. If the movable mirror is displaced by a quarter wavelength, resulting in an optical retardation of a half wavelength, the two beams are now 180° out of phase so would be complete destructive interference when recombined at the beam splitter. A signal (interferogram) is obtained as a function of retardation.[3]

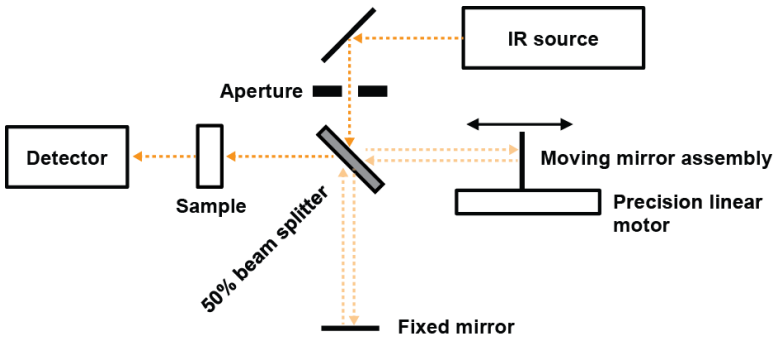

Figure 2.5. Schematic of a Michelson interferometer

The ability of the mirror drive motor to keep the movable mirror in constant alignment and speed is critical for interferogram quality. Furthermore, as the only moving part in the

interferogram, the motor assembly must be resilient to wear. The drive in modern interferometers consists of a brushless DC servomotor mounted on air bearings for frictionless motion. These servomotors contain an electromagnetic transducer with a fixed magnet. The force produced by the electromotor is function of the length of the coil wire, the current passing through it, and the field strength of the fixed magnet. The maximum force is typically around 1 to 2 Newton and can move a mirror assembly with a mass between 50 to 500 g. Advanced modern precision linear motor stages can provide single nanometer resolution with 5 nanometer guaranteed repeatability. These stages contain laser position encoders that have sub-nanometer resolution and are capable of providing positional feedback useful for spectroscopy. Their use has not been reported in interferometers for IR spectroscopy but one has been implemented in our laboratory.

2.4.2 Continuous Scan Interferometer

This mirror drive is currently the most common implementation[3,19,20] of FT-IR spectrometers. The mirror travels at a near constant velocity usually faster than 0.1 mm s^{-1} during each scan. To obtain accurate phase data, the motor must accelerate and decelerate before and after the data collection region so the mirror can maintain a constant velocity. Usually multiple passes are made and the signal is summed. This improves the SNR since noise is random and only increases with the square root of the number of scans. This signal averaging process is performed as many times as necessary in order to obtain the desired SNR. Depending on the quality of the motor, it may not have the necessary accuracy to generate consistent interferogram. Alignment of the interferogram center burst may be necessary prior to averaging. Since the retardation is dependent on the scanning velocity V' over t seconds,

$$\delta = 2V't \tag{2.13}$$

Equation 2.4 can then be modified as

$$S(\delta) = B(\widetilde{v_o})cos(4\pi\widetilde{v_o}V't) \tag{2.14}$$

2.4.3 Step-Scan Interferometer

In a step-scan interferometer, the moving mirror is stopped at discrete retardation until the measurement is completed. The interferogram is built by discrete retardation points rather than discrete time points. Since time is decoupled from the mirror position, a desired retardation can be held and measured for any amount of time. However, the step-scan interferometer is slower due to the time required for mirror to stabilize, is less efficient in data acquisition due to these delays, may suffer from additional noise sources due to positioning and limited filtering capability and requires more expensive and complicated hardware. This method was only more favorable in early FT-IR instruments due to slower detector speeds.[6] Faster detectors and electronics have made the rapid-scan interferometer more popular for many applications. Step-scan interferometers are now primarily used to record the evolution of transient molecular events over a period of time.[6] At each retardation setting, the molecular event is retriggered in order to take a new measurement point.

2.5 Detectors

2.5.1 Thermal and Quantum Detectors

The two types of infrared detectors available are of thermal or quantum design. The sensing element of a thermal detector responds to change in temperature. A thermocouple generates an electromotive force, bolometers or semiconductors change resistance, and pneumatic detectors contain a diaphragm that moves due to the expansion of a gas. Most of these have become obsolete for modern FT-IR spectroscopy due to slow response times. The only mid-IR thermal detector that has sufficient speed, linearity, low cost, and capable of operating near room temperatures is the pyroelectric bolometer. The sensing element of pyroelectric detectors initially used in most rapid-scanning FT-IR spectrometers was triglycine sulfate (TGS). In the 1980s, Deuterated triglycine sulfate (DTGS) was found to have a higher Curie temperature, the point of failure, so it replaced TGS in FT-IR spectrometer designs. Most recently, deuterated l-alanine-doped triglycine sulfate (DLATGS) is preferred.

Quantum detectors contain either a photomultiplier tube (PMT) or a semiconductor sensing element or. In a PMT, when a photon strikes the photoemissive surface, electrons are produced due to the photoelectric effect. A focusing electrode directs these electrons toward

electron multipliers causing a cascading effect. Eventually, enough of these secondary emissions are generated in order to produce a detectable electric current. PMTs require high energies in order to produce a current. Therefore, they can only be used in near-IR regions lower than 1 micron. Semiconductor based detectors are used for the near to mid infrared region. In the semiconductor element of a quantum detector, the electrons in the valence band become excited to the higher energy level conduction bands when interacting with IR radiation. The level of excitation depends on the energy of each photon which is proportional with its wavenumber. However, the wavenumber can only increase until the cutoff where the detector response drops suddenly. Semiconductors are often used for their relatively small bandgap between the valence and conduction bands. Adjusting the doping level of the material through by introducing small impurities is often used to adjust the electrical properties of the semiconductor. A common semiconductor used in IR detectors is mercury cadmium telluride (MCT). The ratio of the HgTe and CdTe used to create the MCT determines the band-pass frequency response of the detector and is closely related to its sensitivity, which is characterized by its specific detectivity.

2.5.2 Single Point Detectors

FT-IR spectroscopy can be used to raster scan a sample to create an image where each pixel contains the infrared spectrum of the specimen at that specific point.[18] The beam from the interferometer is directed at an IR opaque aperture that restricts light to the prescribed sample area. The basic apertures are typically manufactured from carbon black coated metal. However, more advanced microscope designs use apertures formed from IR-absorbing glasses in order to allow visible images to be obtained while recording IR spectra.[6] However, light passing through the aperture will form a diffraction pattern that allows unwanted light to reach the detector. The problem due to these diffraction artifacts is resolved by using a second aperture on the opposite side of the sample in front of the detector to serve as a rejection mask.[6] Since the point spread function narrows, we can achieve a higher resolution but with the drawback of a lower signal to noise ratio.[6] Longer acquisition times and multiple passes are necessary to compensate.

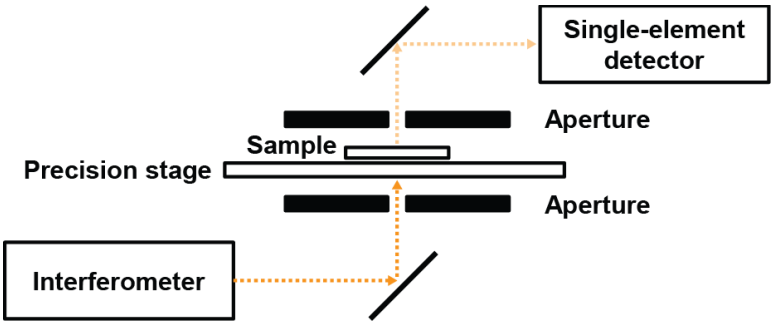

Figure 2.6. Design of a FT-IR instrument incorporating a single-element detector. Dual apertures on either side of the sample minimize error due to diffraction artifacts.

The sensitivity of a detector is usually described in terms of the noise equivalent power, NEP, which is the optical power required to give a signal equal to the noise level.[3] NEP is proportional to the square of the detector area A_D and the specific detectivity D^*. The noise power, N' in Watts, of a measurement over t seconds is given[18] by

$$N' = \frac{NEP}{t^{1/2}}, \quad NEP = \frac{{A_D}^{1/2}}{D^*} \tag{2.15}$$

Given the spectral brightness $U_v(T)$ derived from the Planck equation, using an interferometer at resolution $\Delta\tilde{v}$, throughput Θ, and efficiency ξ, the signal power, S', is given[18] by

$$S' = U_v(T)\Theta\Delta\tilde{v}\xi \tag{2.16}$$

Therefore, the SNR is

$$SNR = \frac{S'}{N'} = \frac{U_v(T)\Theta\Delta\tilde{v}\xi t^{1/2}}{NEP} = \frac{U_v(T)\Theta\Delta\tilde{v}\xi t^{1/2} D^*}{{A_D}^{1/2}} \tag{2.17}$$

FT-IR instruments are limited by trade-offs between SNR, resolution, and acquisition time. This property is known as the "spectroscopic trading rules".[3] Under the criteria of constant throughput and constant mirror velocity, $U_v(T)$, Θ, ξ, and D^* are all constant. In order to measure at twice the resolution, in other words half the $\Delta\tilde{v}$, over the same time period t, SNR will be halved and noise doubles. The relation between SNR and time is shown in Equation 2.18. But, if the throughput is variable, then Θ is also halved so the SNR actually decreases by a factor of

four. The same principle applies when changing the velocity of the movable mirror where the result is identical to varying the scan time.

$$SNR \propto t^{1/2} \tag{2.18}$$

The time can also be impacted by the interferometer resolution $\Delta\tilde{\nu}$. If $\Delta\tilde{\nu}$ is smaller than the full width at half max (FWHM) of the smallest features of the spectrum, lowering $\Delta\tilde{\nu}$ will have little impact on the features' intensity. However, it will increase noise by a factor depending on the constant or variable throughput criterion described previously. If $\Delta\tilde{\nu}$ is much larger than the FWHM of the features, then the feature will appear narrower but with a higher amplitude. If the spectrum is primarily composed of weak narrow lines, lowering the resolution has no effect on the SNR of the spectrum. Therefore, measuring a spectrum that has broad features at excessively high resolution will decrease the potential SNR.

Apodization will affect the SNR of a spectrum. When changing from the boxcar apodization function shown in **Figure 2.2** to the triangular function shown in **Figure 2.3**, the SNR is decreased by a factor of $\sqrt{3}$ on average. Apodization functions are mostly identical at retardations near zero, so changing it will not affect low spatial frequency noise. Changing the apodization function will affect the degree at which high spatial frequency noise is attenuated. Apodization functions that decay more sharply will smooth the spectrum more.

FT-IR instruments incorporating single point detectors also have their speed impacted by individual point mapping. A programmable microscope stage is required to be capable of performing precise movements at the micron scale and then return accurate positional feedback. The stage is used to move the sample such that the beam scans across the desired collection region. Incrementing over thousands of micron sized points across an entire image can take days to weeks to complete. While FT-IR allows measurements at high fidelity, the acquisition time of raster scanning each point of an image individually limits is applications in time critical environments.[21]

2.5.3 Multi-element Detectors and Imaging

Detectors can be arrayed in a linear format or as a focal plane array (FPA). These multi-element detectors, which consist of many detector channels in parallel, allow for faster data

collection and are commonly used for imaging purposes.[6,22–24] The beam of IR light covers the entire detector surface allowing many points to be captured simultaneously at each position of the raster scan. The read out time of multiple channels will be slower than reading from a single element detector. The additional delay depends on system electronics. Yet, this is still much less than the time it takes for the stage to move. Imaging with a multi-element detector, in general, will be faster by a factor of the number of channels in that array. For instance, a 256x256 pixel detector will have a speed advantage of 65,536 fold.

Additionally, higher SNR can be obtained because it eliminates the need for apertures.[6] The dimensions of pixels in a modern detector array are in the tens of microns, compared to single element detectors which are 100-250 microns in size.[6] Since SNR is proportional to the inverse square root of detector size, the smaller multi-element detectors allow for considerable SNR increase. From the single-element SNR analysis summarized by Equation 2.17, the theoretical SNR of a FPA detector can be derived[6] as

$$SNR = \frac{0.12\pi A\left(1-\sqrt{1-(NA)^2}\right)U_v(T)\Theta\Delta\tilde{\nu}t^{1/2}D^*}{{A_D}^{1/2}} \qquad 2.19$$

where NA is the numeric aperture and A is the area of the sample collected per pixel.

The number of pixels on a multi-element detector has been increasing steadily and is expected to increase in the foreseeable future. The speed advantage of parallel data acquisition using multi-element detectors is a key driving force behind the broad deployment of FT-IR imaging. These improvements in hardware, in conjunction with the dramatic increase in computing power due to faster processors, have made FT-IR imaging a powerful tool for molecular analysis. Development of robust signal processing and data analysis algorithms in the recent past has also been important. These developments are making real time analysis of samples using FT-IR spectroscopic imaging practicable in the near future.

2.6 High-Definition Imaging

2.6.1 Synchrotron FT-IR Spectroscopic Imaging

Synchrotron FT-IR spectroscopic imaging combines infrared light from multiple synchrotron beams with wide-field detection using an infrared microscope.[25] Compared to IR

thermal sources, synchrotron sources are stable, broadband and emit high-brightness radiation. The resolution of any FT-IR imaging systems is limited by the diffraction limit of the mid-IR light and the numeric aperture of the objective. For the shortest wavelength of interest, 2.5 microns, and a numerical aperture of 0.65, a pixel spacing of around 0.96 microns or smaller may be achieved. However, commercial instruments are typically limited to a spatial resolution of 5.5 microns in order to ensure a sufficient SNR from the weak thermal source. Using a synchrotron source with the same setup, hence, alleviates the lack of throughput and enables smaller pixel sizes at the sample plane to be recorded. One example of such a device is the synchrotron at the University of Madison-Wisconsin that combines 12 high-flux IR beams through a 74X objective to completely illuminate a FPA detector.[25] The use of multichannel 128x128 pixel FPA detectors removes the need for apertures while allowing for significantly lower acquisition times. However, these synchrotron FT-IR imaging systems have limited applications due to the size and accessibility of the source.

FT-IR synchrotron instruments have allowed for IR diffraction limited imaging measurements of human breast and prostate tissue.[25] As shown in **Figure 2.7**, synchrotron FT-IR instruments are capable of a dramatic increase in spatial resolution. This study identified the chemical characterization of cell types and tissue structures such as the basement membrane in human prostate tissue. The ability to image at fine detail permits the identification of tissues that are key components of cancer diagnosis.

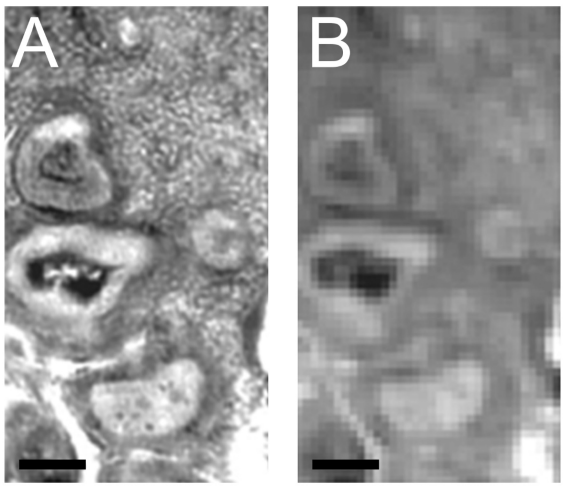

Figure 2.7. Cancerous prostate tissue A) imaged with a multi-beam synchrotron FPA (0.54 micron pixel size), compared to B) an image from a thermal source linear array (6.25 micron pixel size) (50 micron scale bar).[25]

2.6.2 Attenuated Total Reflectance FT-IR Imaging

Attenuated Total Reflectance (ATR) FT-IR imaging relies on the total internal reflection of the incident beam using a solid immersion lens that creates an evanescent electric wave that interacts with the sample. The evanescent waves penetrate 1 to 4 microns into the sample. The lens must have a higher refractive index than the sample, so it is typically made from germanium, diamond, or zinc selenide crystal. Furthermore, the sample must be in complete contact with the lens to prevent the presence of air bubbles where the change in refractive index would systematically distort data. The physical contact may cause damage to the sample as well as changes in conformation. In most cases, liquid samples can be imaged in their natural state with little or no preparation required. ATR can also be an excellent technique for measuring the composition of solids which often absorb too much energy to be measured by IR transmission.

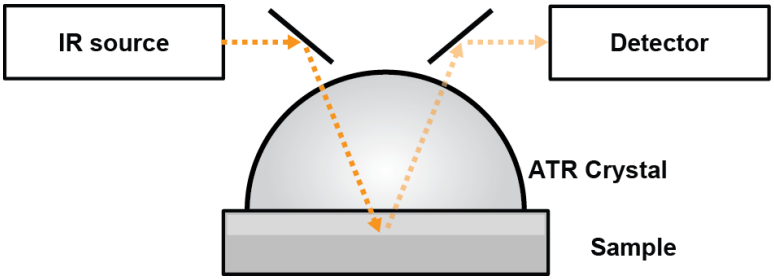

Figure 2.8. Schematic of an ATR FT-IR imaging system.

The spatial resolution of the instrument increases at higher angles of incident light. Since ATR FTIR imaging is a near field technique, there is no theoretical diffraction limit. However, there are practical limitations on spatial resolution due to SNR. At higher incident angles, there is a trade-off between increased spatial resolution and decreased wave penetration depth. Infrared radiation can only interact with the sample up to a depth (dp) depending on the wavelength λ, incident angle θ, and refractive indices n_1 and n_2 of the materials.

$$dp = \frac{\lambda}{2\pi\sqrt{n_1^2 sin\theta^2 - n_2^2}} \qquad 2.20$$

ATR FT-IR instruments have been shown to be capable of imaging large samples at nearly 1.5 by 2 mm in size, at spatial resolutions at up to 1.25 microns, using linear and FPA detectors with dimensions up to 256x256 pixels.[26] Studies have demonstrated that this can

identify important components in tissues and yield new insights into disease processes and their associated chemical changes.[27]

2.6.3 Bench-top High-Definition Imaging

Bench-top high definition FT-IR spectroscopic imaging has been a relatively recent development. Rigorous electromagnetic models for light propagation through a FT-IR imaging instrument have been proposed recently. Creating a complete model for the propagation of light through the instrument has led to key insights and improved instrument design. An appropriate choice of pixel size, Cassegrain magnification, numerical aperture and wavelength has been used to optimize image quality. Consequently, previously obscured spatial information can now be obtained using the new instruments. Data from table-top FT-IR spectroscopic imaging instruments are now capable of spatial resolution and data quality comparable to that from a system using a gigantic synchrotron source, although the SNR from the table-top instrument is significantly lower for a single scan.

The advent of bench-top high-definition imaging instruments has important implications for the application of FT-IR imaging. In a wide array of applications, molecular information coupled to high spatial detailed can be a powerful investigative tool. In the study of diseases like breast cancer, for example, high spatial detail can be important in diagnosis. The infrared spectrum from FT-IR imaging provides information that helps distinguish epithelial tissue from stroma and this is an important parameter in disease diagnosis. However, the spatial resolution of current FT-IR imaging instruments is insufficient for distinguishing inter-lobular stroma which can be potentially diagnostic. High-definition imaging has solved this problem by providing significantly higher spatial resolution and image quality. New instruments incorporating the capability of high-definition imaging are likely to be adopted widely in the near future.

As noted in the section on FT-IR imaging theory, one has to be careful in the interpretation of spectra when observing chemically heterogeneous samples. Differences between spectra of homogeneous and heterogeneous samples need careful attention to avoid incorrect interpretation. Spectral differences can be utilized in characterization and identification of chemical contents of a sample. However, one has to be careful not to assign chemical significance to every variation in the spectrum. Robust identification of chemicals from distorted spectra is a subject of current research.

2.7 Applications

FT-IR spectroscopic imaging has a wide range of applications today. Many ongoing studies deal with investigating fundamental processes involved in disease initiation and progression. Imaging also has significant implications toward the design of methodologies for disease diagnosis and prognosis in a clinical environment. In addition, the ability to characterize various natural and artificial materials at a chemical level is a desirable tool used across many disciplines. There are numerous studies and applications that can be found in several recent reviews from our group and others. Rather than an exhaustive review of the past work, here we present examples of some of the exciting recent developments primarily to provide an illustration of the possibilities.

2.7.1 Cancer Histopathology

Preliminary screening of cancer tends to be sensitive to the disease but at a cost of specificity. Further histologic analysis via biopsies is the gold standard for cancer diagnosis. These histopathology tests typically involve hematoxylin and eosin (H&E) staining of sectioned tissue. A pathologist trained to recognize the morphology of cell types must inspect the patterns in each tissue sample and determine if there are alterations, if these alterations indicate a disease, and if so, characterize its severity. The vast majority of biopsies, however, are actually benign and this consumes excessive health care resources.[28] Additionally, the human factor is often not accurate when dealing with indeterminate cases. FT-IR imaging is developing to become a high-throughput, automatic, and accurate tool capable of making a clinical impact by improving the efficiency of cancer screening.[23,29,30]

Automated histopathologic methods for classifying FT-IR imaging data using Bayesian classification have been developed recently.[30,31] The prediction algorithm is trained to high confidence levels using hundreds of tissue samples in microarrays. Only an optimal subset of metrics that has diagnostic potential is incorporated into the algorithm. The conditional probabilities for the metrics are used to build a discriminant function that returns probabilistic recognitions of cellular states. The model is then applied on FT-IR image data. It is first segmented into regions of similar cell types by applying pattern recognition techniques. Furthermore, spectra and spatial information from the local neighborhood of each data point are

used to determine the presence of a disease and its severity. Supervised classification is performed using chemically stained data segmented by an expert pathologist as a gold standard data.[31] Validation of the resulting algorithm is performed against an independent data set and receiver operating characteristic (ROC) curves are used as a measure of classification accuracy. Information from classification of FT-IR imaging data can be combined with H&E stained visible images[32] to provide further improvements in segmentation. First the images are aligned and overlaid. This is done by using a smoothing filter to identify rough shapes that can be transformed with a least square error minimization approach. Segmentation and feature extraction algorithms then process the combined data sets. This technique has been shown to yield highly accurate classification results.[32–37]

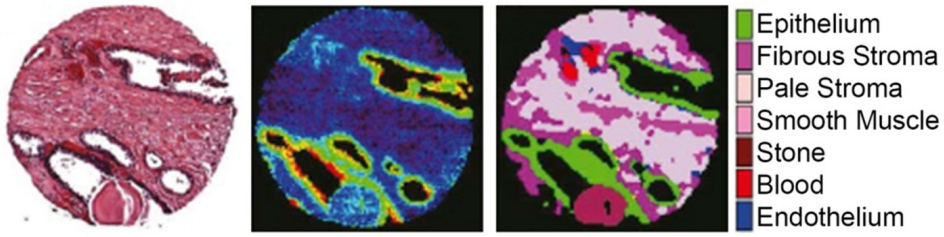

Figure 2.9. Prostate tissue section hematoxylin and eosin (H&E) stained (left) compared to its FT-IR absorption data at 1,080 cm^{-1} (center). The FT-IR spectrum can be analyzed for unique spectral features for each cell type (right) thus providing more information than the conventional H&E stain. The diameter of the sample is approximately 500 microns.[31]

2.7.2 Cell culture

In vitro cell cultures can serve as a model for many environments in the human body. Imaging cell cultures with FT-IR techniques allow us to research the fundamental processes involved in disease initiation and progression.[38–41] During carcinoma progression, the tumor microenvironment transforms both chemically and morphologically. ATR FT-IR spectroscopic imaging has been used to examine these transitions prevalent in early cancer development.[15] The increased spatial resolution allowed the location of the transformations to be identified. The changes in the spectra were found to be associated with protein modifications in the cell cytoplasm rather than events occurring in the nucleus.[15]

2.7.3 Tissue Characterization and Engineering

Morphologic, histologic, and chemical analyses using FT-IR spectroscopy have been performed characterizing porcine skin in order to determine if it can serve as an accurate model for human skin.[42] Porcine skin is a convenient choice for lab environments because it can be cryo-prepared and remain chemically stable over a prolonged time. In this study, a marker molecule such as Dimethyl sulfoxide was tracked over the depth of the skin. This molecule has a unique absorbance spectrum which allows its location to be accurately monitored. The diffusion concentration profile indicated that porcine skin was very similar to human skin both structurally and chemically.[42]

An active area of study is the use of 3D tissue engineered model systems. Many complex interactions found in 3D tissue cultures are often not found in 2D models and engineered skin is able to represent human skin because it has a simple laminar structure. The use of FT-IR imaging systems on 3D tissue samples is a recent development that has not yet been well characterized. The various spectral changes associated with different cell types within engineered skin versus human skin have been studied using FT-IR image analysis.[43] Investigations have used FT-IR imaging to monitor the chemical changes of stromal cells surrounding malignant melanocytes. 3D cultures of engineered skin were designed to model melanoma.[43–45] FT-IR analysis characterized the chemical changes of the stromal cells surrounding the malignant melanocytes.[43] Furthermore, this research led to novel insights that may allow for improved quality control and standardization in tissue engineering.[43]

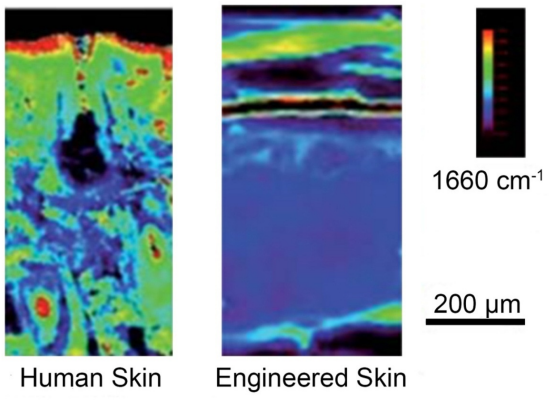

Figure 2.10. FT-IR images of human skin versus 3D tissue engineered skin.[43]

2.7.4 Drug Diffusion

FT-IR spectroscopy is a valuable tool for drug diffusion studies. There are many advantages to transdermal drug delivery in handling, safety, controlled release, and avoiding the gastrointestinal tract. Some FTIR-ATR designs can allow for non-invasive real time measurements of drug diffusion.[46–48] The most important advantage of the ATR technique is that it is non-destructive to the sample and provides a profile drug concentration over tissue depth. In this setup, a membrane acting as a drug acceptor is placed between the ATR crystal and the drug donor. The drug diffuses through the acceptor membrane and builds up at the ATR crystal. The concentration of the drug at the membrane to crystal interface between membrane and crystal is monitored by the appearance and increase of drug specific IR bands over time

2.7.5 Polymers

IR spectroscopy is often used to characterize the properties of polymers and IR imaging was widely used to characterize heterogeneous polymer systems and dynamics therein. Most of these studies focused on fundamental polymer science and less on medically-relevant applications. Recently, however, there have been several reports of the analysis of biomaterials, analysis of materials used in biological applications and biologically-derived polymers. For instance, many applications in tissue engineering and medical devices rely on hydrated polymer coatings on polymer substrates. The thickness of the coating has consequences in tissue response as well as mechanical properties. FT-IR spectroscopy can be used to determine thickness measurements relative to initial calibration with atomic force microscopy.[49] The diffusion of low molecular weight species into polymers also has implications for designing drug release devices.[50] FT-IR images taken periodically generated spatially resolved spectral data and absorbance profiles of the polymer.[50] Another study used FTIR spectroscopy to determine the lower critical solution temperature of hydrogels commonly used in medical devices.[51] This technique can be applied to both linear and cross-linked polymers. The spectral changes especially in the C-H stretching region showed conformational changes when heated above the critical temperature.

2.8 Summary

IR spectroscopic imaging, combining the advantages of optical microscopy and molecular spectroscopy, is a powerful tool for analysis in several physical sciences and biomedical disciplines. By combining interferometry and wide-field detection in microscopy, in particular, FT-IR imaging allows the spatial examination of the spectroscopic fingerprints of the chemical constituents of a sample. Recent developments in FT-IR instrumentation, data processing, and theoretical analyses have led to FT-IR imaging becoming a rapid, robust and reliable tool for molecular analysis with a clear understanding of the underlying theory and origin of signals. While significant progress has been reported in using the approach for biomedical imaging, the translation of these emerging capabilities to cell and tissue analysis is now being pursued and will likely result in many new applications or ones with significantly enhanced capability in both spatial and chemical analyses.

CHAPTER 3: VERSION 1.0 – DISCRETE FREQUENCY IMAGING [†]

3.1 Abstract

Conventional mid-infrared (mid-IR) Fourier transform infrared (FT-IR) spectroscopic imaging systems employ an incoherent globar source and achieve spectral contrast through interferometry. While this approach is suitable for many general applications, recent advancements in broadly tunable external cavity Quantum Cascade Lasers (QCL) offer new approaches to and new possibilities for mid-IR micro-spectroscopic imaging. While QCL-based devices have yet to achieve the wide spectral range generally employed by spectroscopists for molecular analyses, they are starting to be used for microscopy at discrete frequencies. Here, we present a discrete frequency IR (DFIR) microscope based on a QCL source and explore its utility for mid-IR imaging. In our prototype instrument, spectral contrast is achieved by tuning the QCL to bands in a narrow spectral region of interest. We demonstrate wide-field imaging employing a 128x128 pixel liquid nitrogen cooled mercury cadmium telluride (MCT) focal plane array (FPA) detector. The resulting images demonstrate successful imaging as well as several unique features due to coherence effects from the laser source. Here we discuss the effects of this coherence and compare our instrument to conventional mid-IR imaging instrumentation.

3.2 Introduction

Infrared (IR) spectroscopic microscopy is a widely-used technology for achieving chemical contrast at the micrometer scale. Modern instrumentation combines mid-infrared vibrational spectroscopy, microscopy and wide-field detection[52] and has been shown to have broad applications, including in polymer science,[53] cancer histopathology,[31] drug diffusion studies,[42] analyses of trace gasses,[54] and tissue engineering.[43] The basis of this approach relies on the property that many functional groups in molecules have resonant frequencies in the mid-IR spectral range (2-14 μm). The absorption spectrum is a chemical signature that contains contributions from each of the different functional groups constituting the molecules and can be

[†] The work in this chapter has previously been published and is reprinted with permission.

Yeh, K.; Schulmerich, M.; Bhargava, R. Mid-Infrared Microspectroscopic Imaging with a Quantum Cascade Laser. In *SPIE*; Druy, M. A., Crocombe, R. A., Eds.; **2013**; Vol. 8726, p 87260E.

used to create contrast in the image thus providing direct material identification and alleviating the need for external contrast agents or chemical dyes.

One approach to chemical imaging is Fourier transform infrared (FT-IR) spectroscopy. The powerful advantage of FT-IR spectrometry for imaging is in the ability to multiplex signals via interferometry, which allows for the full intensity of the source to be used at all wavelengths therefore resulting in a multi-fold advantage in sensitivity and resolving power when compared to other methods of achieving spectral resolution.[3] FT-IR spectrometers typically employ a globar thermal source which is simple, stable, and low cost. Its broadband emission profile has sufficient intensity for many applications. The most recent improvements in IR spectroscopic imaging continue to be driven by the development of larger format multiple-element linear and focal plane array (FPA) detectors, which require use in a careful manner.[1] Dividing the total flux of a globar source over an increasing number of detector array elements is a system limitation; therefore, higher flux sources have potential to offer major improvements in imaging performance. The use of a synchrotron source,[25] for example, has enabled faster high-definition IR imaging compared to a laboratory setup.[55]

Quantum Cascade Lasers (QCL), first developed in the 1990s,[56] are now becoming commercially available in a variety of packaging options and wavelength regions. They are often designed as an external-cavity laser that utilizes an adjustable grating for spectral selection of tunable discrete frequencies (DF).[57] QCLs can emit extremely narrow spectral line widths less than 0.01cm^{-1} with wavelength dependent intensities averaging over 100mW, far exceeding that put out by a globar source, while functioning at room temperature in a comparatively compact package.[58] Additionally, newer QCL models are rapidly being developed with larger tunable ranges.[59] QCLs have been reported in a variety of studies investigating their use in IR spectroscopic analysis,[60–63] microscopy,[64] and imaging.[65,66]

While there are examples of using lasers for spectroscopic imaging, these are usually prevalent at either macro (> 1 mm) or nanoscale (~ 10 nm) resolution. The ratio of the wavelength to feature size, hence, is either very large or very small in these cases. Wide-field microscopic imaging in the mid-IR using a coherent laser source, where the feature sizes in the image are approximately of the same order of magnitude as the wavelength, presents new challenges.[64] While challenges in understanding data in a microscope using an incoherent source have been recently addressed,[16,17,67] the spatial coherence in using QCLs will require careful

interpretation of the data. In particular, the introduction of interference patterns that will appear as either laser speckle or edge fringing caused by the physical structures in the sample, need to be carefully understood. Furthermore, the tunable range of a single QCL only covers a relatively small region of the mid-IR spectrum. In order for meaningful spectroscopic analysis of tissues and other materials, multiple QCL units will be needed to cover the spectral range typically utilized in FT-IR spectroscopy. Accuracy and stability in beam tuning and power output will also be important areas of investigation. In this manuscript, we report on our initial efforts to characterize and demonstrate the feasibility of QCL sources for discrete frequency infrared spectroscopy and microscopy.

3.3 Experimental

3.3.1 Instrumentation

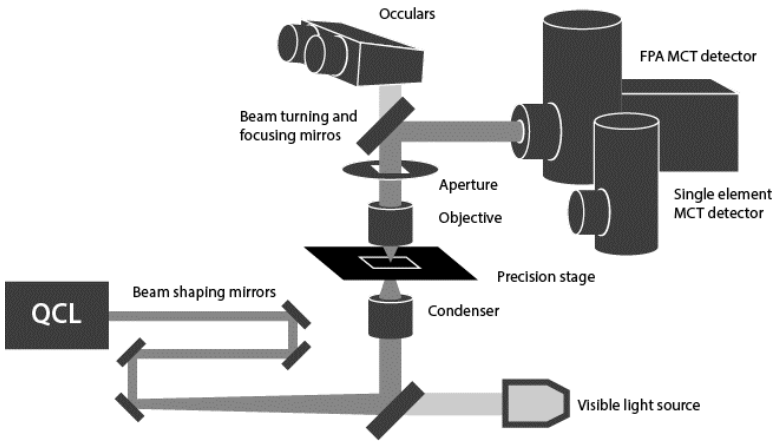

Figure 3.1. Schematic of the QCL-based wide field imaging components configured in transmission mode

The instrument we have developed in-house is schematically illustrated in **Figure 3.1**. It uses a tunable QCL (Daylight Solutions, San Diego, CA), operable in continuous wave (CW) or pulsed modes, with a frequency tuning range between 1570 to 1738 cm^{-1}, wavelength dependent power typically over 100 mW, and a laser linewidth of 0.003 cm^{-1}. Water cooling maintains the laser at its optimal operating temperature of under 20° Celsius. The laser output is expanded to fill the back aperture of the condenser via a series of optical elements. The optical system is comprised of a 0.56 NA germanium glass alloy ($Ge_{28}Sb_{12}Se_{60}$) condenser and.an objective turret with interchangeable germanium glass alloy lenses of numeric apertures of 0.56 and 0.85

(LightPath Technologies, Orlando, FL). This corresponds to effective FPA pixel sizes of 2.5 μm and 0.8 μm respectively. The lenses are coated with an anti-reflection coating (IR-3) that transmits approximately 98% of the incident beam at the QCL's center wavelength. Sample alignment and raster capabilities are controlled with a precision microscope stage (Prior Scientific, Rockland, MA). The instrument is configured in transmission mode with a liquid nitrogen cooled 128x128 pixel focal plane array (FPA) mercury cadmium telluride (MCT) detector (IRCameras, Santa Barbara Focal Plane, Santa Barbara, CA). A 0.5 NA reflective Schwarzschild objective, oculars, and a CMOS camera were installed on the system for sample alignment.

3.3.2 Data Acquisition

To test the optical system, images were acquired for a USAF 1951 optical resolution target conforming to the MIL-STD-150A standard. This target has been traditionally used to test the performance of imaging systems. The target was patterned using SU-8 photoresist deposited at a thickness of 15 μm and developed on a 2mm thick barium fluoride (BaF_2) substrate (International Crystal Laboratory, Garfield, NJ). The imaged patterns are the bars at group 5 element 1 which has a standardized bar width of 15.63 μm. Frames from the FPA were collected at 1610 Hz with an integration time of 0.02 ms. The QCL was stepped through its entire frequency range from 1570 to 1738 cm^{-1} in 0.5 cm^{-1} steps, and for each band, 1600 frames were recorded by the FPA and co-added to generate each image in the sequence. At each wavenumber, the laser current was calibrated such that its detected power falls within the dynamic range of the FPA. The same process was performed on a blank BaF_2 surface to create a background spectrum. At each wavenumber, a background image was taken along with the target image. This was used to ratio out the spectral contributions from the source, atmosphere, and other systematic elements in order to calculate the SU-8 absorbance spectrum. Absorbance was then calculated by computing the negative base 10 logarithm of the target to background ratio.

Configuring the FPA and image acquisition was controlled by WinIR (IRCameras, Santa Barbara Focal Plane, Santa Barbara, CA). The image sequences were then processed and visualized using custom scripts written in MATLAB (The MathWorks, Nantucket, MA), ENVI (ITT Visual Information Solutions, Boulder, CO), and ImageJ (National Institutes of Health, Bethesda, MD).

The comparative FT-IR images were taken with a Varian 680-IR FT-IR spectrometer a 620-IR imaging microscope equipped with a 0.5 NA reflective Schwarzschild objective (Agilent, Santa Clara, CA). The Varian system also uses a liquid nitrogen cooled 128x128 pixel MCT FPA. The samples were measured at 2 cm^{-1} spectral resolution with 32 co-additions and the absorption spectrum was calculated based on a background frame obtained with a 128 co-additions.

3.4 Results and Discussion

A comparison of images acquired with both the QCL and FT-IR imaging spectrometers are presented in **Figure 3.2**. The results were compared with images taken by a Varian FT-IR system at the same sample location illustrating the spatial resolution of both systems at 1608 cm^{-1}. For this image the QCL based system used 0.56 NA germanium glass alloy objective and a matching condenser, while the Varian was fitted with a 0.5 NA reflective Schwarzschild objective. The image size over 128x128 pixels for the QCL instrument is approximately ~300 μm x 300 μm in our designed system, whereas the commercial system images an area of approx. ~ 700 μm x 700 μm.

As expected from a coherent source, features at the edges of the bars are especially apparent in the QCL images. The edge intensity at this wavenumber is roughly twice that of the actual SU-8 absorbance measurement from the center of the bar. This is likely due to multiple reflections and scattering from the structures in the sample, which is significantly more pronounced when using a spatially coherent source. In contrast, the absorbance profile is relatively flat across the entire width of the bar in the FT-IR image. With the use of a coherent source, fringing is visible in the background as well. Observing the 1710 cm^{-1} and 1650 cm^{-1} column images of **Figure 3.4A**, a broad semi-circular pattern is visible in the top right quadrant of the image. Additional finer fringe structures are present especially in the lower left quadrant. The magnitudes of these fluctuations are wavelength dependent.

Coherence effects can be seen more clearly in **Figure 3.3** with images taken with a 0.85 NA objective with an effective pixel size 0.8 μm. The image of the target at group 5 element 3, with expected bar widths of 12.41 μm shows fringes contoured around the edges of the SU-8 on the sample. Here, we also imaged two 10 μm polystyrene spheres placed in close proximity to one another such that the interference pattern of the fringes could be observed. The theoretical

concept behind this phenomenon is that, every pixel on the detector receives signal contributions from not only the corresponding pixel at the sample plane, but also pixels around it with a radius depending on the coherence area.[64] These electric field contributions interfere depending on phase and the result is seen as fluctuating intensities by the detector. Therefore, while these fringes may appear as noise, they actually contain structural information about the sample. A complete theoretical framework is required to understand the meaning and utility of this additional information provided by the QCL system in order to separate absorbance data from structural data.

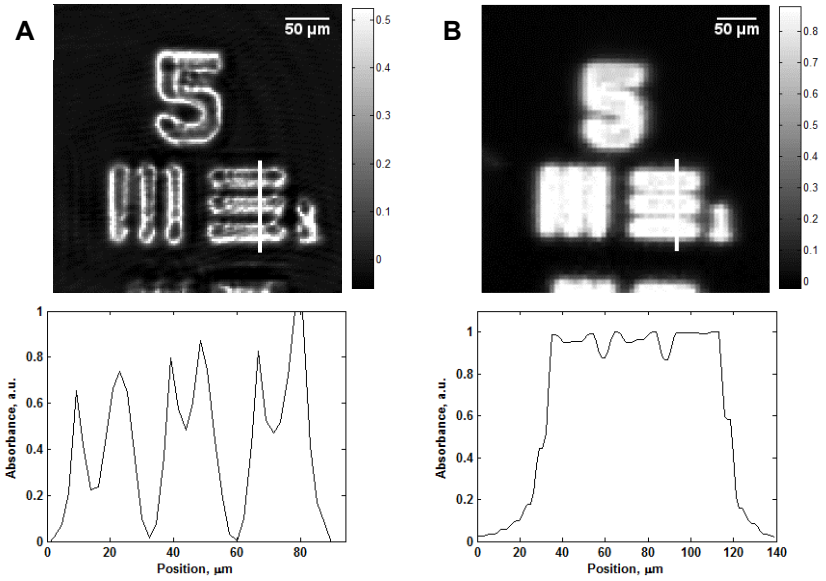

Figure 3.2. Absorbance images at 1606 cm^{-1} of a 1951 USAF resolution test chart (group 5, element 1) acquired by a (A) QCL based system with a germanium glass alloy objective with a 0.56 NA, and (B) Varian FT-IR system with a 0.5 NA Schwarzschild objective. SU-8 has an absorbance peak at this wavenumber as shown in **Figure 3.5**. The second row shows the profile across the horizontal SU-8 bars as indicated by the vertical line in the images. These absorbance values have been normalized in order to compare the images.

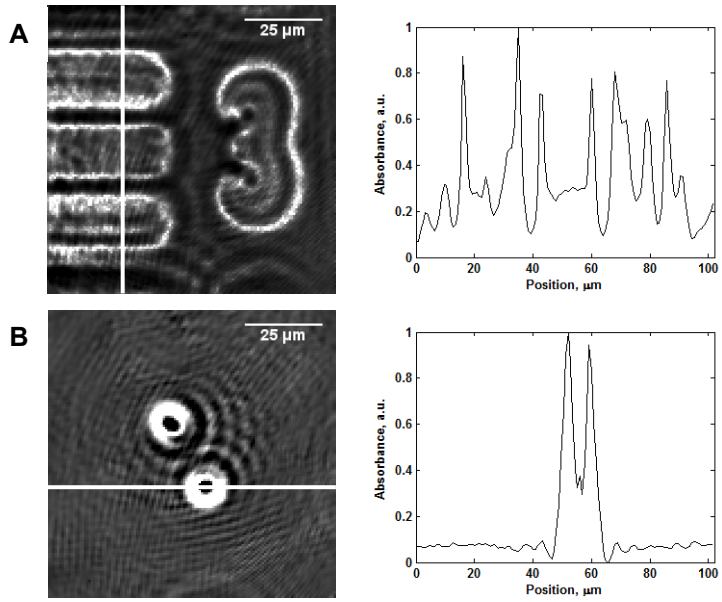

Figure 3.3. Interference patterns due to the effects of a coherent source (A) SU-8 patterned USAF 1951 resolution target (group 5 element 3), and (B) 10 µm diameter polystyrene spheres. The plots show the absorbance profile across the image in the region as indicated by the line. The effective pixel size is 0.8 µm making the field of view 102.4 µm in each dimension.

The SU-8 photoresist has distinctive absorbance peaks at 1608 and 1580 cm^{-1} while BaF_2 is transparent across the mid-infrared wavelength range. **Figure 3.4** shows images at each of these absorbance peaks as well as images at 1650 and 1710 cm^{-1} where the spectral profile is flat. The lighter shading at 1608 cm^{-1}, indicating higher absorbance, is clear especially in the numeric five in both the QCL and FT-IR rows. **Figure 3.5** shows the absorbance spectra measurements of SU-8 from the numeric five on the sample. This span from 1570 to 1738 cm^{-1} represents the tunable range of the QCL with the data taken at 0.5 cm^{-1} resolution. The FT-IR spectral data displayed here is only a subset of the full range (3850-0 cm^{-1} at 2 cm^{-1} resolution). These measurements demonstrate that a QCL based system can recover the SU-8 spectrum at these positions. However, we observe significantly more spectral noise.

Noise has a drastic impact on the signal to noise ratio (SNR) of the spectra and, consequently, on the quality of images acquired which lowers spatial and spectral quality, imaging speed, and the types of measureable samples. A contributing factor to noise comes from power fluctuations in the laser which have been measured up to 1.2 percent. Furthermore, laser speckle in the images has been measured at approximately 5 to 6 percent, though the effect is

expected to be strongly sample-dependent. These issues become worse at the limits of the laser's tunable range as well as at select positions where atmospheric water absorption is strongest. These challenges must be addressed to make full use of the QCL's high flux advantage over the globar source used in FT-IR spectroscopy.

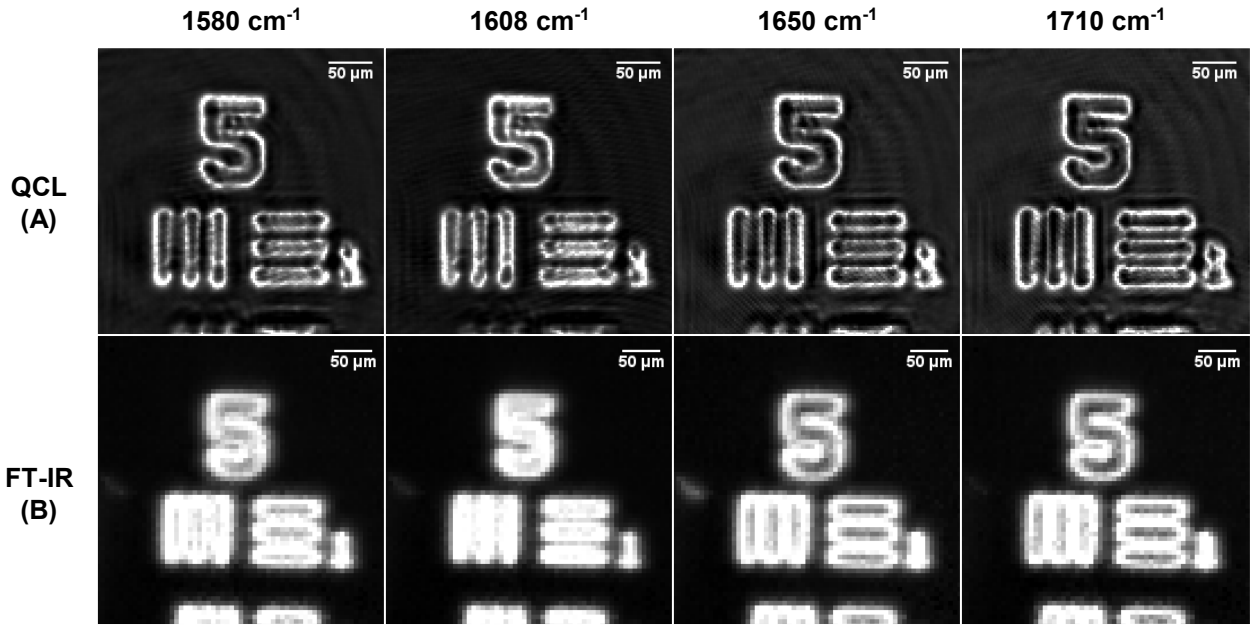

Figure 3.4. Absorbance images at select wavenumbers of a SU-8 patterned 1951 USAF resolution target (group 5, element 1) acquired using (A) a QCL system equipped with a 0.56 NA objective, and (B) a Varian FT-IR system with a 0.5 NA objective. The target consists of a SU-8 photoresist pattern on a BaF_2 substrate. SU-8 has absorbance peaks at 1580 cm^{-1} and 1608 cm^{-1} which can be seen by the lighter shading within the bars.

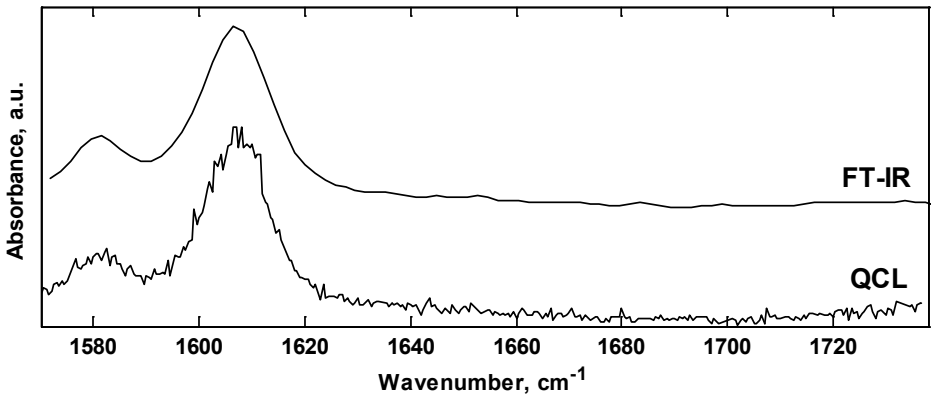

Figure 3.5. Absorption spectra of SU-8 photoresist measured by a QCL system and Varian FT-IR system at 0.5 cm^{-1} and 4 cm^{-1} spectral resolutions respectively. The spectra were calculated from a 3x3 pixel averaged window from the data shown above in **Figure 3.4** and the values have been normalized for comparison.

The QCL model used in this instrument has a tunable wavelength of 168 cm^{-1} centered at 1650 cm^{-1}. This entire range corresponds to just a single band (Amide 1) found in tissues. Therefore, this instrument is not equipped to perform tissue diagnostics as imaging at multiple bands is required to provide contrast. The mid-infrared range spans roughly 4000 cm^{-1} and multiple QCL devices would need to be multiplexed together for adequate coverage. Even then, a full range measurement would not be feasible while FT-IR spectrometers are readily available. However, for sample diagnostics and imaging purposes, most the spectral data taken is not actually used; only a few spectral bands are needed to provide contrast.[68] In this case, however, an FT-IR spectrometer would first need to survey the spectrum and identify the spectral bands of interest. Then, a few separate QCL devices will tune to these bands and provide the spectral contrast required. Matching them to work in a seamless multiplexed configuration is an area of further development.

3.5 Conclusion

We have demonstrated the use of QCLs as a source for discrete frequency mid-infrared wide-field imaging. Their narrow spectral linewidths tunable to wavenumbers and high intensity emissions have many advantages to the globar source typically used in FT-IR spectroscopic imaging. The intrinsic properties of the QCL, especially the high spatial and temporal coherence, generate images that contain both absorbance (chemical) data as well as structural information

and will require careful interpretation. The spatial resolution of the QCL system is competitive to that of a commercial FT-IR instrument, although more development is required to improve the noise characteristics in the spectral data. The advantage of a QCL based system lies with single wavelength measurements where it offers imaging speeds and intensities far higher than what a FT-IR instrument can provide.

CHAPTER 4: **VERSION 1.1 – FAST WIDE-FIELD IMAGING** ‡

4.1 Abstract

Infrared (IR) spectroscopic imaging systems are a powerful tool for visualizing molecular microstructure of a sample without the need for dyes or stains. Table-top Fourier Transform infrared (FT-IR) imaging spectrometers, the current established technology, can record broadband spectral data efficiently but requires scanning the entire spectrum with a low throughput source. The advent of high-intensity, broadly-tunable Quantum Cascade Lasers (QCL) has now accelerated IR imaging but results in a fundamentally different type of instrument and approach, namely discrete frequency IR (DF-IR) spectral imaging. While the higher intensity of the source provides higher signal per channel, the absence of spectral multiplexing also provides new opportunities and challenges. Here we couple a rapidly tunable QCL with a high performance microscope equipped with a cooled focal plane array (FPA) detector. Our optical system is conceptualized to provide optimal performance based on recent theory and design rules for high-definition (HD) IR imaging. Multiple QCL units are multiplexed together to provide spectral coverage across the fingerprint region (776.9 to 1904.4 cm^{-1}) in our DF-IR microscope capable of broad spectral coverage, wide-field detection, and diffraction-limited spectral imaging. We demonstrate that the spectral and spatial fidelity of this system is at least as good as the best FT-IR imaging systems. Our configuration provides a speedup for equivalent spectral signal to noise ratio (SNR) compared to the best spectral quality from a high-performance linear array system that has 10-fold larger pixels. Compared to the fastest available HD FT-IR imaging system, we demonstrate scanning of large tissue microarrays (TMA) in 3-orders of magnitude smaller time per essential spectral frequency. These advances offer new opportunities for high throughput IR chemical imaging, especially for the measurement of cells and tissues.

‡ The work in this chapter has previously been published and is reprinted with permission.

Yeh, K.; Kenkel, S.; Liu, J.-N.; Bhargava, R. Fast Infrared Chemical Imaging with a Quantum Cascade Laser. *Anal. Chem.* **2015**, *87* (1), 485–493.

4.2 Introduction

Obtaining high-quality structural and molecular information from biological samples is an analytical challenge in many clinical and research studies. Traditionally, optical microscopy or fluorescence techniques have been used with a variety of dyes and labels to improve contrast but these external contrast agents can perturb biological samples and are limited to imaging known molecular species. Vibrational spectroscopic imaging techniques, such as using mid-infrared (IR) absorption, allow for the non-perturbing molecular study of microns-thick samples. As many molecular functional groups have resonant frequencies in this spectral range, the mid-IR absorption spectrum provides image contrast as well as uniquely identifies a sample's chemistry without the need for dyes or prior analytical knowledge of its composition.[69] These factors have led to a significant number of potential biomedical applications of IR chemical imaging.[34,70–74] Today, the most popular configuration for IR chemical imaging is the Fourier transform infrared (FT-IR) imaging spectrometer which employs multiplex detection of wavelengths via interferometry. In its most common form, an interferometer is coupled to a multichannel, liquid nitrogen-cooled mercury cadmium telluride (MCT) detector. The detector in commercial imaging spectrometers are typically a linear array (LA)[75] or a focal plane array (FPA).[22] FT-IR imaging instruments use a globar thermal source which has a broadband emission profile with sufficient intensity for data recording, but limits further improvement due to the trade-offs between spectral and spatial performance.[3] For instance, while larger format detectors with smaller active elements could yield faster imaging, their implementation is difficult as the total flux of the globar source must be divided among each pixel. As the individual detector elements get smaller, the signal decreases proportional to area of the detector, adversely affecting the recorded signal-to-noise ratio (SNR). Additionally, due to the nature of the interferometer, the scanning mirror must travel further in order to increase in spectral resolution, which in turn requires closing down the input aperture to maintain a certain level of collimation the beams passing through the interferometer arms. This dramatically reduces the available flux requiring more sample co-additions to preserve the SNR.[1] Thus, commercial FT-IR instruments are typically limited to ~4 cm^{-1} resolution with ~5 μm pixels in order to ensure sufficient SNR from the thermal source.[52]

Higher flux sources can offer numerous advantages toward faster high-definition IR imaging. The most dramatic example is the development of high-definition imaging[25] that

provided high quality data using a synchrotron source[76] and significantly noisier data using a globar. The recent availability of quantum cascade lasers (QCL) has now made the same advances feasible, albeit in a discrete frequency (DF) configuration that contrasts with the prevalent FT-IR and filter based DF-IR technology.[77] QCLs are a type of semiconductor laser commonly packaged in an external cavity (EC) configuration with an approximate 200 cm^{-1} tunable range.[56–58] In recent years, they have become commercially viable in multiplexed configurations spanning the fingerprint region.[59] With narrowband line widths at intensities unmatched by globar sources, QCLs have been incorporated into discrete frequency (DF) instrumentation for chemical sensors,[54,60,63] cavity ringdown spectroscopy,[61] analysis of aqueous samples,[62,78] as well as microscopy.[64,65,79–82] This combination of QCLs with custom designed instrumentation for microspectroscopy provides the unique option of collecting datasets at high SNR. In implementations reported to date, however, the potential of QCLs has not been fully realized. While an uncooled array detector-based instrument was shown to be feasible and is now commercially available, the challenge of using QCLs with high performance cooled FPAs has not been addressed. Here we demonstrate the feasibility of using high-performance, cooled FPA detectors with fast readout speeds in conjunction with a rapidly tunable QCL. We first describe methods to overcome challenges in instrumentation for this configuration. Second, we compare the performance of our setup against commercial high performance systems. Both high spectral quality (LA) and high spatial quality (HD FPA) imaging spectrometers are compared. Finally, we demonstrate the advantages of using our approach for biomedical tissue imaging.

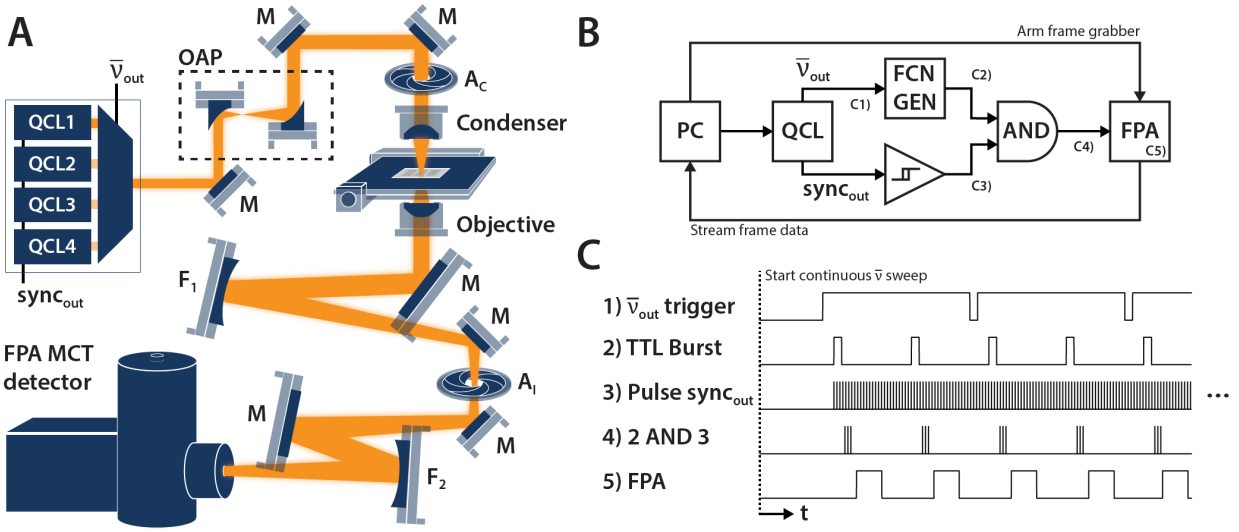

Figure 4.1. (A) Schematic of the QCL-based wide field imaging microscope configured in inverted transmission mode. The microscope is coupled to a 4 chip widely tunable QCL and a 128x128 FPA MCT detector. (B) Wiring diagram showing the primary control components of the system (stage omitted). The timing structure on the annotated trigger lines are then shown (not to scale). (C) A generalized synchronization protocol. The real-time wavenumber monitoring line output from the QCL controls an external oscillator that triggers the FPA depending on the specified spectral resolution and scan speed.

4.3 Experimental Section

4.3.1 QCL Microscopy

We have developed a custom IR microscope, as shown in **Figure 4.1A**, built for integration with commercial QCL sources. The net magnification of the microscope is 20X and 43X with effective pixel sizes of 2.02 and 0.95 µm respectively, resulting in 259 µm and 122 µm corresponding linear fields of view. While the setup is similar to conventional IR microscopes, additional care must be taken during setup and alignment to minimize back reflections which will appear as a flickering ripple effect across the field of view. This behavior can be minimized by slightly closing the condenser's back aperture (A_C) and the windowing aperture (A_I). Beam shaping reflective optics, a pair of off-axis parabolic mirrors (OAP) with 2X magnification, direct the QCL emission to fill the back aperture of a 0.56 NA BD-2 glass ($Ge_{28}Sb_{12}Se_{60}$) AR coated condenser (LightPath Technologies, Orlando, FL, USA). The inverted transmission microscope uses interchangeable BD-2 glass AR coated 0.56 NA and 0.85 NA objectives in conjunction with a 250mm focal length (FL) image forming mirror (F_1). Planar mirrors (M) are

placed to direct the beam at small incident angles to minimize the off-axis aberrations from spherical mirrors (F_1 and F_2). The intermediate image at A_I is then focused with a 150mm FL mirror (F_2) onto a SBF161 128x128 pixel focal plane array (FPA) mercury cadmium telluride (MCT) detector (Lockheed Martin Corporation, Santa Barbara Focal Plane, Santa Barbara, CA, USA). These FPA MCT detectors have microsecond response times that allow for scanning speeds far faster than uncooled IR cameras that can only operate in the millisecond regime. MCT detectors also have the highest noise-equivalent power (NEP) ratings among broadband IR detectors which allow the instrument to maintain sufficient SNR even in areas of lower QCL power output. While uncooled FPAs and bolometers are available in much larger formats, their readout rates are currently limited to standard video rates of tens of frames per second and insufficient for implementation with fast tuning QCLs.

The microscope was paired with a widely-tunable QCL source (LaserTune from Block Engineering, Marlborough, MA, USA) that contains 4 individual QCL chips with a combined tuning range of 776.9 to 1904.4 cm^{-1} that can be scanned at up to 25 cm^{-1}/ms with emission powers between 0.5 to 15 mW. We have set the laser to pulse at 2 MHz with a 31 ns pulse width corresponding to a 6.2% duty cycle. The sweep speed is limited by the maximum 1612 Hz frame rate of the FPA (f_{FPA}), the desired spectral resolution, and number of in-scan co-additions. The wiring diagram of the various control signals in the system is illustrated in **Figure 4.1B**. While sweeping, the laser outputs a TTL synchronization pulse as it crosses every 0.5 cm^{-1} for real-time wavenumber monitoring to correct for any nonlinearities in the tuning grating motion (**Figure 4.1C1**). This is used to trigger an external oscillator (**Figure 4.1C2**) that either: a) bursts N_B pulses per wavenumber trigger at f_{FPA} rate for $N_B \geq 1$, or b) counts $\frac{1}{N_B}$ wavenumber triggers for each pulse sent. The pulse train from the oscillator is used to trigger the FPA frame grabber after it is synchronized to the QCL's pulse sync output (**Figure 4.1C3**). The sync output from this laser has a shark-fin wave shape, so it is first threshold with a Schmitt trigger, and then combined via a logical AND gate with the pulse train from the external oscillator (**Figure 4.1C4**). The FPA acquires a frame when the trigger line is high; any additional triggers during the integration and refractory periods are ignored. The synchronization ensures that the laser fires an identical number of times within the FPA's integration period (**Figure 4.1C5**) provided that the time jitter in the electronics is sufficiently small. Finally, the data from the FPA is streamed directly to a RAID disk array.

We have configured the laser to sweep across its entire 1127.5 cm−1 range at 0.38 cm−1/ms with an oscillator burst rate of 1500Hz. This allows us to acquire a 128x128 pixel image with 4512 spectral bands at 0.25 cm−1 resolution in less than 3 seconds. Several post-processing steps are conducted subsequently, especially to handle the noise in the QCL power output (**Figure 4.2**). The sharp intensity fluctuations in the 1500 cm−1 region, due to atmospheric water vapor absorption, are minimized as much as possible by containing the entire instrument within a nitrogen purged enclosure that brings the air humidity to approximately 5%. Using custom scripts written in MATLAB (The MathWorks, Nantucket, MA, USA), the dark current (I_{DC}) is first subtracted from the raw FPA data to get the AC signal (I_{AC}) (Eq. 4.1). We filter the data using a low pass FFT filter (F_{LP}) with a sweep speed dependent cutoff frequency of 15 Hz (Eq. 4.2). The spectral data is then averaged by in-scan co-addition of every 16 bands (N) (Eq. 4.3), to yield a 4 cm−1 spectral resolution ($\Delta\bar{\nu}$) data set containing 282 bands. The same procedure is performed on both the sample (I_S) and background (I_0) images prior to calculating absorbance (Eq. 4.4). The resulting single beam spectrum demonstrates the improvement over raw data.

$$I_{AC} = (I_{raw} - I_{DC}) \tag{4.1}$$

$$I' = FFT^{-1}(FFT(I_{AC}) * F_{LP}) \tag{4.2}$$

$$I_S(\bar{\nu}) = \frac{1}{N}\sum_{n=\bar{\nu}}^{\bar{\nu}+\Delta\bar{\nu}} I'(n) \tag{4.3}$$

$$A(\bar{\nu}) = -log_{10}\left[\frac{I_S}{I_0}\right] \tag{4.4}$$

Our ultimate goal was to image tissue microarray (TMA) sections, which are standard tools for high throughput IR microscopy today. To image tissue samples 1.1 mm in diameter with the available field of view, we stitch a 5x5 or an 11x11 mosaic with a 10% frame overlap for the 0.56 NA and 0.85 NA objectives respectively. An OptiScan microscope stage (Prior Scientific, Rockland, MA, USA) controls sample positioning while frame alignment and offsets are calibrated using an USAF 1951 optical resolution target. The adjacent frames are then merged per wavenumber with a linear weighted edge blend over the overlapping regions. Finally, the spectral images are processed in ENVI+IDL (ITT Visual Information Solutions,

Boulder, CO, USA) using a minimum noise fraction (MNF) algorithm[21] that removes the noise dominated principal components. The comparison images illustrated in this manuscript are displayed using a linear 2% stretch, followed by color and scale matching in ENVI and ImageJ (National Institutes of Health, Bethesda, MD, USA).

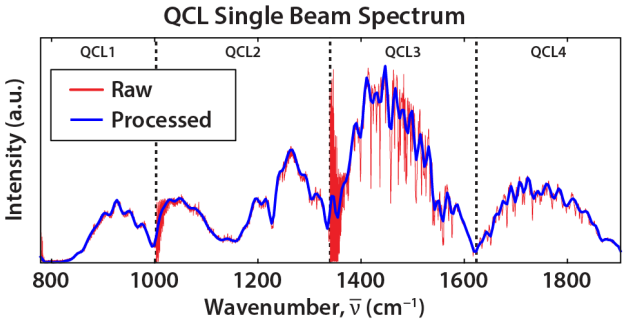

Figure 4.2. The QCL raw power output is noisy when rapidly sweeping across the spectrum (red). The recorded single beam spectrum is noise reduced via post-acquisition processes to yield a high-quality spectrum (blue). The crossover frequencies for each QCL chip are indicated and result in decreased signal intensity and increased spectral noise.

4.3.2 FT-IR Microscopy

Absorption reference images are acquired using a Varian Stingray 620-IR imaging microscope with a 680-IR FT-IR spectrometer (Agilent Technologies, Santa Clara, CA, USA), and a Spotlight 400 FT-IR imaging system with a Spectrum One spectrometer (Perkin-Elmer, Waltham, MA, USA).

The Varian is also equipped with a liquid nitrogen cooled 128x128 pixel FPA. The microscope is configured with a 0.62 NA reflective Schwarzschild objective and matching condenser resulting in a total magnification of 40X. With image pixel sizes of 1.05 µm, it requires an 11x11 mosaic to image 1.1 mm diameter tissue cores. Images were collected with 16 co-additions, 102 µs detector integration time, and an undersampling ratio (UDR) of 4 where data points are acquired on every fourth zero crossing of the FT-IR's internal laser reference. Interferograms were processed with a Blackman-Harris apodization function and then ratioed to a 128 co-addition background. The final truncated spectrum is stored with a 900-3800 cm^{-1} range at 4 cm^{-1} resolution. Images were stitched using the same weighted blending method described previously as well as MNF noise reduced in ENVI+IDL.

The Spotlight instrument uses a 16 element linear array (LA) detector to raster scan the sample. This instrument has a 15X 0.6 NA reflective Schwarzschild objective and a 6.25 μm image pixel size. This linear array is able to acquire spectra at higher SNR than an FPA so data is taken with only 2 co-additions and stored using a truncated 750-3800 cm^{-1} region at 4 cm^{-1} resolution. In addition to MNF noise reduction, the data is also corrected using Perkin-Elmer's proprietary algorithm designed to eliminate CO_2 and H_2O vapor contributions.

Sample Specification and Preparation. In this study, we imaged an unstained breast tissue microarray (TMA) (BRC1501, US Biomax Inc. Rockville, MD, USA) containing 149 cores of various stages and grades of cancer placed on BaF_2 substrate. Immunohistochemistry (IHC) stains of consecutive sections of the TMA were also imaged using an Axio Imager.M2 microscope (Carl Zeiss AG, Jena, Germany).

USAF 1951 optical resolution targets were also imaged for system characterization. Targets were patterned with SU-8 polymer (MicroChem, Westborough, MA, USA) on a polished 1 inch diameter barium fluoride (BaF_2) substrate (ISP Optics, Irvington, NY, USA). The substrate was first cleaned with acetone and isopropyl alcohol (IPA), and then rinsed with distilled water. A 5 μm thick layer of SU-8 polymer was spun coat on BaF_2 at 3000 rpm for 40 seconds. The sample was then baked in two steps to harden the SU-8 polymer: pre-bake at 65 °C for 1 minute followed by a soft bake at 95 °C for 3 minutes. A lithography mask was contact aligned and SU-8 was exposed to i-line UV radiation (365 nm) at 9 mW/cm^2 for 10 seconds. After baking at 65 °C for 1 minute and at 95 °C for 1 minute, respectively, the SU-8 targets were developed in SU-8 developer for 1 minute and rinsed with IPA.

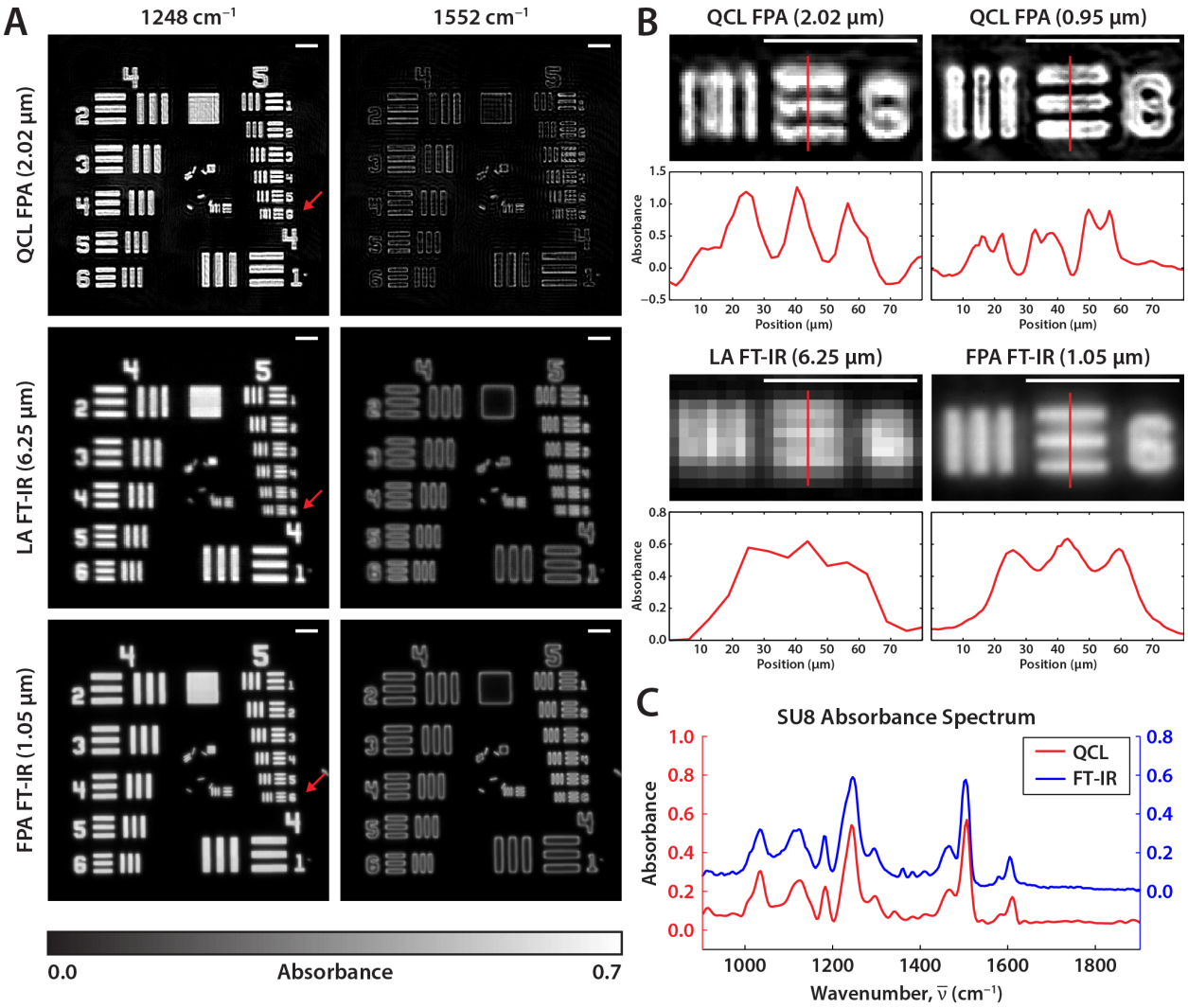

Figure 4.3. (A) SU-8 patterned USAF 1951 optical resolution target on BaF2 substrate imaged with the QCL microscope and two commercial FT-IR imaging systems. Images displayed are from an absorption band (1248 cm^{-1}) and non-absorbing region (1552 cm^{-1}). The resolving limit of each system is tested with group 5 element 6 (red arrow). (B) Enlarged images of group 5 element 6 at 1248 cm^{-1}, which has an 8.77 µm bar width, with y-profiles across the horizontal set of bars (red line) are plotted. Both QCL images are well resolved, the LA FT-IR image is unresolved, and the FPA FT-IR images are at the threshold of the Rayleigh criterion. (C) A comparison between the SU-8 absorption spectra between the QCL and FPA FT-IR imaging systems at 4 cm^{-1} resolution. The white scale bars displayed in all images are 100 µm in length

4.4 Results and Discussion

The performance of the QCL microscope is demonstrated by imaging SU-8, a photoresist polymer that has a distinctive spectrum with multiple peaks throughout the fingerprint region, on

IR-transparent BaF_2 substrate. It is patterned as a USAF 1951 resolution target which is commonly used to test the resolving power of imaging systems. Each group of bars, vertically arranged, contains 6 elements of decreasing size where each successive group is half the size of the previous one. The fifth group has features with sizes on the same order as the incident wavelength. We use this target to serve as a well characterized analog for tissue microarrays. Since both the tissue samples and SU-8 target are roughly the same thickness with features of comparable size, this type of target allows us to test these imaging systems under realistic conditions. The morphology of the sample has been shown to affect the recorded spectra.[16,17] Especially when imaging with a coherent source where scattering and edge effects can cause unwanted artifacts in both the spatial and spectral domains, unstructured samples, such as commonly available chrome on glass targets, would result in an overestimation of real world optical performance. Furthermore, these target calibration images are 1.2 mm wide and the area coverage of groups 4 and 5 is similar to a single tissue core. Through filtering, MNF processing, and mosaic blending, we show that the background non-uniformity and image tiling artifacts are barely noticeable which allows for clean large area TMA scans. To our knowledge, this data quality has not previously been reported.

The QCL microscope was configured to scan the SU-8 BaF_2 target at 4 cm^{-1} spectral resolution across the fingerprint region 776.9 to 1904.4 cm^{-1}. The same target was imaged using the two FT-IR instruments to serve as a standard for comparison. Here in **Figure 4.3A**, we see a selection of images from the full spectral data set representing SU-8 polymer on an absorbing peak at 1248 cm^{-1}. On a non-absorbing wavenumber at 1552 cm^{-1} on the spectral baseline, we see minimal absorbance and only intensity due to edge scattering from features on the sample. The QCL microscope, however, surpasses both the FT-IR systems in terms of resolving power as shown by **Figure 4.3B**. These images show the absorbance of the 6^{th} element of group 5 at 1248 cm^{-1}, marked by the red arrows in **Figure 4.3A**. Alongside each image is the vertical absorbance profile of the horizontal set bars, marked by the red line. Each bar is 8.77 μm wide, which is approximately the same width as the incident wavelength. An interesting feature is clearly visible in the high magnification QCL image. Scattering from the edges of the SU-8 bars results in a loss in energy that is manifest as a sharp increase in the recorded absorbance at that spectral element. This is quite similar to the images of edges as seen in optical microscopy. The edge scattering is well known in IR imaging but is likely amplified here by the high spatial coherence of the QCL

source. As can be seen in **Figure 4.3A**, scattering-induced features are also present in the FT-IR data, although much less pronounced. As the size of the bars decrease and approach the wavelength of light, the scattering-enhanced edge signals merge with the central absorbance values.

The lateral resolution of each system is physically dependent on the diffraction limit. As per the Rayleigh resolution, the optical system is considered diffraction limited if able to distinguish objects separated by $0.61\lambda/NA$. The two bars can be considered separable, per the Rayleigh criterion, if the intensity dip between them is at least 20-30% of the peak intensity. Furthermore, in order to satisfy the Nyquist criterion, the magnification of the image must be sufficient in order to achieve a spatial sampling rate at least twice the Rayleigh resolution at all mid-IR frequencies.[55] Both objectives on the QCL system are able to clearly resolve these group 5 element 6 bars, reading near zero absorbance levels between the bars. The effective pixel sizes of 2.02 μm and 0.95 μm respectively for the 0.56 NA and 0.85 NA objectives result in a slight spatial oversampling at the lowest QCL emission wavenumber. Neither of the other instruments has the same resolving power. The bars are barely distinguishable when imaged by the LA FT-IR instrument due to its larger 6.25 μm pixel sizes. The FPA-equipped instrument has higher magnification optics with smaller 1.05 μm pixel sizes and is just able to resolve these bars; the absorbance dip of approximately 26% is at the Rayleigh criterion threshold. While the spatial fidelity using QCLs is seen to be excellent, as noted by us and other investigators, a spectral examination has not previously been provided.

Maintaining accuracy in the spectral domain of multiplexed QCL systems is a non-trivial process. Unlike a typical broadband FT-IR source which has a blackbody spectral profile and interferometrically-determined spectral scale, each QCL unit is only tunable to roughly 200-300 cm^{-1} around its center wavenumber. When multiplexed together, depending on the manufacturer, these instruments can span large ranges but also have areas of low signal strength between center wavenumbers or discontinuities at cross-over frequencies as seen in **Figure 4.2**. Errors typically manifest as low frequency baseline oscillations from laser pulse-to-pulse power fluctuations or sudden absorbance spikes in the case of tuning mismatches between the sample and background scans. In order to maintain spectral accuracy during a sweeping scan across a large wavenumber range, the switching time between QCL units, as well as the acceleration and deceleration of each tuning grating, however small, should still be accounted for. A simple interpolation to

derive an image's corresponding wavenumber from acquisition timestamps by assuming a linear tuning speed is not accurate. Therefore, the ability to monitor the emission wavenumber in real-time with a TTL trigger output is critical. This allows us to record the sample and background spectra sequentially. If real-time monitoring is not available, the SNR drops drastically in sweep mode; we have found that discretely stepping through each wavenumber is more beneficial despite the significant cost in scan speed.

One-hundred percent lines from randomly selected pixels are shown in **Figure 4.4A** for the linear array and FPA-based FTIR imaging spectrometers and the QCL-based DF-IR instrument. A 100% line is often used to estimate the noise in FT-IR spectrometers. The use of the 100% is often to observe spectrum-to-spectrum consistency (flatness of the line) as well as to estimate the spectral noise. The response of the QCL-based instrument is flat but is significantly noisier than the other two. Specifically, we observed ~4-fold higher noise for equivalent scans in the QCL system. Noise in the 100% line can be safely assumed to be the analytical noise at any wavenumber in an FT-IR spectrometer as each spectral point contributes to the noise at every point. Thus, temporal variance at a wavenumber is the same as spectral variance around that wavenumber. The spectral variance, however, is not a useful measure of the noise in a QCL-based system at a given wavenumber. By averaging 100% lines from 1000 pixels in **Figure 4.4B**, we see the noise in FT-IR imaging systems is reduced according to the well-known trading rules of FT-IR spectroscopy, but structure still remains in the QCL spectrum. This shows that there is both a random and a shot noise component, which also is not constant over the spectrum. This raises an interesting question on how variance at each wavenumber should be quantified in DF-IR systems, for example to provide error bounds for measured absorbance. We recommend extracting that data from a time series and calculating the variance to obtain the error bounds. However, for static samples, it is known that the absorbance is invariant and the use of filtering techniques is well-justified (just as Fourier frequency bandpass filtering is employed in FT-IR spectroscopy). Thus, the issue of characterizing noise in a DF-IR system is much more complicated than the FT-IR case and best examined in detail with methods to obtain high quality data.

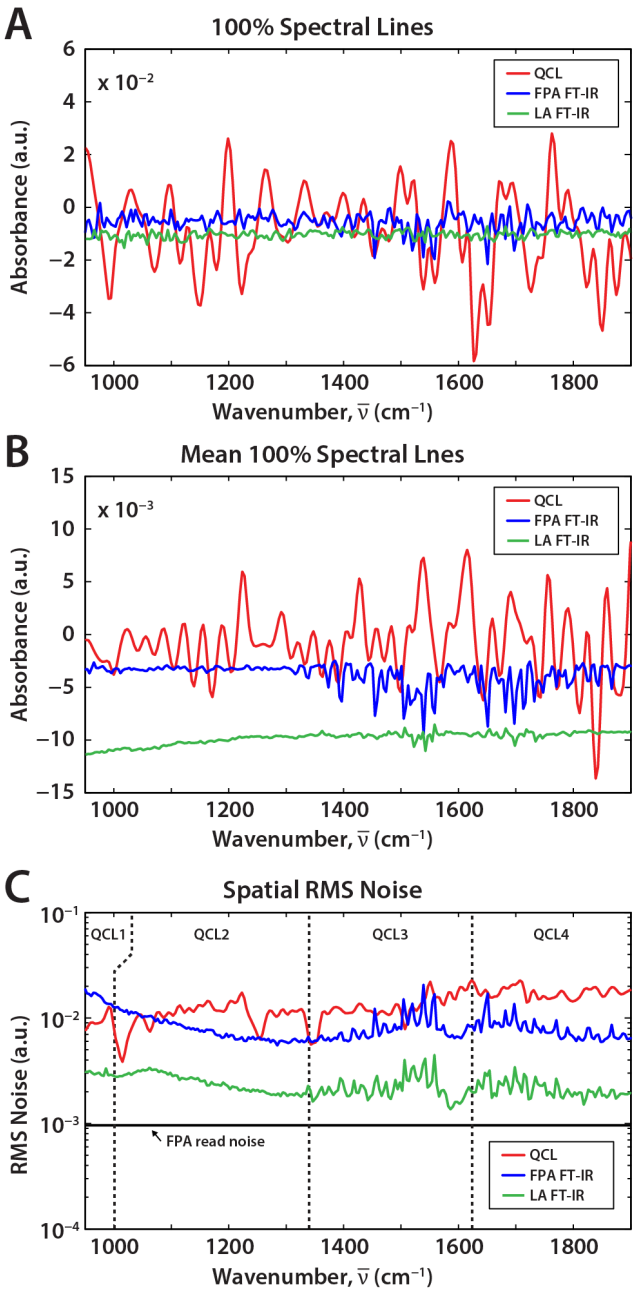

Figure 4.4. (A) 100% spectral lines extracted from randomly selected pixels on the sample substrate for the three imaging systems, all normalized to a single scan. (B) Averaged 100% spectral lines shows that the source (shot) noise persisting in QCL systems does not result in the same noise reduction as seen for the FT-IR (random noise) systems. (C) Spatial root mean square (RMS) variation in the 100% line shows that the random component of the FPA systems are the same while the LA-based system is significantly less noisy. The noise in an FPA frame from the detector is much smaller (FPA read noise), pointing to the significant potential for improvement in QCL-based systems.

We recognize that the performance of our system can be improved significantly over this first prototype and efforts are underway to do the same by a systematic analysis of noise. Here, it suffices to state that the spectral and temporal domains, in contrast to FT-IR spectroscopy, are not coupled. For any DF-IR spectrum, the spatial variation of the 100% line is not affected by shot-to-shot noise. Hence, we calculated the root-mean-square (RMS) absorbance for each wavenumber as shown in **Figure 4.4C**. This should provide the detector-dominated random noise for all cases. The noise contribution of the FPA to both the QCL and FT-IR imaging cases can be seen to be similar and both are significantly worse than the AC-coupled and filtered linear array. Note that there is potential for improvement as the FPA noise floor is significantly lower. Should innovative methods be developed to improve the performance of the QCL-FPA system, it may well rival the LA system's performance. The data presented in **Figure 4.4C** were all normalized for a single scan and do not take the actual scanning time into account. These numbers are simply raw performance measures and differences in optical configuration, spectral range and throughput need to be accounted for to accurately compare per pixel performance. For each setup, hence, we employ the typical experimental parameters (integration time, scanning rate) we use for biomedical tissue imaging. Under the parameters specified previously, a SNR of up to 260 was recorded for the QCL instrument for a single scan while imaging each tissue core in a tissue microarray (TMA) in approximately 2 minutes; in comparison, the FPA FT-IR spectrometer achieved a calculated SNR of 727 (16 co-additions, 2.5 hours/core), and the LA-equipped system reached an even higher SNR of 1034 (2 co-additions, 1 hour/core). Later in the manuscript, we discuss both the quality of the data as well as the SNR and speed implications to acquire data from tissue samples.

The spectra recorded by the QCL and FT-IR systems can also differ due to interference effects in using a spatially-coherent source. The scattered light from each sample point interferes with others within a certain coherence area, thus encoding the sample structure in the signal intensity measured by the detector. In **Figure 4.5**, we compare the breast tissue images acquired from each instrument and examine the spectra from the marked location. Each spectrum has been linearly baseline corrected and normalized to the amide I peak at 1656 cm^{-1}. We see that the spectra are well-matched between the DF-IR system and their FT-IR counterparts while the improvements in resolution are clearly evident.

The advantage of the QCL instrument is the ability of the DF-IR system to scan through large sample areas quickly at single wavelengths. Scans at a discrete frequency are only limited by the time it takes for the microscope stage to reposition. For any biological sample, multiple bands are required for tissue classification, so the limit in imaging speed involves the re-tuning time of the QCL instrument as well. To test the system for long term consistency regarding wavenumber tuning and pulse-to-pulse power output, we scan through all the cores available on a breast tissue microarray. The full BRC1501 TMA was acquired with the QCL microscope using the 0.56 NA objective (**Figure 4.6A**), resulting in a set of 55.3 Megapixel (9408x5880) images for each of the 282 wavenumber positions. The full scan area is approximately 1.5 cm by 2.5 cm so positional markers were assigned to each core to skip imaging empty space. This specific image is displayed at 1656 cm^{-1} on the amide I absorption band. Each tissue core is 1.1 mm in diameter and is scanned as a 5x5 frame mosaic in about 2 minutes with our parameters. In total, there are 149 tissue cores on this TMA, representing a scan time of roughly 5 hours. Three select cores are imaged at 2-fold increased resolution with the high numerical aperture objective in under 10 minutes each (**Figure 4.6B**).

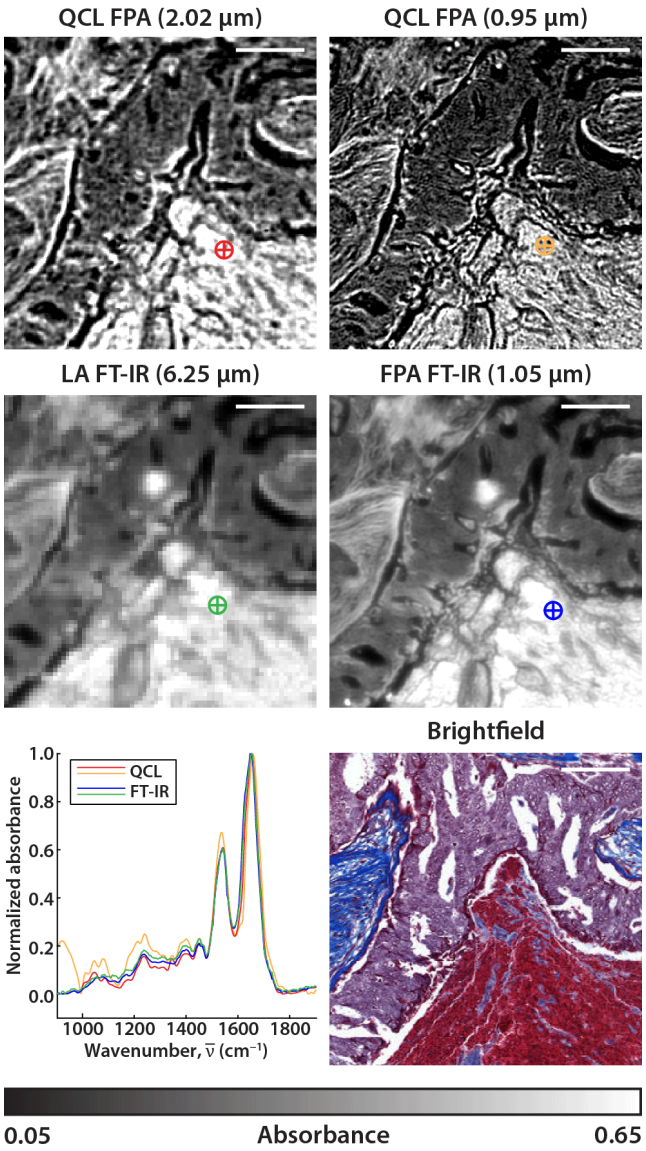

Figure 4.5. Images corresponding to the amide I absorption band at 1656 cm^{-1} from the C2 tissue core on the BRC1501 TMA are acquired by QCL and FT-IR instruments. A brightfield microscopy image of a Masson's trichrome-stained serial section from the same core is included. The 4 cm^{-1} resolution fingerprint region spectra from a single pixel, baseline corrected and normalized to the amide I band at the marked location on the images are compared between each system. The scale bars represent 100 µm.

The LA FT-IR instrument scans 1 core per hour, but at a 10-fold larger pixel size and a ~4-fold higher SNR as noted previously. As may be surmised, there is no simple way to compare these systems. We believe each is suited to its specific use – the QCL system for fast scanning at high spatial quality but limited spectral range, the FPA FT-IR system for HD full spectrum imaging, and the LA FT-IR system for collecting very high quality spectra. Nevertheless, it is

interesting to theoretically compare the systems by normalizing performance as per the trading rules of IR imaging where the pixel rate ratio (R) is proportional to the number of pixels (n), the acquisition time (t), and the resulting SNR.[75]

$$R_{21} = \frac{n_2}{n_1}\frac{t_1}{t_2}\left(\frac{SNR_2}{SNR_1}\right)^2 \qquad 4.5$$

Since SNR has a time-squared dependence, we can normalize each of these benchmarks for equivalent SNR, implying that the QCL system can provide the high quality of the LA system slightly faster (2-fold), albeit with 10-fold smaller pixels and the smaller spectral range. Hence, to a crude approximation, the QCL system can be approximated to be ~20-fold faster than a hypothetical LA FT-IR system. For another comparison, the FPA FT-IR instrument scanned at a rate of 2.5 hours per core with an FPA representing a 75-fold increase in time. When we normalize for the FPA FT-IR instrument's 3-fold higher SNR and its quarter pixel size, this implies that the QCL system is still ~2-fold faster per pixel in this case. These discussions demonstrate that the QCL microscope provides us the option of fast spectral scans at rates competitive with current FT-IR instruments.

The major advantage, however, of the DF-IR approach lies in the reduced spectral scanning. Should only a few frequencies be required, the QCL system advantage will increase proportionally. The linewidth of our laser is less than 2 cm^{-1}, and unlike FT-IR systems, the spectral resolving power does not diminish with scan time. The QCL data at 2 cm^{-1} contains ~550 bands and is presented undersampled by a factor of 2 such that it matches the 4 cm^{-1} resolution FT-IR systems. To examine a single vibrational mode, the FT systems do have to collect the entire spectrum whereas the QCL system will collect a single frequency, raising its speed advantage further by ~550-fold. This represents a net speed increase of over ~1100 fold per wavenumber over the fastest available HD FT-IR system. A major shortcoming of present QCLs is the truncated wavelength range. Should laser systems be developed to cover the full mid-range, it would only require 2-fold higher scanning times. Thus, the analytical advantages of using QCL-based systems are likely to persist. For scanning full spectral ranges, the advantage will be significant but will be impossible to match by FT systems for recording a few discrete frequencies.

We have demonstrated an initial design for a chemical imaging microscope employing QCL source for DF-IR wide-field imaging. This QCL microscope consists of three primary subsystems that must be developed in tandem for optimal performance. Current implementations of multiplexed QCLs are still in their first generation and could improve with respect to wavenumber tuning range as well as power output and pulse-to-pulse stability. With the higher flux of QCLs, this opens up the possibility of cameras with larger pixel formats, faster readout rates, shorter integration times, and deeper charge wells. MCT detectors, while being sensitive, also have drawbacks in linearity and background. Linearizing the photometric response of MCT detectors is likely to be important to account for the strong intensity variations of QCLs but we have refrained from examining this for now. For conventional MCT detectors, numerous strategies have been proposed,[3,83] including incorporating linearized preamplifier circuits calibrated for the given detector.[84] The optical performance of QCL-based microscopes is limited by the lack of commercially available high NA aspheric and achromatic microscope objectives in the mid-IR. IR reflective optics are not well suited toward tunable laser sources, and the majority of IR refractive optics are singlets prone to various aberrations. AR coatings typically run from either 3-5 μm or 8-12 μm while broad band AR coatings covering the full mid-IR are still limited to custom production optics. Innovations in optical design will likely be needed and spurred by the emergence of DF-IR microscopes. Lastly, a careful analysis of the data acquisition process and data is required to develop new signal processing techniques to handle the unique effects of laser coherence on the recorded spectral data as well as eliminate noise.

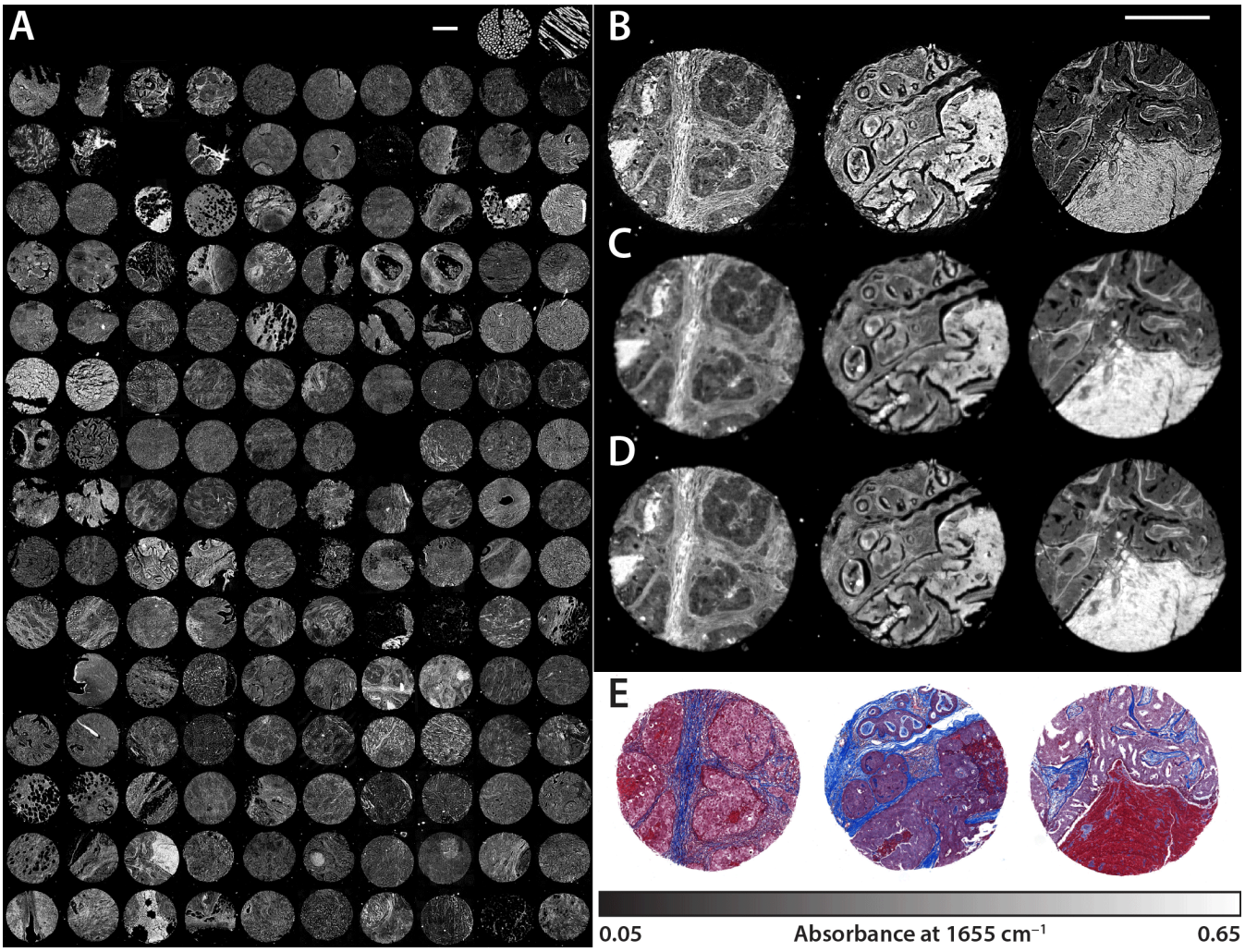

Figure 4.6. (A) Absorbance data of 149 tissue cores from the BRC1501 TMA acquired by the QCL microscope with the 0.56 NA (2.02 µm) objective. The net scan time of the fingerprint range from 776.9 to 1904.4 cm^{-1} at 4 cm^{-1} resolution was approximately 5 hours. Only the amide I absorbance band at 1656 cm^{-1} from the full spectral data set is displayed. Selected tissue cores (C2, C7, G5) are also imaged by the (B) QCL with the 0.85 NA (0.95 µm) objective, (C) LA FT-IR (6.25 µm), and (D) FPA FT-IR (1.05 µm). (E) A brightfield image of a serial core section treated with Masson's trichrome stain as performed in traditional histological studies. The scale bars in all images represent 500 µm.

4.5 Conclusions

In our current implementation of the QCL microscope, the spatial resolving power surpasses that of the best commercial FT-IR imaging instruments while improvements in spectral quality have reached competitive levels. The QCL approach offers higher speeds for scanning large tissue arrays, but the nature of the DF-IR system is such that much smaller times become

accessible for certain types of measurements. The complexities of working with a coherent source are ongoing issues but the data demonstrate little difference from traditional globar sources to a first approximation. Using careful integration and post-processing, we were able to achieve ~(1100/*N*)-fold speedup for measuring the *N* essential spectral features of tissue. This enabled very large images (>50 Megapixels) to be acquired rapidly at high quality. These improvements in DF QCL imaging instrumentation, combined with further ongoing developments, will greatly enhance our ability to perform fast and efficient chemical imaging in cells and tissues.

CHAPTER 5: VERSION 2.0 – POINT RASTER IMAGING [§]

5.1 Abstract

Infrared (IR) spectroscopic imaging is an emerging modality for biological tissue analysis that has traditionally employed an interferometer for spectral discrimination. Recent technology developments have made discrete frequency sources, both lasers and filters, practical for imaging. The use of quantum cascade lasers in particular, presents new opportunities as well as challenges. Here we describe results from a novel point scanning confocal IR microscope and demonstrate the performance imaging several important spectral bands of lung tissue. Results show the possibility of discrete frequency (DF) absorbance measurements with RMS noise levels down to 0.34 mAU in 0.25 ms.

5.2 Introduction

Chemical and structural measurements of biological tissues can reveal important information that can aid a wide variety of research and clinical diagnostic interests. This information is commonly obtained by processing the sample in various dyes and probes that highlight specific targets before viewing these contrast-enhanced samples with optical microscopy. For a full histological analysis, multiple slices of samples are typically acquired and each processed with a different protocol. Infrared (IR) spectroscopic imaging is a newer technique that investigates samples without perturbing it by interactions with mid-infrared light and measuring absorption levels.[52] The most popular approach, Fourier-transform infrared spectroscopy (FT-IR), offers many advantages as it is capable of thorough measurements over a large wavelength range that allow measurement of a wide variety of biomolecular species.[3,22,34,69] Recent advances in high quality imaging[25,55] and relations to clinically-used images [85] provide further impetus for biomedical translation.[86] The intrinsic nature of the Fourier-transform and interferometry, however, necessitates that all wavelengths are acquired regardless of whether they are useful for final diagnostics or not. The discrete frequency infrared (DF-IR) spectroscopic microscopy technique is advantageous when the specific set of wavelengths that

[§] The work in this chapter has previously been published and is reprinted with permission.

Yeh, K.; Bhargava, R. Discrete Frequency Infrared Imaging Using Quantum Cascade Lasers for Biological Tissue Analysis. In *SPIE*; Mahadevan-Jansen, A., Petrich, W., Eds.; **2016**; Vol. 9704, p 970406.

can discriminate the sample are already known.[31,68] Consequently, only the wavelengths useful for analysis are acquired thus resulting in a significant improvement in data efficiency.

While initial approaches used filters,[77,87] the recent use of quantum cascade lasers (QCL) for DF-IR microscopy has provided new opportunities for investigations by several groups.[64,65,79–82,88–91] While the speed of these systems can potentially exceed that of FT-IR instruments, the spectral quality of these interferometer based instruments is still unmatched. The use of a coherent source for wide-field imaging presents numerous challenges that can adversely affect the quality of the absorbance measurements. Many of these issues are largely mitigated by point scanning. Lasers are often used with point scanning confocal instruments since their spatial and temporal coherent properties are advantageous in creating a spot that is tightly focused and far brighter than what an extended source is capable. Additionally, the spatial filtering properties of the confocal design rejects out of focus light that scatters from the sample due to the relatively high coherence of the laser source. Here we present a low-noise point scanning microscope and show preliminary data demonstrating its performance on calibration targets and tissue samples.

5.3 Instrument Design

The instrument we have developed incorporates a widely-tunable quantum cascade laser with a confocal reflection microscopy optical system as shown in **Figure 5.1A**. The laser assembly contains four individual laser modules arranged in collinear geometry (Block Engineering, Marlborough, MA) which together span a tuning range from 777 to 1940 cm^{-1}. A microscopy stage (H101A ProScan III, Prior Scientific, Rockland, MA) raster scans the sample. The reflected beam is focused onto a 25 μm active area MCT detector (MCT-13-.025, InfraRed Associates, Stuart, FL). Data acquisition and synchronization are handled by a high-speed digitizer and a multifunction data acquisition card (PCI-5122 and PCIe-6361, National Instruments, Austin, TX).

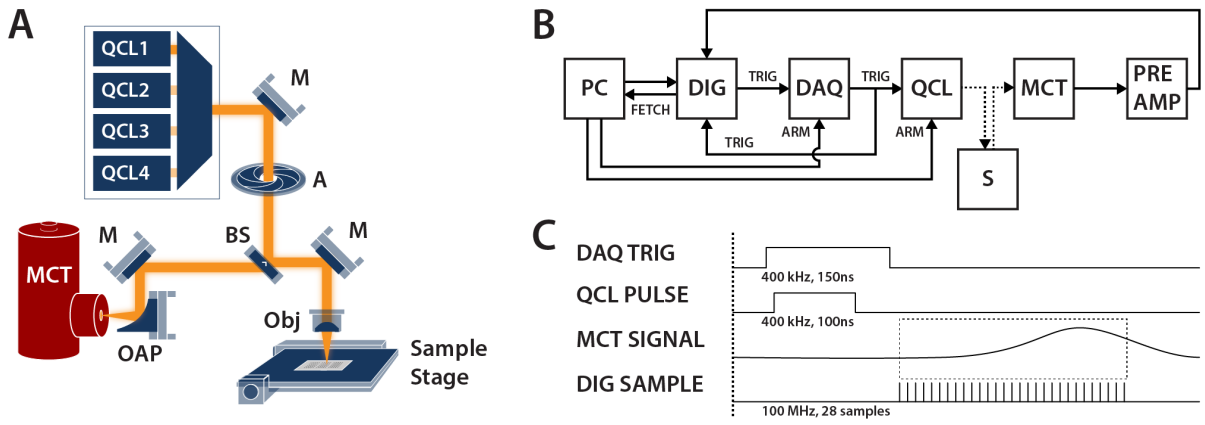

Figure 5.1. (A) A schematic layout of the microscope setup in a reflected confocal geometry. (B) The functional blocks of system showing the data flow between components. (C) The trigger cascade through the system digitizes each individual laser pulse.

The synchronization of this equipment is shown in **Figure 5.1B**. In the first stage, all the equipment is initialized and armed. Once the digitizer is software triggered to collect N samples, the rest of the low-latency cascading hardware triggers. The DAQ, after receiving the start trigger from the digitizer, sends a TTL pulse to both the QCL and back at the digitizer. On the rising edge of this pulse, the QCL files one laser shot. The duration of the DAQ trigger corresponds to the latency of the QCL. Therefore, the falling edge of the trigger is used to begin digitizer acquisition. The MCT signal is digitized at 100 MHz with 28 samples. While this is not sufficient to capture the whole pulse, we only need the rising profile since the signal's falling profile is predictably a capacitor discharge. Furthermore, 28 samples is the most efficient use of bandwidth given the way the digitizer stores sample data into packets for transfer.

Since the detectors are configured in AC coupled mode, and this waveform is non-symmetric, the baseline value will shift such that the average value of the entire signal is zero. By comparing the two traces in **Figure 5.2A**, the baseline shift increases as the overall intensity increases. To minimize sampling noise, the waveforms are processed with a Blackman window filter to smooth out any irregularities. Finally, the single beam intensity is calculated as the integral of the filtered waveform over the DC baseline. One of these traces was acquired on a reflective background and the other on a partially absorbing material. The signal difference represents the absorption. In this figure, 100 individual laser pulses are overlaid. It is clear that

laser fluctuations, which can depend on wavenumber, as opposed to FT-IR systems in which detector noise is dominant, will be the primary source of noise.

This system is capable of generating one absorption measurement per pulse of the laser. While the laser can fire up to 2 MHz, the current ideal repetition rate is 400 kHz limited by the acquisition electronics. Taking per pulse measurements allows this system to accumulate a large number of co-additions very quickly in order to achieve the target noise characteristics. The noise seen here is not atypical – some wavenumbers will have much less noise where co-additions are not required, and some will have far more. For the low noise wavenumbers, the response time of the system can be on the order of a few microseconds thus allowing the system to measure absorbance changes of very transient events.

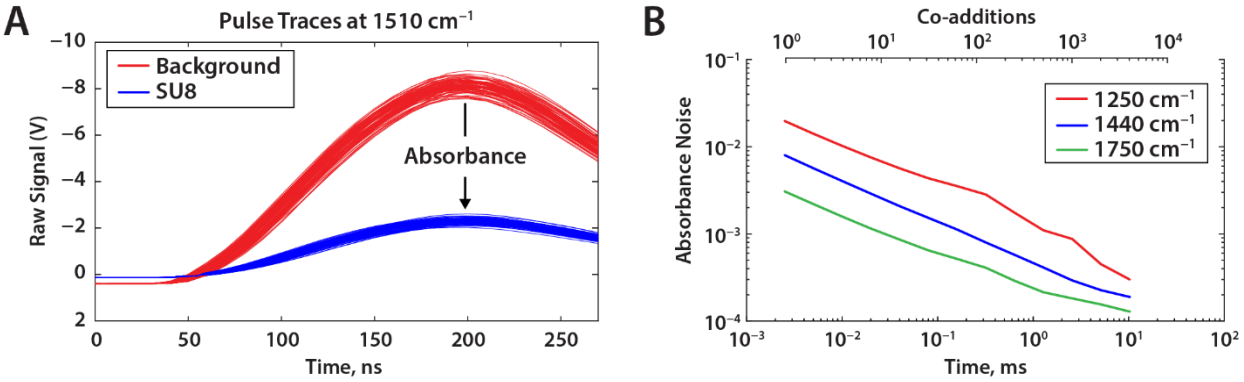

Figure 5.2. (A) Individual laser pulses (100 overlaid traces) on a reflective surface and on a 5 µm layer of SU-8 polymer are individually digitized and used to calculate absorbance per shot. The pulse-to-pulse noise shown at 1510 cm^{-1} is wavenumber dependent and can vary drastically. (B) The noise level can be tuned for each wavenumber by adjusting the number of laser pulses averaged. Three example wavenumbers at 1250, 1440, and 1750 cm^{-1} are shown.

Prior to imaging, the instrument is initialized with an autofocus subroutine that generates a z-shift map as a function of x and y coordinates as well as wavenumber. This corrects for chromatic focal shift as well as sample tilt, both of which can affect absorbance measurements. The autofocus routine first creates a rough z-map attempting to find the global signal maximum. The initial search is coarse which prevents the system from tuning to a local maxima of the axial point spread function. This search range is recursively expanded or contracted depending on the intensity measurements. Unless the system is severely out of focus, this coarse search is normally only performed once and can be overridden if, for example, the system recently found the focal position of an adjacent wavenumber. When the approximate focal window is found, the final

position is calculated by curve fitting the nearby data to a 3-term polynomial and then using this fit to determine the z position of the focus. By iterating across all wavenumbers, we generate a chromatic shift map that is eventually fitted and the coefficients saved for later use in calculating fine focal adjustments. A similar subroutine calculates sample tilt by autofocusing on several sample coordinates and using this data to best-fit a plane. Both calibrations are combined and stored to be called later for fine adjustments during data acquisition. Once the single beam image is acquired, the blank regions on the image are automatically masked out and used to generate a background image. The missing background data is then extrapolated via plane fitting. In the event that no background areas are available in the image, a previously stored background value is used instead, which will also result in less accuracy. The absorbance of the image is then computed by the negative base 10 logarithm of the transmission ratio. Since this is a reflection measurement, to account for the double pass through the sample's thickness, the final absorbance value is halved in order to obtain comparable data with transmission measurements.

The system is controlled with custom software written in C# .NET Framework (Microsoft, Redmond, WA) and Labview (National Instruments, Austin, TX). Post-processing and visualization are handled with MATLAB (The MathWorks, Nantucket, MA), ENVI (ITT Visual Information Solutions, Boulder, CO), and ImageJ (National Institutes of Health, Bethesda, MD).

5.4 Experimental Results

The performance of this microscope is tested by imaging a 1951 USAF resolution target. The target has between patterned with a 5 μm layer of SU-8 photoresist, a thickness commonly used for tissue sectioning. This allows us to test both the spatial and spectral of the instrument simultaneously. The region imaged with pixel sizes of 2 μm, shown in **Figure 5.3A**, contain groups 4 and 5 of the target which cover a 1 by 1 mm square. These smallest resolvable features in these targets according to the Rayleigh criterion are group 6 element 1 bars, which are 7.8 μm wide. This corresponds with the theoretical Rayleigh resolution limit, thus demonstrating diffraction limited imaging using a 0.56 NA objective. The spectrum is taken from the center square, post-processed using a 3-term lowpass filter, and compared with a FT-IR spectrum acquired with a Perkin-Elmer Spotlight microscope at the same location.

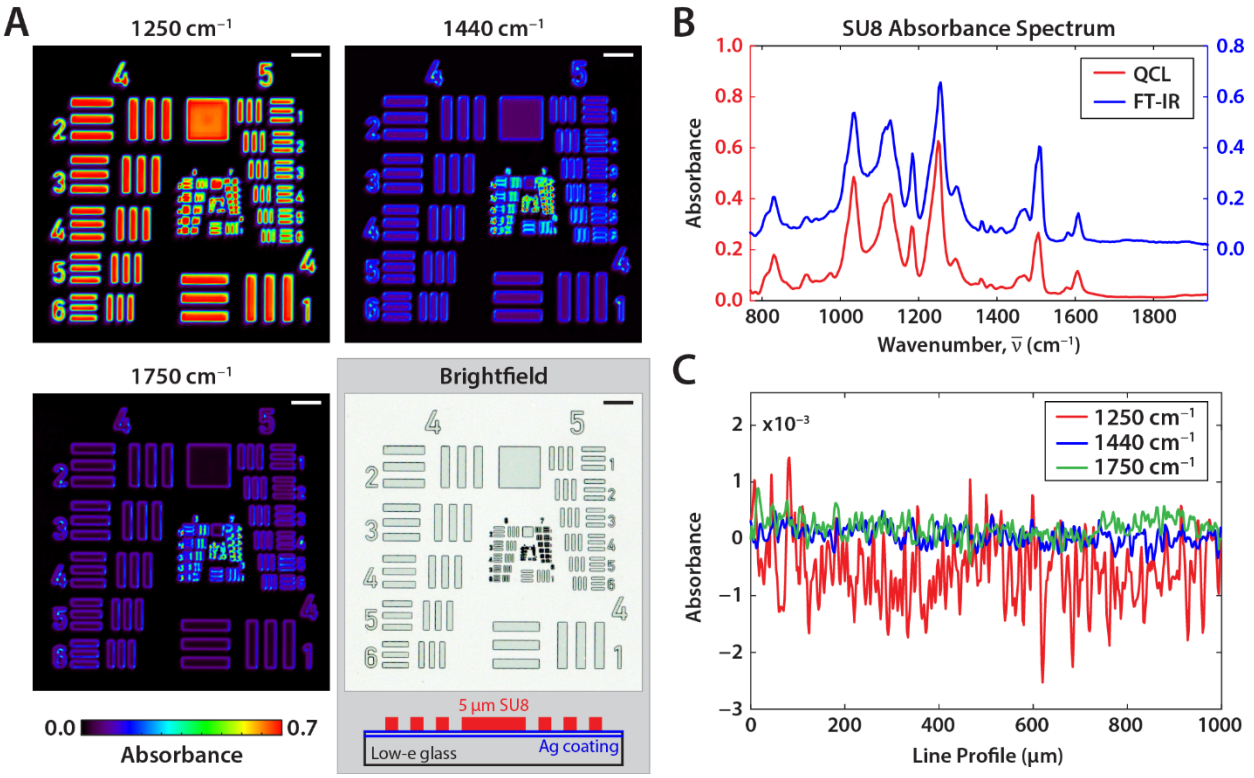

Figure 5.3. (A) The system was tested by imaging a 1951 USAF resolution test target fabricated with at 5 µm layer of SU-8 photoresist on reflective low-emissivity glass. Three wavenumbers are shown at 1250, 1440, and 1750 cm^{-1} representing regions in the spectrum with high, medium, and low absorption respectively. A reflectance brightfield image is shown for comparison. The images are 1 mm^2 and the scale bars represent 100 µm. (B) The spectrum taken from the center of the large square between groups 4 and 5 show good agreement between the QCL data and reference FT-IR data. (C) A line profile across an empty region of the target are shown at each of these wavenumbers.

As expected from using a point scanned approach, no speckle arising from laser illumination is visible in these images. In fact, the noise is far below the visible noise threshold when converted to 8-bit color for display which displays a maximum signal-to-noise ratio (SNR) of 256. The background noise levels, show in **Figure 5.3C**, are calculated from a spatial 100% line profile across the image. The RMS noise of each of these 3 traces are 1.1, 0.36, 0.34 mAU for 1250, 1440, and 1750 cm^{-1} respectively. If we assume a maximum signal of 1 AU for a typical sample, the previous noise values correspond to SNR of 900 to 3000. These SNR values can be fine-tuned to the desired result shown in **Figure 5.2B** at the cost of time. For this image, each absorbance measurement was acquired in 0.25 ms. The true maximum signal depends on the absorption of a particular sample and can be varied depending on the thickness of the SU-8 layer patterned or how the sample is sectioned. The noise on the sample, as opposed to the

background measured previously, will always be lower due to lower signal values. Such measurements are typically less accurate due to their reliance on sample uniformity.

The instrument was also tested on a section of mouse lung shown in **Figure 5.4**. In this image we clearly see the many small respiratory ducts and alveoli as well as large bronchiole consistent with lung tissue. Veins and arteries are also visible in the enlarged images. This sample is 12 by 6.75 mm and acquired at 1664 cm^{-1} with the small sub-region acquired at 4 key wavenumbers in the fingerprint region. The 1664 cm^{-1} and 1556 cm^{-1} frequencies correspond to the amide I and II absorption bands respectively, while 1080 cm^{-1} and 1240 cm^{-1} are often indicative of the presence of epithelia and stromal tissues. When we normalize the color scales in **Figure 5.4B** to the amide I band we see clear absorption variations attributed to the different tissue types present in the image. The spectral curves of corresponding regions marked are shown in **Figure 5.4C**. Analysis of these key bands in the fingerprint region can then be used to classify tissues into various types as well as identify possible disease markers.

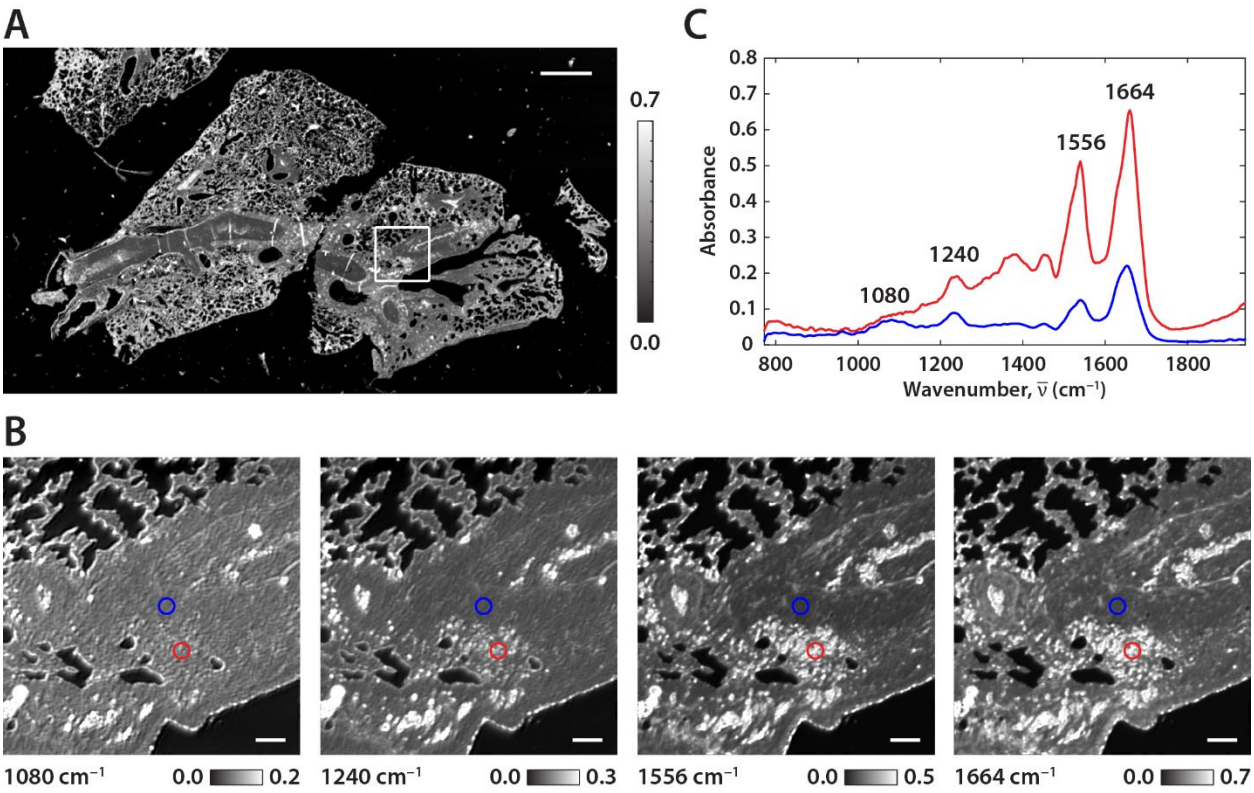

Figure 5.4. (A) An image of a section of mouse lung tissue is acquired at 1664 cm^{-1} corresponding to the amide I absorption band. The scale bar represents 1 mm and the region marked by the square is displayed below. (B) Detail of the tissue is shown at 1080, 1240, 1556, and 1664 cm^{-1} bands which are important for tissue classification purposes. These images have been color scaled to the amide I band in order highlight differences in relative absorption. The scale bars represent 100 μm (C) The full fingerprint spectra are shown at the regions marked below.

5.5 Conclusion

We have demonstrated the use of a QCL for point scanning reflected infrared microscopy. The use of coherent illumination for a point scanning approach is advantageous over a wide-field design in terms of the achievable spatial and spectral accuracy. However, due to the multiplexing advantage of focal plane array cameras used under wide-field illumination, point scanning instruments will be slower. Both technologies are well-suited for their specific use. With this point scanning approach we are able to achieve SNR approaching 3000 in sub-millisecond times. Our continuing developments in the area of mid-infrared point scanning microscopy, including further improvements to the electrical and optical design, will aim to maintain SNR while improving acquisition speed in order to accelerate imaging performance.

Nevertheless, this instrument provides the means to perform experiments involving very low absorbing materials or measuring very transient absorption changes.

CHAPTER 6: VERSION 2.1 – CONFOCAL STAGE SCANNING IMAGING [**]

6.1 Abstract

Histopathology based on spatial patterns of epithelial cells is the gold standard for clinical diagnoses and research in carcinomas; though known to be important, the tissue microenvironment is disregarded in decision-making due to the onerous need for multiple staining and complex interpretation. Here we demonstrate accurate subtyping from molecular properties of epithelial cells using emerging high-definition Fourier transform infrared (HD FT-IR) spectroscopic imaging combined with machine learning algorithms. In addition to detecting four epithelial subtypes, we simultaneously delineate three stromal subtypes that characterize breast tumors. While the work enables fully digital pathology with rich information content, the long spectral scanning times required for signal averaging and processing makes FT-IR imaging impractical for routine research or clinical use. Hence, we developed a new confocal design in which refractive IR optics are designed to provide high-definition, rapid spatial scanning and discrete spectral tuning using a quantum cascade laser (QCL) source. This instrument provides simultaneously high resolving power (2 μm pixel size) and high signal-to-noise ratio (SNR > 1300), providing a speed increase of ~50-fold for scanning tissues compared to present imaging spectrometers. We demonstrate spectral fidelity and inter-instrument operability of our developed instrument by accurate analysis of a 100 case breast tissue set that was analyzed in a day, considerably speeding research. Clinical breast biopsies typical of a patients' caseload are analyzed in ~1 hr. This study paves the way for comprehensive tumor-microenvironment analyses in feasible time periods, presenting a critical step in practical label-free molecular histopathology.

[**] The work in this chapter has previously been published and is partially reprinted with permission here in abbreviated form. Please refer to the citation for the full manuscript.

Mittal, S.*; **Yeh, K.***; Leslie, L. S.; Kenkel, S.; Kajdacsy-Balla, A.; Bhargava, R. Simultaneous Cancer and Tumor Microenvironment Subtyping Using Confocal Infrared Microscopy for All-Digital Molecular Histopathology. *Proc. Natl. Acad. Sci.* **2018**, *115* (25), E5651–E5660.

6.2 Significance Statement

Cancer alters both the morphological and the biochemical properties of multiple cell types in a tissue. Generally, the morphology of epithelial cells is practical for routine disease diagnoses. Here, infrared spectroscopic imaging biochemically characterizes breast cancer, both epithelial cells and the tumor-associated microenvironment. Unfortunately, conventional spectral analyses are slow. Hence, we designed and built a new laser confocal microscope that demonstrates a high signal to noise ratio for confident diagnoses. The instrument cuts down imaging time from days to minutes, making the technology feasible for research and clinical translation. Finally, automated human breast cancer biopsy imaging is reported in ~1 hr, paving the way for routine research into the total tumor (epithelial plus microenvironment) properties and rapid, label-free diagnoses.

6.3 Introduction

Histopathology is essential for both research and clinical management in a variety of diseases, including cancer. The diagnostic process relies on staining thin tissue sections, followed by a pathologist manually recognizing epithelial morphology and patterns using an optical microscope. While carcinomas originate in epithelial cells, it is now well understood that stromal (both cellular and extracellular) characteristics aid cancer progression[92,93] and determine clinical outcomes.[94,95] Though holding tremendous potential for observing, understanding and treating cancer, stromal changes are not routinely used for research or clinical diagnoses. This arises from a lack of practical technology to capture morphological and biochemical patterns; multiplex staining is time consuming and expensive, generally limited to proteins and results are difficult to interpret. Computerized pattern recognition has been reported[95] to be effective in utilizing stromal signatures but digital data has been limited to simple structural data or highly detailed but time-consuming molecular measurements.[96–102] Methods based on optical vibrational spectroscopy[85,103,104] provide an avenue as they offer the same image scale and quality as traditional pathology, can be coupled to computational analysis,[69] show contrast between different cell types and disease,[52] and are sensitive to changes in both cells and extra-cellular material.[105,106] Moreover, label-free spectroscopic imaging does not perturb the tissue samples in any way, and can be computed to resemble conventional stained (H&E or molecular) images,

enabling integration into clinical or research workflows.[103] Laboratory studies using tissue microarrays (TMA) using Fourier Transform Infrared (FT-IR) imaging,[34,107,108] for example, have provided extensive demonstration of this potential. Fundamental molecular vibrations provide strong signals across a spectral region (800 cm^{-1} – 4000 cm^{-1}) 20-fold larger than the visible spectrum making it efficient and ideally suited to thin sections commonly used in pathology.

Despite extensive histologic studies, there are no reports of tumor staging and tumor microenvironment use for (a) diagnostically relevant accuracies, and (b) reasonable analysis times. These two factors are related. Data acquisition is slow compared to optical microscopy as thousands of spectral frequencies need to be acquired.[109] A necessary trade-off to make imaging practical is to use larger pixel sizes; but large pixels result in biochemical averaging of the heterogeneous microenvironment reducing the chemical contrast. This spatial averaging over a 10 μm scale in turn necessitates exceptionally high signal to noise ratio (SNR) to resolve small differences, complex analysis models[110] and high computational overhead. The limits of pixel sizes are now established, with rigorous optical modeling fueling new instrumentation that provides so-called high-definition (HD)[25,55] images, in which pixels are ~25-100 times smaller than previously used. While understanding of optical design has been transformed, two unresolved issues persist: first, *n*-fold smaller pixel areas require *n*-fold more pixels scanned per specimen and *n*-fold less available light (SNR) per pixel; together these imply ~n^2 larger scan time just to maintain SNR. Second, there is no evidence yet to show that HD imaging offers an analytical advantage beyond image quality. The smaller pixels may well need higher SNR and sub-cellular heterogeneity may need yet more complex computations. Together, there appears to be no obvious pathway with current technology to clinically feasible, HD imaging that allows confident information extraction from both the tumor and microenvironment in real time.

This study focuses on three major advances: discovery of diagnostically useful tumor microenvironment classes along with precise detection of epithelial stages, development of a new high performance discrete frequency IR microscope, and a first demonstration of high-definition chemical characterization of human biopsies in clinically feasible times. First, we seek to develop confident tumor and microenvironment detection using HD FT-IR imaging. While there have been prior studies on breast tissue and its microenvironment using IR imaging,[111–116] there are no reports of clinically feasible epithelial and microenvironment protocols. One

challenge is to acquire consistent information that allows computerized recognition despite the tissue heterogeneity arising from small pixels. The underlying complexity is that the types and number of classes of microenvironment associated with disease are unknown. Hence, the first section of this study focuses on discovering a small number of characteristic microenvironment responses to cancer potentially making diagnoses feasible. This fundamental understanding can broadly impact pathology as a step towards utilizing microenvironment information but must be translated to an approach with practical imaging times. Hence, second, we seek new instrumentation to overcome current limitations. Recently, high-intensity, broadly tunable quantum cascade laser (QCL) sources have enabled rapid discrete frequency IR (DFIR) imaging,[56,88,117,118] especially for problems in which the data dimensionality can be significantly reduced[68] by using a smaller set of frequencies.[79,91,119–122] In current designs, however, laser coherence can degrade image quality and can subtly distort spectra. This distortion affects pattern recognition accuracy in an unpredictable manner due to its dependence on local structure and/or SNR. We systematically address these challenges by engineering a new IR microscope. While providing new analytical capabilities, this advance is useful for tumor staging and microenvironment analysis in breast cancer. We subsequently validate this confocal microscope design and ensure its capabilities in providing diffraction limited imaging with minimal noise and aberration. This enables accurate histological and pathological segmentation of tissue that was not previously possible. Next, we adapt the FT-IR epithelial subtyping and stromal differentiation using a discrete frequency model to this instrument and assess its accuracy. Finally, in the third part of this report, we image tissue biopsy samples and demonstrate automated tumor-microenvironment classifications for breast cancer in clinically feasible time.

6.4 Methods

6.4.1 Quantum cascade laser confocal microscope

The QCL confocal microscope consists of a quantum cascade multi-laser source (Block Engineering, Marlborough, MA, USA) that contains four individual tuner modules with beams combined into a single collinear output spanning the mid-infrared fingerprint region from 770-1940 cm^{-1}. The general layout is illustrated in **Figure 7.1**. The alignment of these tuners is assisted by a two-axis galvanometer pair (θ_{XY}) (6215H, Cambridge Technology, MA, USA).

Imaging is performed by two interchangeable high numerical aperture (NA) aspheric collimating lenses with 0.56 NA and 0.85 NA (LightPath Technologies, Orlando, FL, USA) that focus the beam to a diffraction limited spot. Complicated aberration corrected optics are not required as the instrument design compensates for many optical aberrations. When imaging via high-speed stage scanning (HLD117, Prior Scientific, Rockland, MA, USA), all optics are illuminated with a zero-field angle where performance is optimal. Off-axis light rays due to scattering are rejected by the illumination (A_I) and detection (A_D) apertures limiting the focal area thus increasing resolution and minimizing aberrations. The instrument also corrects for chromatic distortion using a calibration curve generated in optical design software (Code V, Synopsys, Pasadena, CA, USA). The instrument is also capable of running an autofocus subroutine per wavenumber by sweeping the axial position of the objective maximizing the signal.

The laser is split using a KBr beam splitter (BS) (Spectral Systems, Hopewell Junction, NY, USA) with half discarded (BB) and the rest used to illuminate the sample in transflection mode. Light is absorbed by the sample and the remaining intensity is focused onto a cryogenically cooled, 0.5 mm active area, photovoltaic Mercury Cadmium Telluride (MCT) detector with matched preamplification (MCT-13-0.5PV and MCT-1000PV, InfraRed Associates, Stuart, FL, USA) using a 100 mm focal length parabolic mirror (OAP). After preamplification, the detector signal (V_{AC}) is measured with a lock-in amplifier (MFLI, Zurich Instruments, Zurich, Switzerland). A data acquisition card (PCIe-6361, National Instruments, Austin, TX, USA) generates the pulse reference frequency for the laser and the lock-in amplifier as well as the analog drive signal for the galvanometer pair. The demodulator samples are triggered by the stage encoder and the magnitude (R) of the demodulator vector represents the pixel intensity. Since the stage velocity is not constant, this minimizes distortion since the image is formed as function of spatial distance rather than time. At 2 μm pixels, approximately half the size of the point spread function (PSF) and the lowest wavelength, with 50 nm encoder spacing, the counter outputs a single TTL pulse per 40 ticks (Enc_{XY}). The instrument can acquire images at any resolution as long as the pixel size is rounded to an integer multiple of the encoder spacing.

System performance is optimally stabilized by automatically adjusting several important parameters when tuning the laser including repetition rate, pulse width, pointing angle, and detection sensitivity. These parameters are saved as a system configuration file for a subset of

wavenumbers, typically the key classification bands. For hyperspectral scans where a predefined configuration is not available, a default set still provides acceptable performance for most wavenumbers. When a scan is first initiated, two subroutines are performed. First, the instrument finds the optimal focal point at various points across the scan field and calculates the best fit plane that represents the substrate. The autofocus algorithm sweeps across z coordinates while monitoring the detector signal, which approximately follows a sinc-squared profile, until the global maximum is found. First, the operator must bring the sample near the focal point before the automation takes over the remaining fine adjustments. During the search, the signal is smoothed and the search window restricted to > 5 μm in order to avoid converging onto errant local maxima. We autofocus only on bare substrate in order to avoid situations where the reflection off the sample surface exceeds the transflected signal resulting in an offset to the desired focal point. All system coordinates are then transformed by this matrix so its accuracy is critical. Small tilts can defocus the image by several microns for large specimens and create artifacts such as fades and ripples. The plane is shifted axially depending on the focal point of the objective at the specified wavenumber. Secondly, the system performs a test sweep calculating the minimum pixel dwell time as a function of stage velocity and setting the lock-in amplifier time constant to one third this value. The instrument scans in both directions, creating a forward image and a backward image.

For each image, the background intensity is generated by surface fitting against empty regions of the image, predominantly along the edges. This compensates for slow power fluctuations as well as any residual sample tilt leftover from the mechanical correction. Forward and reverse images are then interlaced. These images have an offset due to system delays. When the pixel is triggered, assuming a constant time delay, will still result in a spatial delay since velocity is constantly changing. The instrument records data throughout most of the acceleration period in order to maximize acquisition time. Any residual distortions are a function of velocity and signal delay. They are small, approximately 0.02%, yet result in a misalignment gradually increasing to a several pixels over 10s of millimeters. Therefore, aligning the odd and even rows in these forward and reverse images is a non-rigid image registration task. We estimate these local distortions and the displacement field that registers the reverse scan with the forward scan and the corrected images are warped and resampled using the original pixel grid (MATLAB, MathWorks, Nantucket, MA, USA). Next, to compensate for microscope drift over time arising

from environmental changes, we register the adjacent wavenumber bands and aligning the entire stack using affine transforms (ImageJ, National Institutes of Health, Bethesda, MD, USA). Lastly, the point spread function (PSF) of the optics at each wavenumber is simulated and used to deconvolve[123] the image according to the Tikhonov-Miller algorithm. The spectral images are rubber band baselined and visualized in ENVI+IDL (ITT Visual Information Solutions, Boulder, CO, USA).

6.4.2 FT-IR imaging

HD FT-IR imaging was conducted using a 680-IR spectrometer coupled to a 620-IR imaging microscope (Agilent Technologies, Santa Clara, CA, USA) at 0.62 NA with a liquid nitrogen cooled mercury cadmium telluride (MCT) 128×128 focal plane array (FPA) detector. Data were acquired over the 900-3800 cm^{-1} spectral range and averaged over 32 scans per pixel. Afterwards the images were corrected against a background acquired in an empty space of BaF_2 slide with 120 scans and Fourier transformed. The spectral resolution was 4 cm^{-1} with a nominal pixel size of 1.1 μm was obtained at the sample plane. Resolutions Pro software was used for data collection and preliminary data processing. Each sample was imaged by raster scanning a ~140 x 140 μm tile. Each of these tiles took approximately 2 minutes for scanning and 30 seconds of processing. The individual spectroscopic image tiles were imported into ENVI+IDL 4.8 and mosaicked using in-house software. This was further processed using Minimum Noise Fraction (MNF) for noise reduction. FT-IR images were manually labeled using correlation with the consecutive marked H&E stained glass slide images under the supervision of a pathologist as ground truth for our analysis. A tissue mask based on intensity of Amide I band was applied, in order to remove empty spaces and debris from further analysis.

6.4.3 Sample preparation

A paraffin embedded serial breast tissue microarray (BR1003, US Biomax Inc. Rockville, MD, USA) consisting of a total of 101 cores of 1 mm diameter from 47 patients was obtained. Two sections were stained with hematoxylin and eosin (H&E) and smooth muscle actin (SMA) and imaged with a light microscope. Corresponding 5 μm thick adjacent unstained sections of the TMA were placed on a BaF_2 salt plate for transmission FT-IR imaging and on a low-

emissivity glass (MirrIR, Kevley Technologies, Chesterland, OH, USA) for reflective QCL- IR imaging. The sections were deparaffinized using a 16 h hexane bath.

6.4.4 Test target fabrication and microscope calibration

The QCL confocal microscope was calibrated using a negative chrome on glass USAF 1951 test target (II-VI Max Levy, Philadelphia, PA, USA) as well as a SU-8 photoresist target to evaluate spectral fidelity. The multispectral images were acquired in transflection configuration at 2 μm resolution with the 0.56 NA objective, at 1 μm resolution with the 0.85 objective, and at 12 distinct spectral frequencies from the fingerprint region. Point spectra were acquired at 1 cm^{-1} resolution.

6.4.5 Classification models

A classification model developed in a study[124] using FT-IR data was adapted for the DF-IR capabilities of this microscope. The predominant few features in the fingerprint region responsible for class differentiation were identified and this selection of DF-IR bands, representing the top 7 metric definitions from the original FT-IR classifier, and their associated biochemical significance are described in the subsequent tables below.

Metric Definitions for QCL Data		
$\mathbf{H_{1082} : H_{1238}}$	$\mathbf{H_{1386} : H_{1238}}$	$\mathbf{H_{1658} : H_{1546}}$
$\mathbf{A_{984,\underline{1082},1143} : A_{1143,\underline{1238},1278}}$	$\mathbf{A_{1143,\underline{1238},1278} : A_{1353,\underline{1386},1483}}$	$\mathbf{A_{1483,\underline{1546},1587,1765} : A_{1483,1587,\underline{1658},1765}}$ $\mathbf{A_{1353,\underline{1386},1483} : A_{1483,1587,\underline{1658},1765}}$

Table 6.1. 7 metric definitions used in all the QCL classification models. Abbreviations: H: Peak Height; A: Peak Area at the indicated the wavenumber. For instance, the H_{1546}: H_{1658} indicates the peak height ratio of 1546 cm^{-1} and 1658 cm^{-1} wavenumbers and $A_{1483,1587,\underline{1658},1765}$ represents the spectral area of the 1658 cm^{-1} peak (underlined) calculated from these bounds.

Peak (cm^{-1})	Commonly accepted Biological species/ Functional Group Assignment	IR Band Assignments
1082	DNA/RNA	PO_2 symmetric stretch
1238	DNA/RNA	PO_2 asymmetric stretch
1386	Aliphatic groups	CH_3 symmetric bend
1546	Amide backbone	N-H bend and C-H stretch
1658	Amide backbone	C=O stretch

Table 6.2. Biochemical significance of absorbance peaks[125].

Metric	Biochemical Significance
$\mathbf{H_{1545}: H_{1653}}$	Amide II to Amide I ratio indicates protein profile of the sample both in composition and secondary structure
$\mathbf{A_{1387}: H_{1653}}$	Relative concentration of aliphatic groups compared to proteins and also composition of different proteins
$\mathbf{A_{2873}: H_{2916}}$	Aliphatic chain length and the extent of branching. This is important to distinguish between the different types of stroma and capturing differences in the composition of the amino groups
$\mathbf{A_{1080}: A_{1340}}$	DNA/RNA to CH_2 ratio for nuclear to cytoplasmic ratio, which is known to change during disease progression
$\mathbf{A_{1032}: H_{1080}}$	DNA, RNA and glycosylation profiles for epithelial segregation and differentiating between reactive and other stroma.
$\mathbf{A_{1080}: A_{1238}}$	Relative concentration of nucleic acids to collagen and glycogen glycosylation
$\mathbf{H_{2873}: H_{2956}}$ & $\mathbf{A_{2916}: H_{2848}}$	Relative CH_2 to CH_3 concentration important for stroma model to separate between the different types of stroma
$\mathbf{A_{1032}: A_{3080}}$	Relative concentration of DNA/RNA to proteins

Table 6.3. Detailed description of the important features in the different classification models obtained using the FT-IR data. Abbreviations: H: Peak Height; A: Peak Area at the indicated the wavenumber. For instance, the H_{1545}: H_{1653} indicates the peak height ratio of 1545 cm^{-1} and 1653 cm^{-1} wavenumbers.

6.5 Results

6.5.1 High performance IR microscopy – a new confocal, spectral-spatial scanning system.

To address the need for a low noise, speckle insensitive and diffraction-limited microscope, we developed a design precisely to address these shortcomings and enable translational studies. Our microscope, shown in **Figure 6.1A**, consists of a multi-laser unit spanning the mid-IR fingerprint region from 770-1940 cm^{-1}, interchangeable high numerical

aperture (NA) optics with 0.56 NA and 0.85 NA image formation lenses, a cryogenically cooled, single element Mercury Cadmium Telluride (MCT) detector, and a high-speed linear motor microscopy stage. Each aspect of this design is optimized to overcome current drawbacks. First, we utilize the high brightness of the laser to provide confocal illumination using high NA lenses and use apertures to limit the focal area. The confocal geometry not only provides spatial localization but is also effective in rejecting out of focus light as well as reduced speckle due to limited sample area illumination. Second, the use of a cooled single element detector provides high SNR data due its superior noise characteristics compared to array detectors as well as the ability to lock into the modulated QCL pulsed signal. Third, real-time controls are integrated into the system to maintain high fidelity. Since the confocal geometry is effective in rejecting out of focus light, slight tilts in the sample can drastically affect the image's focus while the high-speed stage is scanning the sample over large areas. We developed and integrated software controls that make axial adjustments to keep the sample in focus in real-time, which also compensates for chromatic aberration and provides optimal SNR at every point. In addition to optimizing imaging performance, we also optimized spectral fidelity by resetting laser parameters at every wavenumber to the optimal repetition rates, pulse widths, and pointing alignment. The instrument can scan at up to 300 mm/s; for each pixel during the scan, axes encoders trigger detection electronics locked into the laser's pulse frequency, allowing images to be acquired at a magnification limited only by the encoder resolution. The pixel size is optimally set at 1 μm, no larger than half the size of the point spread function (PSF) at the shortest tunable wavelength according to the Nyquist sampling criterion. The scanning is optimized for a "long direction" that limits acceleration-deceleration effects and achieve high pixel rates. Finally, the raw data undergoes a multistep post-process to obtain absorbance data from a background, integrate by aligning forward and backward stage sweeps using a non-rigid alignment algorithm that compensate for stage induced aberrations, and inter-band alignment to account for instrument drift over time. If needed, the data can be deconvolved[123] against a simulated PSF at each wavenumber to further improve visualization.

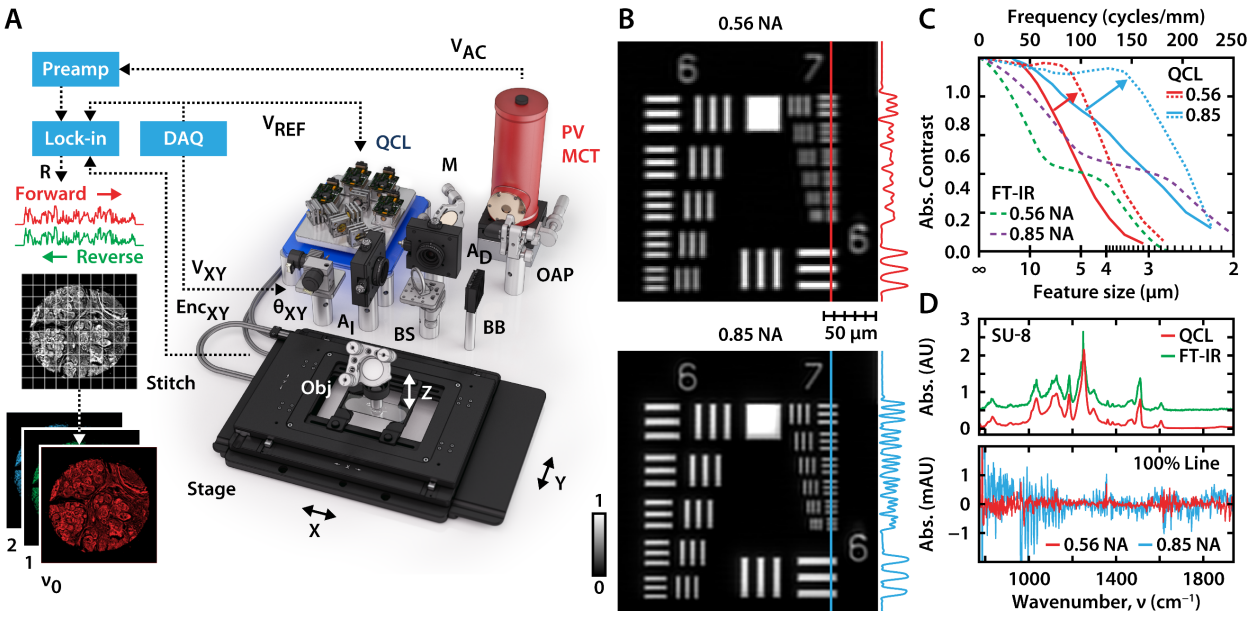

Figure 6.1. Laser-based confocal infrared microscopy. (A) The microscope consists of a quantum cascade laser (QCL) source, tunable for narrow-band emission across the mid-IR fingerprint region. A high-speed stage and focus unit raster scans the sample, while the detection is locked into the laser's pulse rate and each pixel is triggered by the stage encoder counter. (B) Images of USAF 1951 resolution test targets show diffraction limited performance for absorbance at 1658 cm^{-1} with both the 0.56 NA objective (top) at 2 µm pixel size and the 0.85 NA objective (bottom) at 1 µm pixel size. (C) The optical contrast of each set of bars is plotted as a function of spatial frequency. The bars are no longer resolvable if the contrast drops below 26%, which corresponds to the Rayleigh criterion separation distance. The arrow indicates the deconvolution of the raw data (solid line) with the simulated PSF at the specified wavenumber to achieve a substantial resolution enhancement (dotted line). These results are compared to the simulated performance (dashed line) of a FT-IR instrument with optimized Schwarzschild objectives used in FT-IR imaging. (D) The unprocessed spectrum of a 5 µm layer of SU-8 epoxy acquired by our QCL instrument at 1 cm^{-1} resolution shows accurate spectral features compared to a reference FT-IR spectrometer. The 100% spectral profile lines show absorbance noise of ~10^{-4} and 10^{-3} for the two objectives over most the fingerprint region.

6.5.2 Evaluation of imaging performance

We sought to ensure spectral and spatial fidelity of the newly designed instrument. We first validated the spatial resolution against a USAF 1951 chrome-on-glass resolution target. The Rayleigh criterion is often used to determine the resolution of the instrument, and signifies the minimum separation distance between two objects where they appear to remain distinct, corresponding to a contrast ratio of at least 26.4%. Accordingly, our system provides diffraction-limited resolution of 4 µm and 3 µm with the 0.56 NA and 0.85 NA objectives, as shown in

Figure 6.1B and seen in the absorbance contrast as a function of line spacing in **Figure 6.1C**. After deconvolution, minor improvements in resolvability to 3 μm and 2 μm respectively are seen but a drastic improvement in the contrast of structures up to 10 μm is observed, highlighting the potential to improve visualization. To our knowledge, the only comparable capability to this performance has previously been reported using synchrotrons.[25] We further compared the experimental transfer functions with that of FT-IR instruments using optimized Schwarzschild objectives of the same NA using Code V optical design software. The underlying mechanism of image formation is apparent for a coherent source whose amplitude transfer function (ATF) has a flat frequency response followed by a sharp cutoff dependent on the aperture size of the pupil. As the beam coherence decreases, the transfer function will approach optical transfer function (OTF) behavior as seen with our measurements. Since the OTF of an instrument with an incoherent source is the autocorrelation of the ATF, the contrast gradually declines to zero at twice the ATF's cutoff frequency. However, the higher cutoff frequency of these simulated incoherent systems falls below the Rayleigh criterion threshold where the features are indistinguishable. In FT-IR imaging instruments, the lower spatial frequencies are attenuated because the Schwarzschild objectives have an obscuration created by the secondary reflector and this presents in the simulations as an additional loss in contrast. Above the Rayleigh resolution, our confocal microscope outperforms and has substantially higher contrast levels compared to the current state of the art infrared imaging instruments. The spectral fidelity of the instrument was tested by measuring an epoxy photoresist, at 1 cm^{-1} resolution from 770-1940 cm^{-1}. The measurement accurately tracks the reference spectrum acquired with a FT-IR spectrometer, as indicated in the spectra in **Figure 6.1D**. To provide the most representative noise characteristics, the spectra and signal to noise ratio (SNR) calculations are from data without deconvolution. Deconvolution provides substantial smoothing of the background as well as feature sharpening. Without post-processing, we achieve noise levels on the order of 10^{-4} and 10^{-3} at 0.56 and 0.85 NA respectively. This data quality is not feasible in an FT-IR imaging system and has not been previously reported for an IR microscope.

6.5.3 High resolution and rapid IR imaging for breast tissue segmentation

We imaged breast tissue previously analyzed by FT-IR imaging using the confocal microscope. Representative images and spectral data are shown in **Figure 6.2A** and **Figure**

6.2V, respectively. In **Figure 6.2A**, both the 0.56 and 0.85 NA objectives provide good quality data that matches well with the conventional H&E images; the 0.85 NA images are sharper, as expected. Representative spectra from histologic units in breast tissue (**Figure 6.2B**) match those acquired from FT-IR imaging and show the subtle spectral differences that permit accurate classification. We selected 12 discrete frequencies from the FT-IR 6E and 6S models (**Figure 6.2C**) and also show differences in major classes as well as an average SNR of ~1000 for a single scan (**Figure 6.2D**). This SNR enables high accuracy tissue classification with fewer frequencies that is only achieved in FT-IR imaging systems by extensive signal averaging and using mathematical noise rejection that needs hundreds of frequencies to estimate noise characteristics. To quantify the comparison between the FT-IR and confocal laser microscopes, scanning a full TMA shown here with a typical commercial FT-IR imaging system would require: nearly 25,000 individual frames of the 128x128 array detector to cover the area and averaging each frame 32 times each (1.8 min of total acquisition) in a total acquisition time of ~ 40 days. Due to the weak radiance from a FT-IR globar source, a large number of co-additions are required in order to achieve the required SNR for accurate tissue classification. To further increase the SNR, an additional processing time (30 s per frame) is needed using the most effective noise rejection algorithms available today[126] which adds another ~10 days. The high SNR of our system allows us to avoid signal averaging and dispenses entirely with the need for numerical noise rejection. Thus, the microscope reported here permits imaging and analysis of the full TMA in feasible time (8 hr), cutting the time to validate imaging results from months to one day and greatly accelerating the potential of IR imaging for biological research. This approximately 50-fold reduction in time to acquire the needed quality data with the required set for obtaining a decision-ready image presents a practical comparison between conventional approaches and this new instrument.

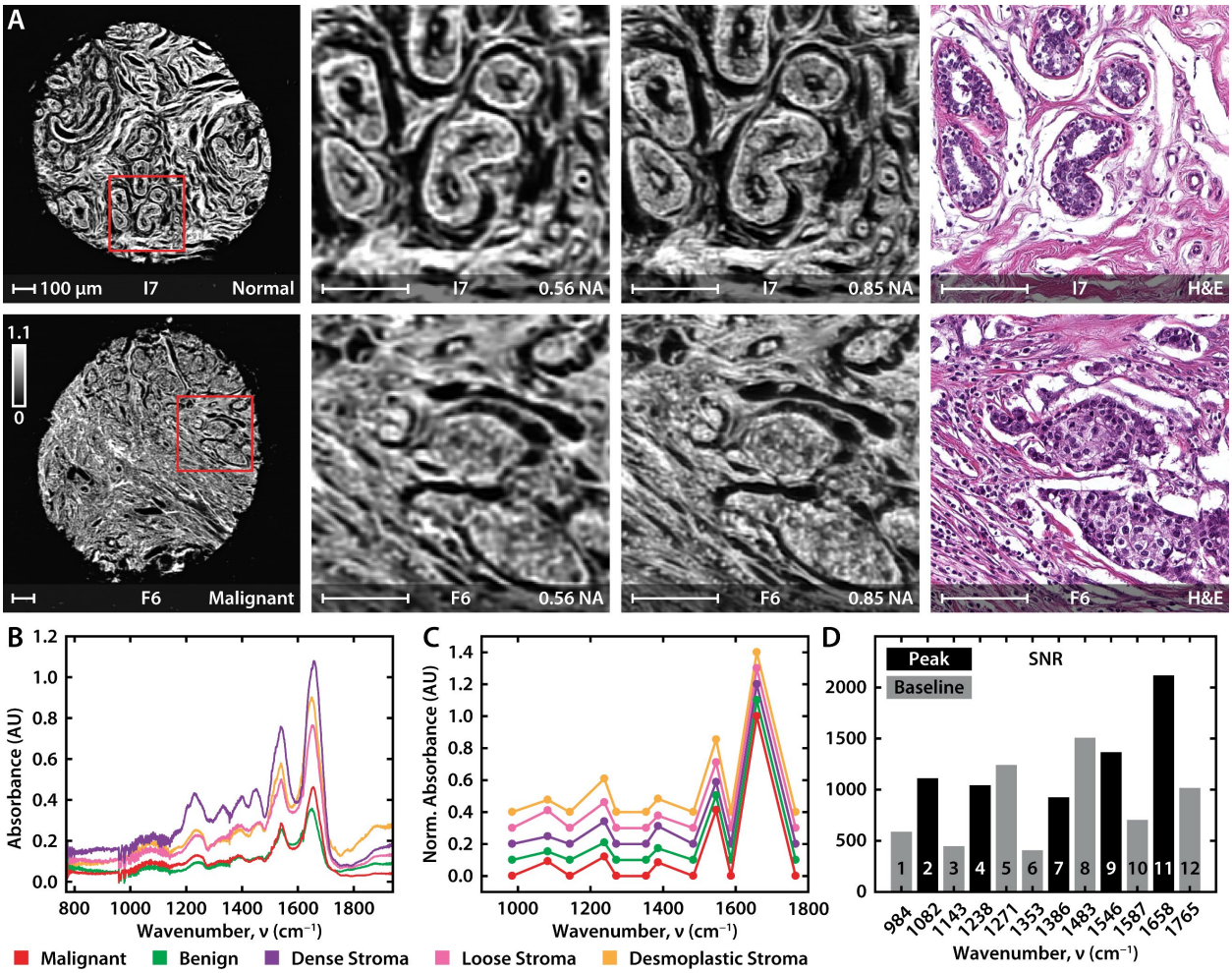

Figure 6.2. High-definition imaging of breast tissue. (A) A selection of one normal and one malignant tissue sample from a 20 x 20 mm TMA, acquired at 0.56 NA and 0.85 NA at 2 µm and 1 µm per pixel, respectively. The absorbance at 1658 cm^{-1}, indicative of the Amide I vibrational mode, is shown in the image and enlarged subsections that are compared to an H&E stained image of a serial section. (B) Point spectra from five tissue types at 1 cm^{-1} resolution; spectra are offset for clarity. (C) Normalized and baselined point spectra from five tissue types at discrete frequencies. (D) Average SNR for important spectral features.

6.5.4 Compatibility of DFIR results with FT-IR developed classification algorithms[124]

The precision of the information provided in a spectral data set is limited by the worst performing spectral band. While the presentation of single band images may appear excellent, the utility of the data set is unknown until we pass it through machine learning algorithms, which because of their design to identify patterns, tend to especially highlight any defects present the

imaging system. Here we have tested the DFIR system against two classification algorithms initially developed on FT-IR data where further details can be found[124].

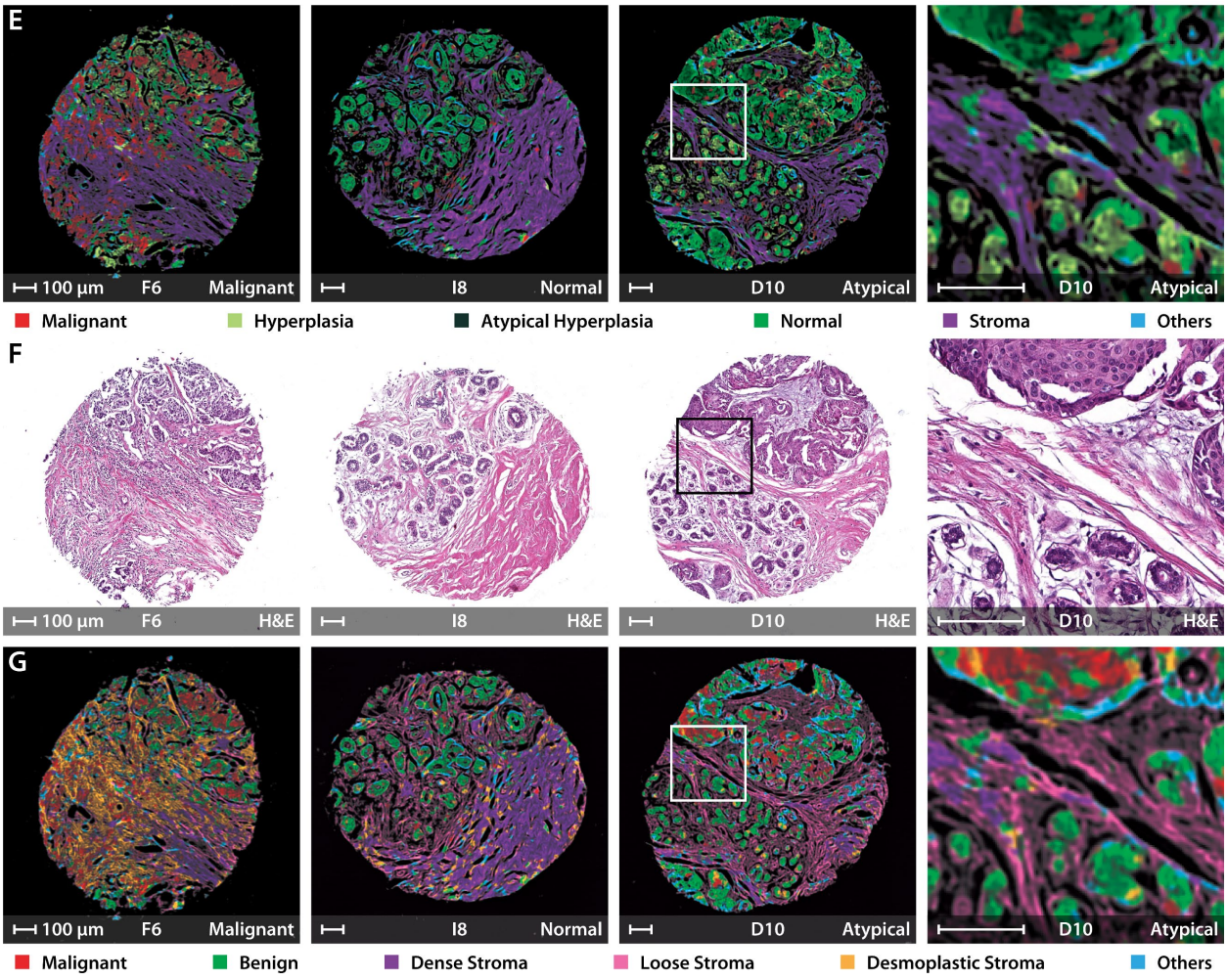

Figure 6.3. Performance of two DF epithelial and stromal classification models (top and bottom rows) originally developed for FT-IR analysis[124]. A small region from the hyperplasia with atypia sample is also shown, along with its H&E stain, to demonstrate the spatial distribution of normal and malignant cells. The letter and numbers below each image correspond to the row and column of the TMA (A1 is the Top Left sample), respectively. All scale bars: 100 µm.

We emphasize that low SNR does not permit accurate classification, as previously reported.[31] The apparent SNR for DF systems reported previously has ranged from ~10 in early systems[64] to ~100 using expensive cooled detectors in the latest state of the art.[88] While large format array detectors offer rapid imaging, the typical SNR cannot approach the levels reported here using a single element detector. Even if laser stability or innovative designs allowed signal

averaging to improve the SNR, the additional measurements will result needing the same time as an FT-IR imaging experiment, providing no specific advantage to DFIR systems. A less discussed, but known issue, with using lasers is that coherence induced speckle acts as a noise source since the underlying tissue structure changes from sample to sample. Speckle contributions may not appreciably manifest in images but do affect spectra. The variance introduced by speckle remains to be quantified using theory[55] but current estimates are of a few percent, which will not allow accurate histologic recognition. Thus, while it is possible to translate the FT-IR imaging results to DF instruments in principle, there are no reports yet of histopathological models with the complexity presented here being possible with speckle-free laser-based instruments using these few frequencies.

6.5.5 Clinical translation to biopsy and surgical specimens

The impact of the three developments thus far – accurate HD histology, high performance IR imaging, and fast histologic recognition – lies in a translation of the approach to typical samples in screening or operative care. We believe a primary utility of this technology will lie in rapidly triaging biopsies. **Figure 6.4** shows fast and accurate detection of tumor and characterization of the tumor microenvironment in needle biopsy sections. There are numerous implications of a clinically feasible (in both time and accuracy) imaging technology. With the microscope shown here, for example, biopsy results can now be provided on the day of biopsy itself, reducing wait times for patients. Combined with stainless staining techniques,[85] both conventional and new information can be provided to aid precise and accurate diagnoses. In atypical cases, additionally, both epithelial and stromal measurements[94] can be used to help pathologists make more confident decisions. This slide of biopsies shown in **Figure 6.4** can be imaged and classified in 3 hours using the same 6 class technique discussed previously. We clearly see the spatial accuracy of the model wherein the cancerous regions are being classified with a majority of malignant epithelium surrounded by reactive collagen acting as further confirmation. Needle biopsies are the standard for breast cancer diagnosis and for many other solid tumors. Approximately 1.6 million biopsy samples are taken annually in the US for breast cancer alone,[127] with typical needle sizes of 14-22 gauge[128] (2 mm to 0.7 mm diameter biopsy). There is an emphasis on returning biopsy results within days both to confirm the diagnosis in

patients with breast cancer and to rapidly inform the large majority of biopsied women who do not have cancer.

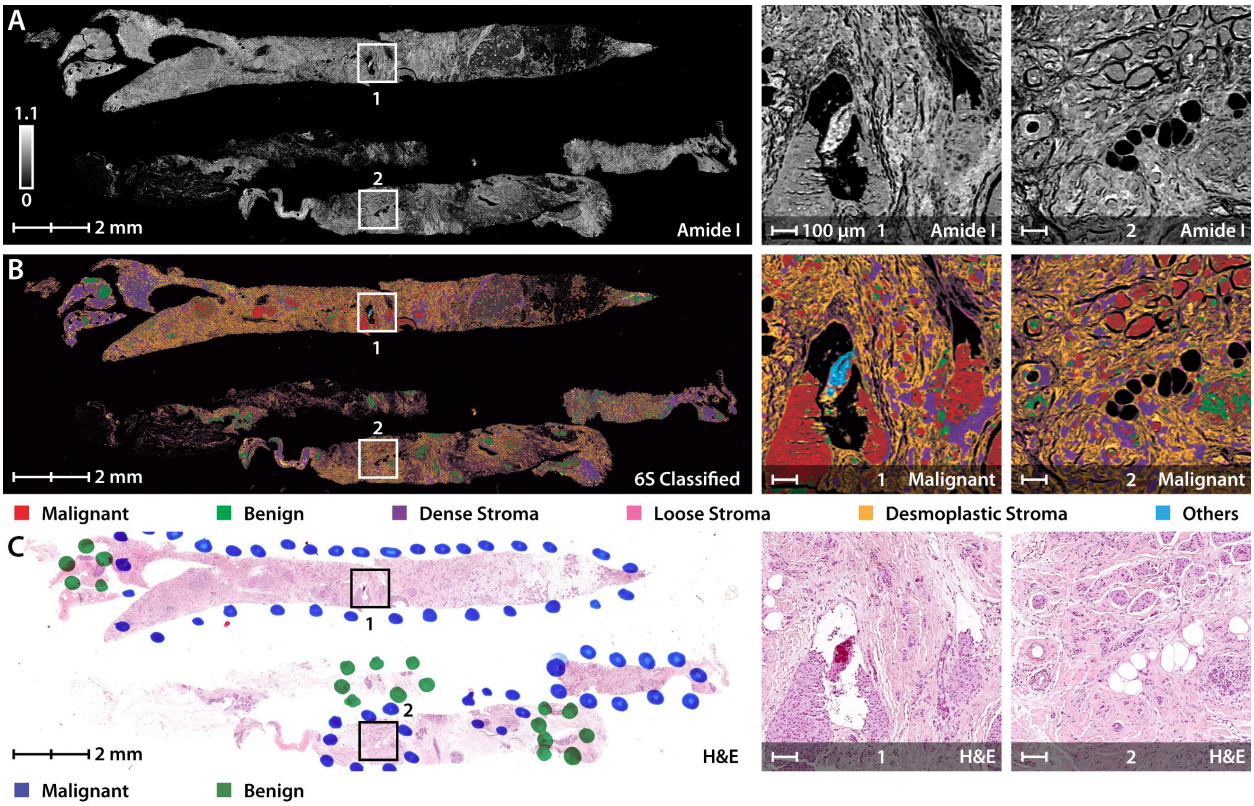

Figure 6.4. Rapid triaging of malignant sections using stainless imaging of human breast biopsy samples in feasible times. (A) Image of needle biopsy sections using absorbance at 1658 cm^{-1} with specific malignant regions enlarged for clarity. (B) The multispectral image was classified using a six class model separating cancerous and normal epithelial cells from various collagen-rich stromal types (6S). (C) Pathologist annotations to the H&E stained image of a consecutive section demonstrate agreement with the IR classified image.

6.6 Discussions and Conclusions

Here we demonstrate histologic recognition by high resolution imaging at a competitive level of morphological detail as current microscopy albeit with new information regarding disease state and its progression; instrumentation for high performance IR DF microscopy further enabling useful histologic imaging in clinically-feasible times. This is critical for practical IR imaging towards digital pathology. Given that we use chemistry in detection of disease, as opposed to morphology in conventional pathology, the sensitivity of IR imaging opens the possibility of additional disease analysis. Higher resolutions offer increased analytical sensitivity

where comprehensive computational models, including those more complicated than presented here can be used to then relate back to conventional spatial images. While the smaller pixels do indeed provide greater chemical localization, the subcellular sensitivity also implies that the heterogeneity in cellular responses may prevent accurate classification.

While many optical scanning confocal designs are available for visible microscopy and several microscopy approaches available in the infrared, enabling the use of a broadly tunable IR laser is not trivial. The large wavelength range in the mid-IR results in strong chromatic aberrations and makes design difficult using refractive optics; the use of reflective optics result in loss of light and weighting of collected signal on scattering due to the central obscuration in schwarzschild objectives. Here, our optical design is combined with real-time control algorithms to reduce errors and achieve minimal-distortion images, demonstrating a performance that has not been previously seen for IR microscopy. While widefield configurations can typically provide greater speeds due to their multichannel advantage and increasingly larger sensor formats, area illumination using a laser typically suffers from a low SNR due to miniaturized detectors and presents speckle patterns across the image that can complicate spatial interpretation needed in pathology. The low noise in our single element detector, ability to modulate the beam and confocal geometry greatly reduce noise within each spectral band, allowing accurate classification models to be constructed from fewer number of discrete frequencies and without the need for extensive signal averaging or mathematical noise rejection. By providing enhanced spatial image quality, as shown by rigorous contrast analysis, the classified images allow for detailed tissue segmentation for tumor detection. The path to clinical translation is also enabled by the demonstration of HD histology and new instrument developed here. The key idea is that only a small number of spectral frequencies provide accurate and robust classification that allows us to overcome the slow data acquisition. The implementation of the presented approach on large biopsy sections emphasizes the potential of efficient clinical translation. Precise detection of the epithelial and stromal signatures in a few hours of tissue procurement can greatly complement and extend the capabilities of the current clinical practices. The combined instrument and epithelial-stromal segmentation opens new possibilities for developing early detection automated algorithms, serve as a confirmation tool for diagnosis, especially facilitating the pathologists to focus on specific regions of interest. While focused on breast cancer, this work also paves the way for development of similar practical scanning for other tissues and disease types.

CHAPTER 7: VERSION 2.2 – MULTICOLOR IMAGING [††]

7.1 Abstract

Advancement of discrete frequency infrared (DFIR) spectroscopic microscopes in image quality and data throughput are critical to their use for analytical measurements. Here, we report the development and characterization of a point scanning instrument with minimal aberrations and capable of diffraction-limited performance across all finger- print region wavelengths over arbitrarily large samples. The performance of this system is compared to commercial state of the art Fourier transform infrared (FT-IR) imaging systems. We show that for large samples or smaller set of discrete frequencies, point scanning far exceeds (∼10−100 fold) comparable data acquired with FT-IR instruments. Further we show improvements in image quality using refractive lenses that show significantly improved contrast across the spatial frequency bandwidth. Finally, we introduce the ability to image two tunable frequencies simultaneously using a single detector by means of demodulation to further speed up data acquisition and reduce the impact of scattering. Together, the advancements provide significantly better spectral quality and spatial fidelity than current state of the art imaging systems while promising to make spectral scanning even faster.

7.2 Introduction

Infrared (IR) spectroscopic imaging has undergone several innovations in recent years that have advanced it as an analytical technique.[52,129,130] This is a nondestructive approach that directly images the distribution of chemical composition of samples in the absence of exogenous contrast agents. Instead, contrast is derived directly from molecular structures which absorb optical frequencies that are resonant with the vibrational modes of the comprised functional groups.[16,17] Each peak in the absorption spectrum corresponds to a characteristic which together can be used for the identification and classification of spatially and spectrally complex samples. While IR vibrational frequencies span the mid-IR spectral range (800−4000 cm^{-1}), the fingerprint region (800−1800 cm^{-1}) has traditionally been critical for biological and polymeric

[††] The work in this chapter has previously been published and is reprinted with permission.

Yeh, K.; Lee, D.; Bhargava, R. Multicolor Discrete Frequency Infrared Spectroscopic Imaging. *Anal. Chem.* **2019**, *91* (3), 2177–2185.

sample identifications,[53,69] The acquisition of a limited spectral range is often a feasible route to reduce data acquisition time while maintaining the analytical capabilities of IR spectroscopy and imaging. Recent studies have shown that the ability to obtain actionable information about a sample does not require the measurement of the continuous spectral range[68,131] a restriction fundamental to Fourier transform (FT) technology, the historical state-of-the- art. For example, a discrete subset of spectral positions, typically less than 30 bands, is often sufficient for histopathological tissue imaging. This idea has led to the development of discrete frequency infrared microscopy (DFIR) systems, predominantly using quantum cascade lasers (QCL) where 50-fold gains in speed have been reported by only measuring the spectral frequencies required. Furthermore, with substantially higher source power and a narrower spectral range of lasers, refractive optics can be used for better image formation. This study focuses on design of instruments under these conditions and how laser- based DFIR imaging may be enhanced even further in performance.

Imaging instruments were first designed in widefield configuration with fixed frequency sources10 followed by broadly tunable systems[64,79,88,119,132] as lasers became more prevalent. IR light from a QCL is condensed onto the sample and the residual signal after attenuation is imaged using an uncooled bolometer camera or cooled mercury−cadmium−telluride (MCT) focal plane array. In this configuration, the narrow spectral bandwidth of the coherent laser, multiple reflections within the optical train, stray light and scattering from the sample result in speckle that degrades image quality. Since the analytical quantity of interest is absorbance, a ratio of the recorded signal from a sample to a reference signal is measured. The ratio is a measure of total beam attenuation, which includes contributions from both absorption and scattering.[133,134] Since scattering is wavenumber and morphology dependent, errors arise in correct estimation of absorbance. In FT-IR imaging, the scattering contribution is largely subtracted from recorded attenuation by using a nearby non-absorbing region to estimate the slowly varying scattering. Other correction methods also work well, primarily because the incoherence of the thermal source does not result in additions of the scattered electric fields but of intensities. For a coherent source, scattered field additions manifest in the formation of speckle patterns and cannot simply be subtracted out due to redistribution of light in the spatial plane. Measuring the sample again at identical location but with a non-absorbing frequency tens or hundreds of wavenumbers away alleviates the nonuniformity of laser illumination but is not

effective in alleviating speckle patterns. Hence, several additional techniques have been proposed to mitigate speckle effects. Rotating diffusers rapidly vary the speckle pattern while integrating the signal over time,[64,119,135] spectral averaging integrates the fluctuating speckle patterns as the laser tuner sweeps,[88] and time delay integration averages speckle patterns by shifting the sample.[136] Regardless of their individual efficacy for specific samples, none of these methods provide a general solution to scattering induced effects. They also increase experimental times, which reduce the multichannel detection advantage of widefield imaging.

In contrast, exceptional image quality has been reported with scanning systems that map the sample point by point.[120,124,137] These scanning systems typically have higher imaging quality simply due to the ability to condense light with substantially higher intensities per illuminated area but are also immune to many of the drawbacks observed for widefield systems. First, only a single point is illuminated and detected at a time; hence, recorded intensity is affected by coherent addition of scattered light only from a very small (single pixel) area. Without the need to average laser speckle over time, spectra or space, absorbance at single locations can be recorded in much shorter time. Second, high laser powers are not required, as covering large areas and a flat-field illumination is no longer required. With these advantages, the image quality and signal-to-noise ratio (SNR) of these systems facilitates the development of analytical capabilities not previously possible with DFIR systems. Finally, point illumination enables the development of instruments that measures both transmitted light and novel means to measure absorption, for example, through photoexpansion of the sample using devices such as nanoscale cantilevers[138] with corrections,[139–141] acoustic transducers,[142] and visible light probes.[143,144]

A major drawback of point scanning systems, however, is a loss of speed in acquiring images compared to widefield systems. Since each point must be measured individually, the advantages of higher fidelity data must sufficiently offset the inefficiency of scanning. There are several designs of point scanning systems that build up the image by raster scanning a point across the sample as fast as possible. In the visible spectrum, laser scanning confocal microscopes commonly incorporate mirror galvanometers and resonant scanners. However, the optical design of these involves scan lenses, tube lenses, and infinity-corrected objectives each containing many refractive elements. This is difficult in the mid-infrared spectrum as chromatic and field corrections are more complicated and expensive when recording a spectral range 20-fold larger while being restricted to a very limited selection of IR compatible materials with

viable dispersion characteristics. Thus, far, IR scanning systems have relied on on-axis scanning by either sweeping the lens[145] or sweeping the sample.[124] Here, we describe a point scanning system that operates by sweeping the sample. After optimizing the system, we further demonstrate a new technique that can increase data acquisition rates using simultaneous illumination at dual frequencies. This "multi-color" scanning approach is then described and evaluated.

7.3 Design and Optimization

The designed system is shown in **Figure 7.1A** and is based on earlier versions reported in previous studies.[124,137] It is powered by an array of QCL modules that together have a tuning range that spans the mid-IR fingerprint region (Block Engineering). Dual apertures (**A_I** and **A_{DET}**) equidistant from the sample on the illumination and detection paths are aligned such that they have identical focal points in the sample plane. Half the beam is split (**BS**) to the sample and focused onto the sample and detector using a refractive lens (**OBJ**) and a reflective off-axis parabolic mirror (**OAP**) respectively. The remaining half is dumped into a beam block (**BB**). The design of the microscope allows for epi-illumination of the sample with an interchangeable selection of 3 objectives with numeric apertures (NA) of 0.56, 0.71, and 0.85 (LightPath Technologies), which spans the range of NAs reported in most previous IR imaging studies. The transflected signal is detected by a cryogenic photovoltaic mercury cadmium telluride (**PV MCT**) detector (MCT-13-0.5PV, InfraRed Associates) without preamplification or biasing, and demodulated using a lock-in amplifier (MFLI, Zurich Instruments) referenced to the QCL's pulse repetition frequency. The magnitude (**R**) of the signal's in-phase and quadrature components is used to form the image as the stage scans the sample. A standard white-light epi-illuminated inverted micro- scope (not illustrated) is built underneath the microscopy stage and used for targeting selecting the area for IR scanning as well as additional features later described.

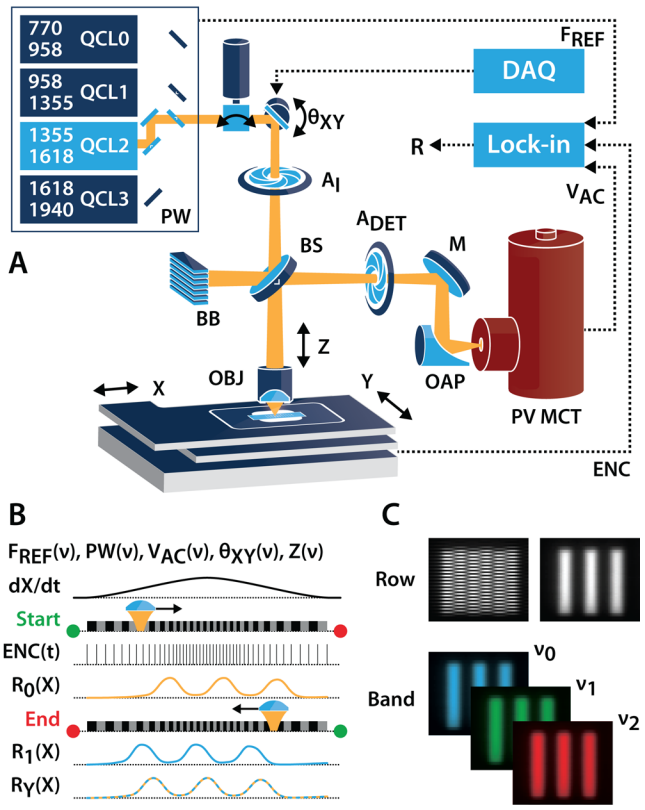

Figure 7.1. Schematic of a QCL-based point scanning microscope depicting the (A) optical and electronic components, (B) signals diagram, and (C) software post-processing.

We have designed several subroutines that carefully increase the fidelity of the acquired signal but operate in the background as diagrammed by **Figure 7.1B**. First, the power stability of each wavenumber is a function of the laser's repetition rate (**F_{REF}**) and pulse width (**PW**). This is not consistent even within the tuning range of each of the four lasers. Before scanning an image, these parameters are either (in priority) overridden by the user, directly selected from a precalibrated table of optimal settings, automatically estimated using the nearest entry in the table, or restored to default which will result in a loss of SNR of undetermined magnitude. The laser's intensity (**V_{AC}**) and pointing angle (**θ_{XY}**) are also unique so we adjust the sensitivity of the lock-in amplifier and galvanometer angle corrections, respectively. Chromatic dispersion tables, simulated with Code V (Synopsys), are used to estimate the jump in focal position (**Z**) before running a quick short-range autofocus subroutine. The magnification of mapping systems is arbitrarily adjustable allowing us to optimize each image by wavenumber (ν). The pixel size ($\Delta X \leq d_{XY}/2$) is adjusted proportional to the lateral point spread function ($d_{XY} \cong 1.22/\nu NA$). To prevent aliasing due to excessively low sampling rate and to minimize noise in the signal, the

lock-in time constant ($\tau = C^{-1}t_{\Delta X}$) is set relative to the minimum pixel dwell time ($t_{\Delta X}$) where C is a parameter specific to the lock-in amplifier that has a low-pass filter order that reaches steady state in $C\tau$.

The axial tolerance of the scanner's ability to trace the sample substrate is coupled to the axial point spread function ($d_Z \cong 2d_{XY}$). Any deviations as the sample moves out of focus will result primarily in a loss of power. Vibrations manifest as image striping, while a slanted sample causes vignetting. This becomes problematic since absorbance measurements are referenced to the original laser power, often taken at a single point with ~100% reflectance on the background. Clearly, a single background measurement is not enough when the power varies by position. We implement two methods to address this problem. The first performs a ~9-point autofocus across the sample and calculates a best-fit plane. Manual sample leveling improves results, minimizing the required travel range of the z- axis, but even a carefully adjusted sample is still not flat. The scanner corrects for residual misalignment by tracing the sample in 3 dimensions, keeping parallel with the substrate regardless to how it is mounted. Second, following the mechanical corrections, we reference to an interpolated background plane instead of a single background value.

Once these initialization procedures are completed, the instrument is designed to scan the sample line by line. For discussion purposes, we assume the instrument scans row by row, but technically, it is not required that we scan horizontally or vertically. Since the stage coordinates are adjusted to align to the sample plane, any affine transformation matrix is possible, including rotations that scan diagonally. Scan areas do not need to be rectangles either. This framework can improve efficiency by fitting the scan pattern to the arbitrary sample, thereby minimizing the amount of empty space that is wastefully mapped point by point. This feature is also an advantage over widefield imaging and, for sparse samples like those in cytology, may render point scanning a better option. When scanning each row, the acquisition is triggered based on distance traveled, as shown in **Figure 7.1B**. Instead of scanning and acquiring data at a fixed rate, this encoding minimizes errors because of acceleration, deceleration, or other velocity instabilities. A consequence is that pixel dwell time is not uniform across the scan direction; pixel dwell time is shortest when the stage is at maximum velocity near the center of the sample. Noise remains consistent throughout since the lock-in amplifier's time constant is dependent on

the shortest pixel dwell time. The steady stage value of each pixel should be measured $C\tau$ after each trigger and error in the delay creates an offset between the forward and backward scans.

Image alignment procedures to first align the rows, and then to align the frequency bands is necessary, as show in **Figure 7.1C**. Row alignment is GPU accelerated and performed in MATLAB where the odd and even lines are nonrigidly registered only in the x-direction to correct for residual local distortions. To reduce memory requirements, we may bin the data prior to registration and correspondingly scale the calculated displacement fields afterward. Once each band is constructed, we must also align the bands with each other to account for sample drift. This is tracked using the IR images or more accurately by using the white light images from the inverted brightfield microscope if imaging on a transparent substrate. The displacement is calculated by detecting corners using the features from accelerated segment test (FAST) algorithm, using the fast retina keypoint (FREAK) algorithm to match the keypoints between successive images, and finally estimating the geometric transform. Inaccurate band alignment results in corrupted spectra. A point spectrum extracted from a multispectral cube acquired from a system that measures spatial before spectral information must be averaged within a window of surrounding pixels representing the area of uncertainty due to sample drift. In the opposing case, for instance all FT-IR instruments and some QCL DFIR instruments, which acquire all spectral information at a given location before moving the sample, the averaging is unnecessary. Errors due to sample drift appear as misaligned image tiles and this type of error is less impactful for most chemical imaging applications.

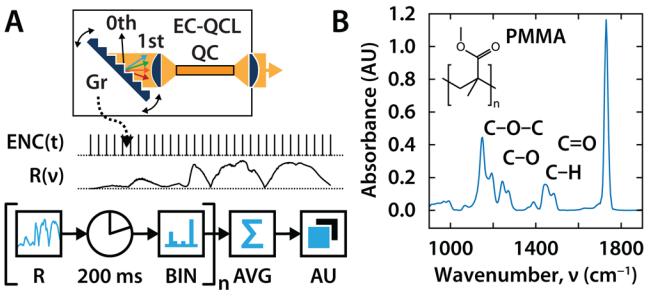

Figure 7.2. Schematic of a QCL-based rapid scanning point spectrometer depicting the (A) control scheme and (B) a standardized diagnostic spectrum.

One of the disadvantages of discrete frequency systems is the necessity of prior knowledge of the sample to optimally select useful spectral features for imaging. To acquire full

spectra when needed, a flexibility in design is built-in to our system by enabling use as a rapid scanning point spectrometer. This capability is analogous to the ability of FT-IR imaging systems to provide a single spectrum. Along with a standard white-light epi-illuminated inverted microscope (not illustrated) built underneath the microscopy stage in **Figure 7.1A** for targeting the spectrometer, we rapidly collected representative spectra of key locations on the sample. The control scheme of the spectrometer shown in **Figure 7.2A** is essentially identical to an FT-IR spectrometer where spectral information is computationally derived from the physical position of a moving reference mirror encoded with a copropagating reference laser. In QCL spectrometer design, the spectral tuning of an external cavity (**EC**) QCL is relative to the rotation of a grating (**Gr**) that directs a specific frequency into the quantum cascade (**QC**) gain medium where the wavenumber is tracked by a TTL signal at every 0.5 cm^{-1}. Spectral resolution and SNR do not depend on acquisition time as they do for an FT-IR spectrometer.[3] The raw data acquired here is 0.5 cm^{-1} spaced, but the data is typically binned to 4 cm^{-1} for better SNR. The small piezoelectric-driven grating can be oscillated quickly. We acquire fingerprint spectra at 4 cm^{-1} resolution every 200 ms and coaverage 10 iterations to obtain the diagnostic PMMA thin film spectrum shown in **Figure 7.2B** at 0.5 Hz. These specifications are adjustable according to the experiment and viable spectra can be acquired at up to 10 Hz.

7.4 Methods

All FT-IR reference images and spectra are acquired using a Cary 620-IR imaging microscope with a 680-IR FT-IR spectrometer (Agilent Technologies). This microscope is equipped with a liquid nitrogen cooled 128 × 128 pixel focal plane array (FPA) detector and a 0.62 NA reflective Schwarzschild objective with 36X total magnification resulting in pixel sizes of 1.1 μm. Images are collected with 16 coadditions at 4 cm^{-1} resolution, processed with a Blackman-Harris apodization function, and then ratioed to a 128 coaddition background. QCL-equipped spectrometer data is acquired as described with each configuration in this study. Average FT-IR point spectra were collected using the 250 μm single element detector in approximately 2 s with 16 coadditions at 4 cm^{-1} resolution with an asymmetric single sided interferogram sampling speed of 75 kHz and a reference laser sampling interval of 2.

Chrome on glass USAF 1951 resolution test targets (II−VI Max Levy) are used for resolution testing since glass has broadband IR absorbance and the thin chrome plating does not

introduce scattering artifacts. PMMA film was spun coat on low- emissivity microscope slides (Kevley Technologies) at 1 μm thickness and used for spectrometer calibration. SU-8 photoresist USAF 1951 resolution test targets were prepared on low-e microscope slides at 5 μm thickness, a common biological sample thickness, and used for to test multicolor imaging.

7.5 Results and Discussion

The key performance metric in design of any instrument is the SNR. The analytical signal (absorbance) is determined by the sample in IR spectroscopy and noise is the metric for comparison. Two sources of noise must be examined in imaging. The first is the variation across the field of view, while the second is the spectral noise at any point. The spatial noise includes a component arising from spectral noise (at every pixel) and variations in the image (arising from illumination, focusing, drift, or other sources). In addition, each system has its unique spatial noise contributions. In point scanning systems, abrupt motion of the microscope stage can vibrate the sample and appear as low frequency directional fluctuations in absorbance. Similarly, sensor nonuniformity of the staring array provides a spatial noise for widefield FT-IR imaging systems. Hence, it is instructive to examine spatial noise first. The noise characteristics of the DFIR scanning system are compared to a leading, commercially available FT-IR imaging spectrometer in **Figure 7.3A**. Noise in each case is calculated as the root-mean-square (RMS) of each band for similar fields of view. As anticipated, the noise across the FT-IR image is devoid of spectral features (other than increased noise due to water vapor lines). The noise in DFIR imaging data is influenced by several factors but mostly dependent on the design of the composite QCL (consisting of four individual modules). We observe variable noise that corresponds to changes in the emission spectrum of each module of the composite source. Noise control for the DFIR microscope is determined by adjusting scan speeds to affect pixel dwell times, while the lock-in time constant and filter orders are set such that their settling time resides within the minimum dwell time of any pixel. Consequently, for each pixel, we ensure that the number of laser pulses recorded is the same, regardless of dwell time at any specific position with respect to the range of stage motion. These controls ensure that the SNR achieved is both maximized and consistent across the image. Optionally, if we decrease the stage velocity, pixel dwell times increase causing the system to select longer filter time constants thereby improving SNR further without needing repeated coaveraged scans.

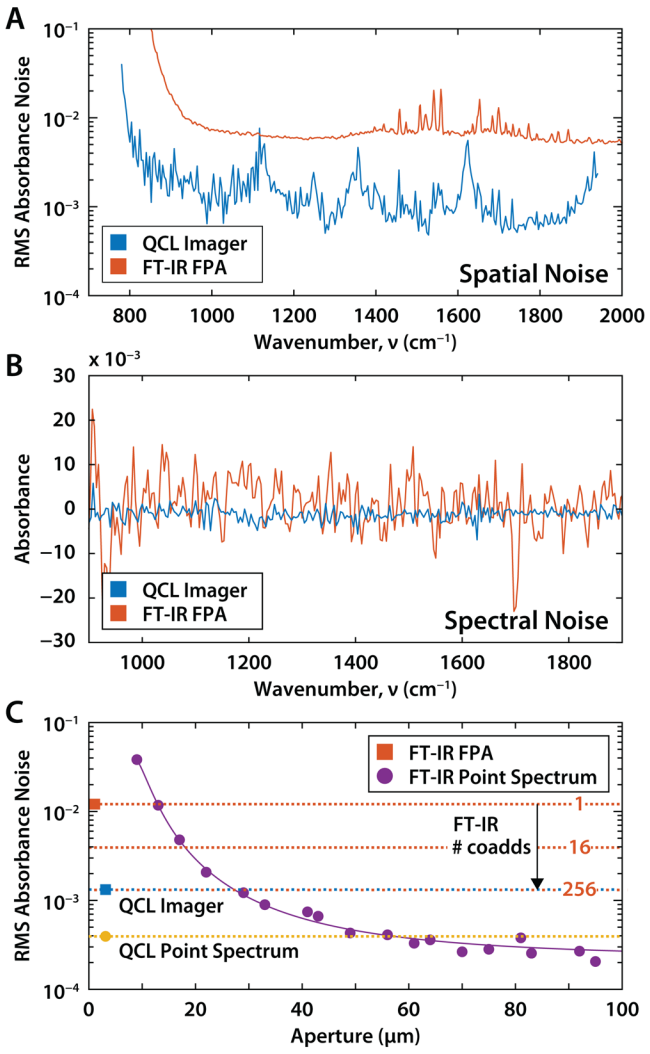

Figure 7.3. (A) Spatial root-mean-square (RMS) noise, calculated using spatial variance of recorded data at each band in a hyperspectral image acquired using the developed DFIR point scanning and commercial widefield FT-IR imaging systems. (B) 100% spectral lines from a single pixel under typical experimental conditions. (C) RMS noise of the 100% line with different aperture settings in a commercial single point FT-IR microscope and its comparison with the point scanning DFIR system.

It is notable that noise in the QCL system here is approximately an order of magnitude lower as the advantage of a low noise sensor and higher source intensity overcomes the multichannel and multiplex advantages of the FT system. Spectral noise reduction algorithms, such as the minimum noise fraction (MNF) method, can reduce the FT-IR RMS noise by less than an order of magnitude,[88] which presents an opportunity to increase data quality using the white noise properties of the FT spectra. However, it should be noted that the noise reduced data

is an estimate arising from a model of noise and the native precision of the data does not increase with mathematical methods. Similarly, the speed of DFIR systems can be increased significantly by only acquiring data needed for particular applications. While the native recorded SNR of the QCL system will be higher, conversely, spectral noise rejection methods are typically unusable for discrete frequency data sets with a small number of recorded bands.

While overall noise in an imaging data set is our primary metric, it is also instructive to estimate the noise and spectral reproducibility of the instrument using single pixel spectra. Here, we compare spectra by examining the 100% spectral lines acquired on a reflective surface, as shown in **Figure 7.3B**. These spectral lines are extracted from the hyperspectral data set acquired with DFIR and FT-IR instruments at typical experimental settings described previously in the methods. The comparisons of spectral and spatial noise show that the DF instrument is capable of lower noise performance, often in much less time. The DF system benefits from real-time coaddition as previously noted, whereas the high performance of the FT-IR spectrometer, despite an orders of magnitude weaker source, attests to the effectiveness of spectral multiplexing of the continuous spectrum (Fellgett's advantage). This advantage has allowed FT-IR spectroscopy to dominate all other forms of spectral acquisition in the mid-IR range for nearly five decades.

While the above comparison is valid for imaging, it is also instructive to examine the performance of the QCL-DFIR spectrometer against the performance of a single point FT-IR spectrometer. We acquire 100% lines using a point detector, similar to that used in our QCL instrument, on the FT-IR imaging system. To compare with the point scanning system, we restrict the microscope's physical aperture to decreasing sizes and calculate the noise levels. **Figure 7.3C** shows the noise in recorded 100% lines as the aperture is closed from 100 μm; in all cases, the data are acquired by signal averaging for 2 s to keep the total measurement time approximately equal to the DFIR spectrometer. As the aperture is reduced to 10 μm, noise rises and eventually light throughput is too low for measurements at diffraction-limited pixel sizes. For larger aperture sizes, noise decreases and stabilizes once the detector area is filled. A comparison of the 100% lines reveals that the performance of the ∼3 μm focal spot of the QCL system is matched by 30−60 μm aperture sizes in the FT-IR system across the spectral bandwidth. For localized measurements, FPA measurements are advantageous[7] as each pixel has effectively a virtual aperture and there is no loss of intensity, though the minimum sampling area is defined by the point spread function (PSF) of the system optics, not the magnification. Each of

these physically smaller (39-fold) individual elements on the FPA have lower readout noise, which is dominant in low light conditions. Additional coadditions (256) can reduce the noise such that the averaged measurement is competitive with QCL noise levels. In the ideal conditions at maximum aperture, the performance of a highly stable FT-IR thermal source illuminating a single element detector is unmatched.

The advantages of QCL systems are only in measurements with resolutions under ~60 μm because a coherent source can be condensed to a much smaller focal point with enough power remaining to effectively illuminate a detector. The minimum focal spot achievable with an incoherent thermal source depends on the magnification of the system and the size of the source, which is comparatively large. Further windowing is necessary to restrict the measurement area which also restricts the available light and consequently degrades the SNR. Thus, on both spectral and spatial measures, we can conclude that the performance of an FT-IR imaging system for a full spectrum at a given pixel has been exceeded when small areas (smaller than 50 μm × 50 μm) are measured per pixel. This is essentially the microscopy regime and the improved performance of QCL-based microscopes represents is now better than comparable FT-IR imaging. This is a major milestone in IR spectral analyses, wherein an appropriately utilized, high laser power has overcome the dominant multiplex and multichannel advantages of FT-IR imaging. While the spectral range of QCLs cannot yet cover the full range of FT-IR instruments, laser innovations are continuing to bridge the gap.

It is also interesting to compare the imaging rates between scanning systems that record data while in motion versus array- based microscopes that record multipixel fields of view (FOV) which are stitched together as a mosaic. The imaging time ofan FPA equipped system (Eq. 7.1) to measure a specific area at a defined data quality (SNR) is linearly dependent on the total pixels in the image ($n_X \times n_Y$) scaled by that in the FPA FOV (n_{FPA}) and the time it takes to acquire each interferogram (t_{INT}), which is a function of the inverse of the spectral resolution ($\Delta\nu$). SNR normalization increases the number of coadditions (n_C) for each FOV. For a scanning system, however, the scaling is not as straightforward (Eq. 7.2). Efficiency is maximized at peak stage velocity. One option is to accelerate to peak stage velocity as quickly as possible and to hold that velocity constant for the largest fraction of time. These abrupt dynamics tend to degrade SNR, increase instability due to overshoot, and lengthen settling time. Instead, the motion of the scanning stage follows a third order trajectory[146] to sweep the sample in s-curves

minimizing unwanted vibrations. The time to traverse each line (t_{LINE}) is dependent on its length; the number of pixels (n_X) nor the size of pixel (ΔX) alone do not affect scan times. Instead, scan times for each band is primarily scaled by the number of rows (n_Y). For small images, the fixed time (t_{INIT}) to refocus the image for chromatic correction as well as other initialization procedures described previously per frequency become dominant resulting in diminishing improvements. Lastly, the imaging time is scaled by the number of discrete frequencies bands selected (n_ν).

$$t_{FTIR} \propto n_C \left[\frac{n_X n_Y}{n_{FPA}} t_{INT}(\Delta\nu^{-1})\right] \quad 7.1$$

$$t_{QCL} \propto n_\nu \left[n_Y t_{LINE}\left(n_X \Delta X, \frac{dX}{dt}, \frac{d^2X}{dt^2}, \frac{d^3X}{dt^3}\right) + t_{INIT}\right] \quad 7.2$$

It is notable that high aspect ratios (n_X/n_Y) are more efficient for the scanning QCL system, whereas this value has no impact with the FT-IR system. The fast and slow axes (simplified as x and y, respectively) do not need to align with the microscopy stage axes and an appropriate rotation of the sample can improve efficiency. To compare the performance of these two approaches as simulated in **Figure 7.4A**, we assume the most favorable scenario for the widefield systems−we use square images from 0.1 μm up to 20 mm per side for comparisons. The minimum scan time for an image is given by a single QCL band or a single FT-IR coaddition. The upper bound is represented by hyperspectral QCL data with 250 bands at 4 cm^{-1} spacing covering the fingerprint spectral region or 256 FT-IR coadditions, which brings the SNR in line with that of the QCL. Under typical experimental parameters, however, we acquire between 10 and 30 QCL bands as this information is typically what is required in DFIR approaches to obtain information about biological samples. Similarly, a typical parameter for FT-IR imaging systems is 16 coadditions to achieve a reasonable SNR for tissue imaging, which is then augmented by postprocessing noise reduction. We do not include time required for this postacquisition noise rejection in our comparisons, though it can be substantial.

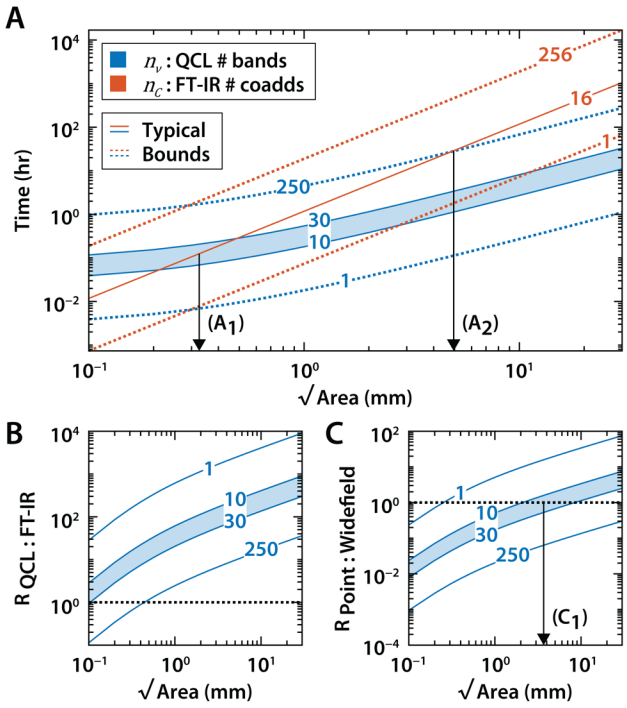

Figure 7.4. (A) Estimated imaging time for a square sample area linearly scaled by the number of frequency bands or coadditions for the DFIR and FT-IR systems, respectively. (B) The SNR-normalized pixel rate ratio of the QCL system to the FT-IR system. (C) The SNR normalized pixel rate ratio of the QCL point scanning system to a QCL widefield imaging system.

As we compare these systems and their current limits of performance, we emphasize that no system is globally preferred in all scenarios. A particular system is may be the preferred one depending on specific experimental conditions; we illustrate this situation using three scenarios next.

7.5.1 Case 1: Small samples below 300 µm

For an image the size of a single FOV, the FT-IR system simply sweeps the interferometer ($n_C t_{INT}$), whereas a scanning system must sweep the image line by line ($n_\nu n_Y t_{LINE}$). While we can reduce n_C and n_ν if appropriate, the inefficiency in turning the stage and rescanning each line (n_Y) makes QCL scanning impractical. Thus, for small areas, it is best to employ FT-IR imaging with a staring camera. The lower times to scan with the FT-IR system holds up to the crossover point (A_1) shown in **Figure 7.4A**. Under normal conditions, where we would need to acquire a reasonable set of discrete frequency bands, it is preferable to perform

this experiment using FT-IR at 16 coadditions or even 256 coadditions where the SNR between the systems is equivalent.

7.5.2 Case 2: Hyperspectral acquisition of samples up to 5 mm

The spectral multiplexing advantage of FT-IR interferometers remains up to moderately sized images (**Figure 7.4A**, A_2). Both systems take roughly a day to image this area, however the QCL system is limited to the fingerprint spectral region. Here we are assuming an experiment that draws no advantage from the ability of discrete band selection. This is often the case for completely unknown samples in which discovery of new information is targeted. Once prior information becomes available and the spectral set is reducible, the speed advantage of DFIR scanning grows to an order of magnitude.

7.5.3 Case 3: Large Samples

The advantage of QCL DFIR systems is most significant when being used to screen large areas. For instance, 20 mm samples such as tissue surgical sections or microarrays, can be imaged in a day with a typical band set, whereas this task would take an FT-IR system upward of 1000 h while still obtaining lower SNR. A means to quantitatively compare performance is to normalize ratings by noise (σ) and the number of pixels (n) required to cover a fixed area as follows:

$$R_{2:1} = \frac{n_2}{n_1}\frac{t_1}{t_2}\left(\frac{\sigma_1}{\sigma_2}\right)^2 \qquad 7.3$$

These relations are shown in **Figure 7.4B**, where the QCL point scanning time is compared for different numbers of bands against FT-IR imaging with the dotted line indicating parity. On a per pixel basis when SNR is equivalent, the FT-IR system can surpass the QCL system only when hyperspectral data is required, and even so only for small images. In all other cases, the QCL is faster and its advantage climbs rapidly as SNR required increases or spectral bands needed decrease. It is also instructive to compare the point scanning system against a widefield QCL based system previously reported using the same FPA detector as used in widefield FT-IR imaging. In **Figure 7.4**C, performance of a widefield QCL DFIR system[88] is compared to the point system, where it is evident that array detectors are faster up to midsized

images (C1). These metrics, however, do not account for image quality where minimization of artifacts and aberrations allow for laser-based point scanning techniques to be dominant.

The comparison of widefield and point DFIR systems demonstrates that the QCL point scanning, DFIR approach can be a candidate of choice for scanning large areas at limited spectral bands. Hence, we sought to optimize image quality and speed up spectral acquisition. First, we evaluate the image resolving performance of our designed system against the state- of-the-art commercial FT-IR imaging system by measuring the contrast of an USAF 1951 resolution test target consisting of groups of progressively smaller features. The features of these negative chrome on glass targets broadly absorb IR frequencies while the background is highly reflective. These targets allow us to determine the resolution within the absorbance image across all spectral positions. From these measurements, in **Figure 7.5A**, we observe that the resolving power of the QCL system (1 μm pixels) far exceeds that of a FTIR system (1.1 μm pixels). Refractive optics focus all the light incident on the lens aperture to a single point. Since this is a stage-scanning system, the focal point is always on axis with minimal field-induced aberrations. The performance, which is proportional to wavenumber, is described by the modulation transfer function (MTF) curves that indicate how accurately a system reproduces contrast with increasing spatial frequency (**Figure 7.5B** top). The use of refractive materials, however, has well-known drawbacks of not being able to simultaneously focus across a wide spectral range. Since the developed laser imaging spectrometer is a DF system, chromatic focal shifts are easily correctable mechanically, while losses due to attenuation of the material and limits of the antireflection coating are mitigated by higher source power.

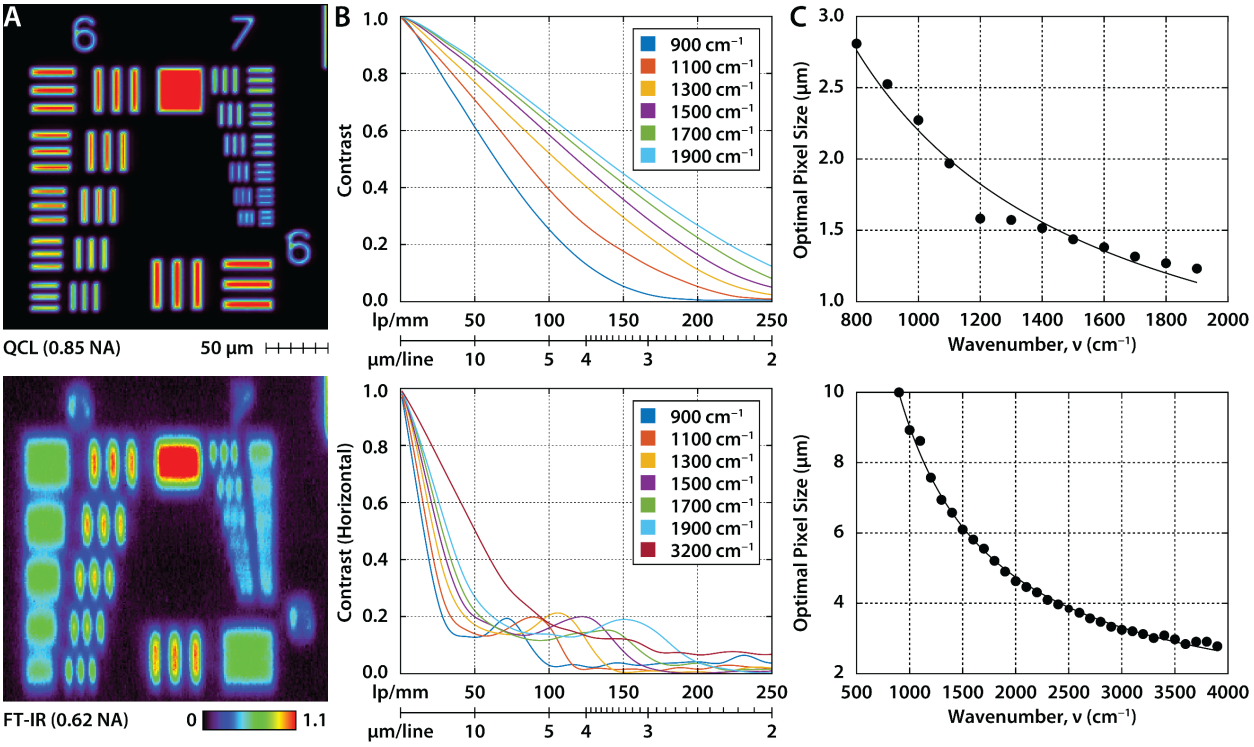

Figure 7.5. Spatial resolution characteristics of a QCL microscope (top row) and a FT-IR imaging spectrometer (bottom row). (A) Absorbance images of USAF 1951 chrome on glass negative resolution test target images of groups 6 and 7. (B) Modulation transfer function (MTF) curves showing the reflectance contrast decay with increasing spatial frequency per wavenumber measured from a slant-edge. (C) Ideal pixel size measurements per wavenumber with a fitted trendline.

None of these corrections are feasible with FT-IR systems; since the broad spectral range is simultaneously acquired, they are designed with reflective optics.[147] A reflective Schwarzschild objective focuses light without introducing chromatic aberrations using two reflective surfaces. Unlike a refractive singlet, these reflective objectives are corrected for third-order aberrations making them viable for widefield imaging. However, there is a trade-off between resolution and light throughput due to the large hole in the primary reflector. A larger obscuration allows for increased light throughput up to a limit but reduces the inner NA of the objective. This obscuration acts as a Fourier filter reducing the contrast of the lower spatial frequencies as evident by the stepped drop (**Figure 7.5B** bottom). Additionally, in epi-illumination configuration, a mirror is rotated above the objective to direct the light to the sample and consequently blocks half of the light returning to the detector. Unlike a refractive beam splitter that evenly attenuates the beam but introduces other chromatic issues, the mirror

completely blocks half the angular aperture but only in the vertical direction. The horizontal direction remains unaffected, thereby causing significant asymmetric blurring in the images. For trans- illuminated images we expect the vertical MTF to match the horizontal MTF.

From these MTF measurements, we can calculate the optimal pixel size as half the resolution where the contrast falls below the 26% specification of the Rayleigh criterion which is considered reasonable for common microscopy applications. As shown in **Figure 7.5C**, the pixel size is inversely proportional to the wavenumber and often considered to be no larger than the highest utilized band to prevent aliasing by under-sampling. Due to the large wavenumber range that spans the mid-infrared fingerprint region, considerable oversampling is inevitable. When pixel sizes are kept consistent, halving the wavenumber would result in 4-fold undersized pixels, increased scan times, and excess data processing requirements. Fourier transform systems especially have low data efficiency as they cannot decouple magnification from spectral information. Even camera- based discrete frequency systems cannot easily change magnification without additional optics. Only DF systems that employ point scanning for imaging formation allow for arbitrary pixel sizes that can be precisely adjusted to the optimal value for each wavenumber. The pixel sampling is triggered by the stage encoder to any multiple of encoder ticks, which is spaced 50 nm in this hardware. Instead of acquiring a data cube where each wavenumber slice has an equal number of pixels, we can accelerate this by avoiding over sampling and imaging the sample area always at appropriate resolution. Of course, such an approach would need a careful interpolation of the data to ensure ease of data processing and assuring that spectral fidelity from each location is maintained as well as noting that the localized region from which each analytical result is derived changes with wavenumber. The same happens currently in any imaging system, of course, given the changing point spread function. The result above not only demonstrates that this varying pixel size is a possibility but also provides the optimal size, which can help optimize designs of the future that employ optimal spatial sampling to speed up data acquisition.

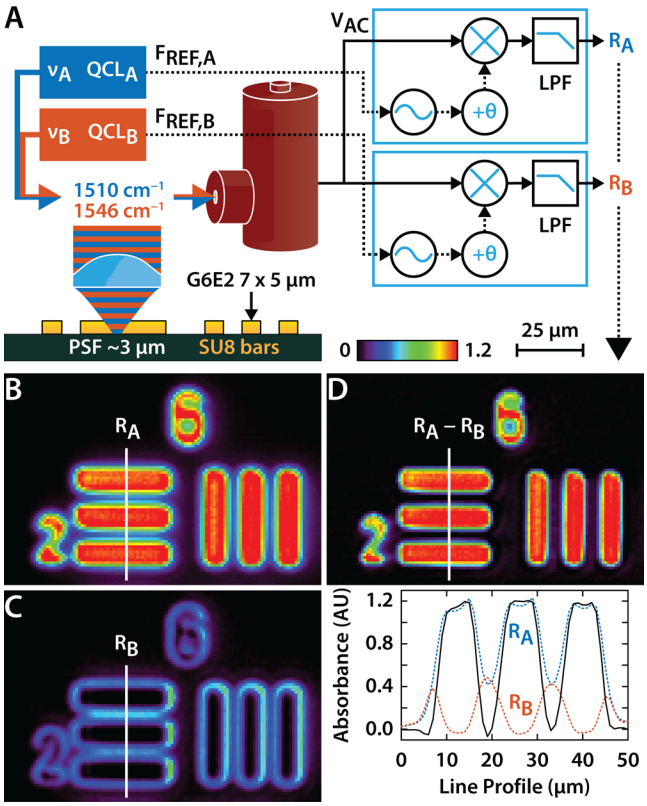

Figure 7.6. (A) Schematic of a DFIR microscope with a simultaneous multicolor acquisition scheme. In this setup, each color illuminates the sample with a unique repetition rate. The recorded signal is demodulated at the respective reference frequencies by a multichannel lock-in amplifier. SU-8 photoresist bars on low-e reflective glass acquired at (B) an absorbing wavenumber and (C) a nonabsorbing wavenumber. (D) The difference image cancels scattering contributions resulting in a corrected absorbance image.

Another approach to speed data collection is to employ multiplexing.[148–150] Current QCL imaging systems do not address the loss of spectral multiplexing inherently advantageous when using FT systems. Despite modern configurations commonly consisting of four individual QCL lasers per microscope to span the fingerprint region, only one laser is transmitted at a time. Each discrete band in the set is measured sequentially while the other 3 lasers remain idle representing a clear inefficiency. IR detectors simply measure the intensity of irradiance without any information regarding the incident wavelength. Therefore, when using slower detectors that measure the average power of the laser, only one laser can be active at once. While it may be possible to use multiple detectors and a series of cutoff filters, such a system would have cross-talk relative to the quality factor of the filter and, therefore, have limited practicality.

We present a detection scheme that demodulates multiple incident beams to allow multiple spectral bands to be acquired simultaneously on a single detector as shown in **Figure 7.6A**. Two essentially identical but separate laser assemblies, each with 4 laser tuners, are colinearly aligned with a beam splitter. This arrangement eventually can be replaced with a single laser system with completely independent tuners, but as of this study, no commercial system with this capability is available. The combined beam is passed through the QCL microscope as for a single frequency but with the lasers emitting at slightly different repetition rates. A digital lock-in amplifier equipped with multiple demodulator units, each locked to respective reference frequencies, separate the signals from each laser. The first consequence is that the data acquisition is further sped up by a factor of 2. The same approach may be adopted for even further multiplexing with emerging multicolor QCL lasers.[151]

While measuring multiple gas or liquid species has been shown to be possible, one unique application of multiplexing is to actively remove scattering effects in the recorded data that arise from refractive index mismatches at domain boundaries. We have imaged SU-8 photoresist bars that are 7 μm wide and 5 μm thick. These are relatively small structures that are roughly the same size scale as the PSF. A key band set that is reduced from and representative of the full spectrum typically contains absorbing and baseline pairs that can be imaged simultaneously. As can be seen when imaging the photoresist at an absorbing wavenumber (**Figure 7.6B**), edge scattering is clearly visible and reduces the image contrast by approximately half according to the vertical line profile. At a nonabsorbing wavenumber, which could be used for baseline correction in a continuous spectrum, only scattering-induced features are present in the attenuated beam. These are well-known to arise from refractive index mismatches at boundaries (**Figure 7.6C**). Using the dual color system here, we record only the differential signal (**Figure 7.6D**) that is the scattering corrected absorbance normally used for analysis. As shown by the line profile from **Figure 7.6D**, the edge scattering contributions are clearly observed and duly subtracted in real time. For any sample, the precise wavenumbers for absorption bands and nonabsorbing spectral regions can be quickly determined using the rapid scanning spectrometer described in Figure 2. Simultaneous multicolor imaging, while common across other microscopy modalities, has yet to be broadly implemented for mid-infrared discrete frequency microspectroscopy. When 4-tuner QCL laser systems that are truly independent become available, no additional design changes are expected to pair with existing 4-demodulator

lock- in amplifiers. But as development of multichannel QCL chips consisting of larger arrays become more prevalent, this may exceed capabilities feasible with lock-in amplifiers. Nevertheless, the ability to compress large numbers of frequency bands into a single receiver is well-known in the telecom industry and many of these techniques can be implemented in future iterations of discrete frequency microscopy systems as IR laser technology continues to advance.

7.6 Conclusions

In this study, we describe and characterize a DFIR point scanning spectrometer and compare it to state-of-the-art commercial FT-IR spectroscopic imaging systems. The separation of magnification from optics or sensors, and arbitrarily controllable by software, allows us to optimize imaging parameters to prevent oversampling, minimize scan times, and reduce data overhead. Consequently, the performance of the system reported here exceeds that of previous QCL imaging or mapping systems as well as a leading FT-IR imaging system. We demonstrate the experimental parameter space where the performance of the DFIR system exceeds that of FT-IR widefield imaging whereas the spectral quality exceeds that of any point or widefield FT-IR imaging spectrometer. Finally, we show marked improvements in spatial image quality with the new optical design. Further advancement though multicolor mapping demonstrates potential to provide corrected absorbance images or multiplexed chemical information. These extensions in performance exceed current state of the art in both spectral and spatial data quality and provide exciting new opportunities for advancing IR imaging technology.

CHAPTER 8: VERSION 2.3 – SYNTHETIC HOLOGRAPHIC IMAGING

8.1 Abstract

In previous chapters, we have built a flexible, open source, discrete frequency imaging platform not previously available. This presents us with many new opportunities to develop techniques that would otherwise be incompatible or difficult to implement with commercial infrared imaging systems. Here we consider the addition of Synthetic Optical Holography[152] capabilities to our platform, where Digital Off-axis Holography (DOH) is combined with Scanning Probe Microscopy (SPM), and investigate its applicability towards infrared spectroscopic imaging.

8.2 Methods

We begin with the stage scanning microscope system[124,153] and use the other half of the input beam that was previously dumped as a phase-shifted reference instead. As shown in **Figure 8.1**, the beam block has been replaced with a piezo mounted reference mirror and an electronic shutter which the system automatically closes when executing non-holographic functions such as autofocusing, recording point spectra, and certain calibration subroutines.

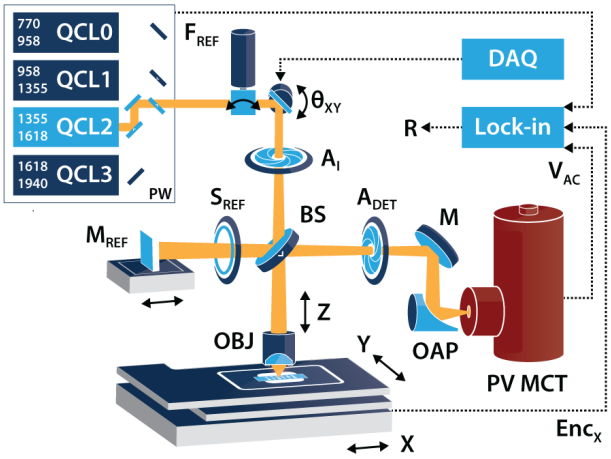

Figure 8.1. Schematic of a QCL-based point scanning microscope with a reference arm enabling holographic imaging.

The theoretical background of this technique[152] is similar to off-axis wide-field holography. The field from the sample $\boldsymbol{U_S(r)}$ interferes with the reference field $\boldsymbol{U_R(r)}$ at each

position $\boldsymbol{r}$, where $\boldsymbol{U_R(r) = A_R e^{i\phi_R(r)}}$ with amplitude $\boldsymbol{A_R}$ and phase $\boldsymbol{\phi_R(r)}$. By adjusting the piezo stage, we control the optical path difference between the sample and reference arms of this interferometer. The recorded detector signal is the intensity resulting from the intereference between the two beams (Eq 8.1). Using a spatial Fourier transform (FT), we have the demodulated autocorrelation term $\boldsymbol{C(q)}$, a DC value in the Fourier domain, as well as a pair of shifted complex conjugates $\boldsymbol{A_R^* \tilde{U}_S}$ and $\boldsymbol{A_R \tilde{U}_S^*}$ (Eq. 8.2) from which we can reconstruct the amplitude and phase of the sample through filtering and an inverse FT.

$$\boldsymbol{I(r) = |U_S(r)|^2 + |U_R(r)|^2 + U_R(r)U_S^*(r) + U_R^*(r)U_S(r)} \quad 8.1$$

$$\boldsymbol{\tilde{I}(q) = \tilde{C}(q) + A_R \tilde{U}_S^*(k-q) + A_R^* \tilde{U}_S(k+q)} \quad 8.2$$

8.3 Results

We demonstrate this technique on a SU-8 photoresist USAF 1951 test target patterned on a IR reflective low-e microscope slide at 5 µm thickness. The image is super-sampled at 4-fold the diffraction limited pixel size and for each row, the reference mirror is phase shifted by an additional quarter wave. An alternate option to limit errors associated with small step movements is to acquire the full image at the normal diffraction limited pixel size at each phase shift.

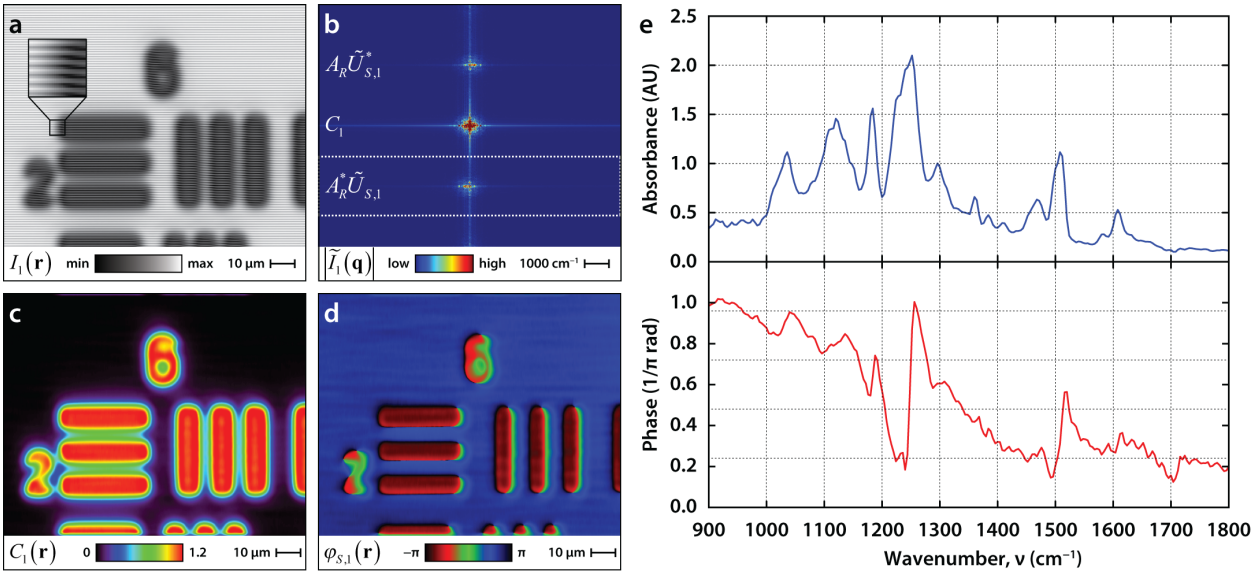

Figure 8.2. Holographic hyperspectral data set of an SU-8 photoresist USAF 1951 test target patterned on a IR reflective low-e microscope slide at 5 µm thickness.

The raw holographic image is shown in **Figure 8.2A** (Eq 8.1) and its Fourier transform in **Figure 8.2B** (Eq. 8.2). By taking the inverse FT of the windowed DC component $\widetilde{\boldsymbol{C}}(\boldsymbol{q})$, we recover the image shown in **Figure 8.2C**. Lastly, the phase information shown in **Figure 8.2D** is computed by windowing the direct or conjugate images, $\boldsymbol{A}_{\boldsymbol{R}}^{*}\widetilde{\boldsymbol{U}}_{\boldsymbol{S}}$ or $\boldsymbol{A}_{\boldsymbol{R}}\widetilde{\boldsymbol{U}}_{\boldsymbol{S}}^{*}$ respectively, shifting by $\boldsymbol{k}$ back to DC, followed by an inverse FT. The computation is then performed on all spectral bands and referenced to the background to obtain the absorbance and phase spectrums shown in **Figure 8.2E**.

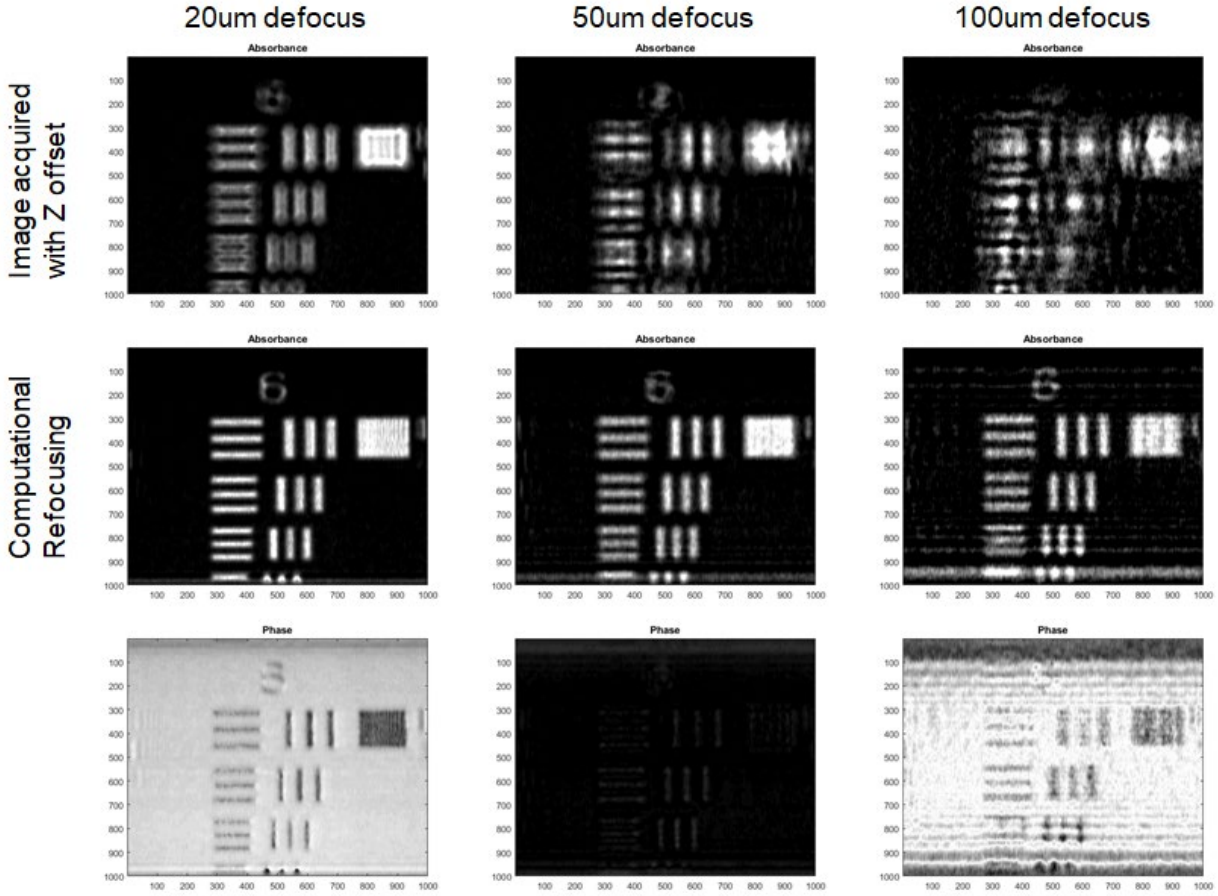

Figure 8.3. Computational refocusing using holographic images of a chrome on glass test target.

In this demonstration, we image the sample out of focus by a distance $\boldsymbol{Z}$ and apply a transfer function (Eq. 8.3) on $\tilde{\boldsymbol{I}}(\boldsymbol{q})$ that propagates the field back to the point of best focus.

$$\boldsymbol{H} = \boldsymbol{e}^{\boldsymbol{i2\pi\frac{Z}{\lambda}}}\boldsymbol{e}^{-\boldsymbol{i\pi\lambda Z(u^2+v^2)}} \tag{8.3}$$

CHAPTER 9: VERSION 3.0 – LASER SCANNING IMAGING

9.1 Abstract

The most established technique for laser imaging is in the visible wavelengths where galvanometer-controlled beam steering is combined with high-speed single element detectors. In the infrared, many laser welding and cutting instruments also operate in this manner. Yet, all the designs for infrared chemical imaging that were discussed in previous chapters as well as thus far in literature implement less efficient alternatives that have not been as successful for other applications. This is because the laser scanning design incorporates three complicated optical assemblies: a scan lens (SL), tube lens (TL), and objective (OBJ), each consisting of multiple materials and aspheric lens elements. For infrared chemical imaging, these optics must be corrected for field aberrations while being restricted to the few and significantly more expensive IR transparent glasses or crystals suitable for manufacturing lenses. Furthermore, these designs must be corrected for chromatic aberrations across a wavelength range 10-fold larger than the visible spectrum. In this chapter, we detail designs for these optical assemblies, demonstrate successful fabrication, and present our on-going work toward delivering an infrared broadband laser scanning microscope.

9.2 Introduction

The recent use of quantum cascade lasers (QCL) for infrared spectroscopic microscopy has enabled discreet frequency chemical imaging at speeds orders of magnitude faster than previously possible. While a QCL can be adapted to existing infrared microscopes with moderate changes, as we approach diffraction-limited performance requirements, a full redesign is required. Mid-infrared optics for microscopy that are both well-corrected over a reasonable field of view and a broad wavelength range are not available commercially.

We have implemented several designs for QCL wide-field microscopes. We combined a QCL with a Varian UMA 600 microscope containing completely reflective relay optics with stock Schwarzschild objectives which resulted in the first QCL images at the time[64]. The Schwarzschild objectives contain an obscuration that degrades image quality, so such option is no longer viable. Redesigning the reflective microscope using stock spherical mirror relays and using a stock refractive singlet lens as an objective yielded improvement in image quality[88].

However, there are still numerous shortcomings. Due to spherical optics, spherical aberration is inevitable. Due to reflective optics, a non-zero incident angle is required. If we want to decrease aberrations, we must decrease the incident angle, but in turn this causes the path lengths and the microscope to become large. The aspheric refractive objective is only diffraction limited for one wavelength and on axis at the center pixel.

The consequence is that our microscope only functions ideally at one pixel at one wavelength. We must move to compound optics. To address these issues, we have a few options. A microscope objective is designed similarly to infrared camera lens which are commercially prevalent. The camera lens can provide magnification if installed in the reversed direction with an additional focusing lens. Camera lenses will be achromatic and field corrected, albeit less so than microscope objectives, but this configuration will still be an improvement. The major difference between the two is that camera lenses are typically not designed to be telecentric. Such a shortcut would result in magnification error, parallax error, and nonsymmetric blurring. Spectrometers are typically designed in reflective configuration to eliminate chromatic aberration. We can implement field correction using multiple aspheric reflective surfaces, for instance, an anastigmat corrected for spherical aberration, coma, and astigmatism. However, the assembly is relatively large, has inconvenient sample positioning, and relatively low numeric aperture (0.2). The only commercial option is a FLIR close-up lens which has a NA of 0.35 and a spatial resolution of 25 μm. Furthermore, the lenses are optimized for a 7.5-13 μm wavelength range. This would not be ideal for tissue imaging which has strong amide absorbances in the 6-7 μm wavelength range.

Our presented solution is to design a well-corrected microscope objective and tube lens assembly. This infinite conjugate design follows modern visible microscope design principles. The infinite design allows us to insert other optics such as filters, beamsplitters, and polarizers into imaging path without distorting the image quality. No comparable design with these capabilities has been reported.

9.3 Design

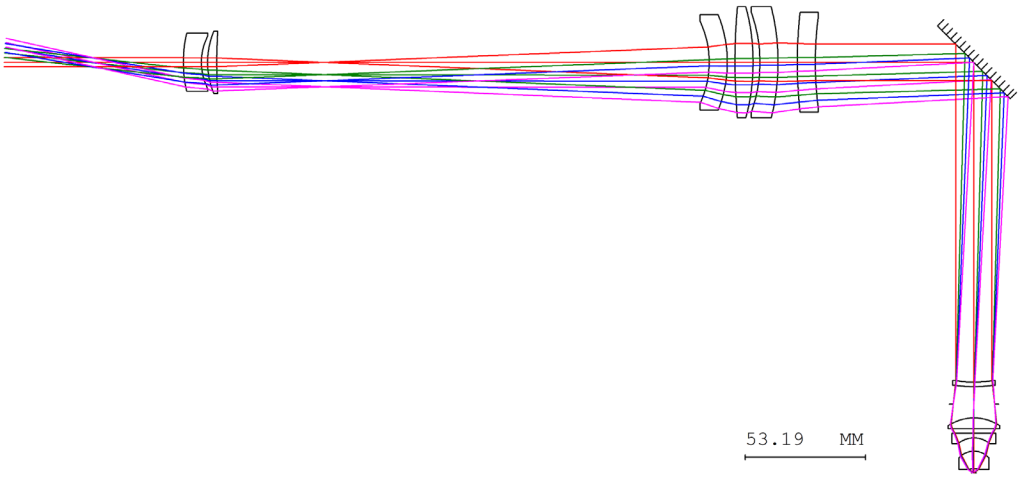

Figure 9.1. The infinity-corrected optical layout of the laser scanning QCL microscope consisting of a 4X scan lens, a 200 mm EFL tube lens, a low-magnification 10X/0.4NA microscope objective (not shown), and high-magnification 20X/0.8NA (shown) objective.

PERFORMANCE	WF system[88]	10X	20X
NA	0.56	0.4	0.8
Pixel size (µm)	2	4	2
FOV diameter (mm)	0.256	2.2	1.1
Spatial resolution (cycles/mm)	45 – 77	66	128
Design wavelength (µm)	2.5	5.2-12	5.2-12
AR range (µm)	8-12	5.2-12	5.2-12
Corrected wavelengths	1	3	3
Max chromatic focal length shift (µm)	49	2.4	0.5
RMS spot size, center-edge (µm)	14-27	1.0-1.4	1.7-1.8
Max ray aberration (µm)	68	4.6	5.2
Max optical path diff. (waves)	1.653	0.057	0.112
Max astigmatism (µm)	6	2.7	1.3
Max distortion (%)	0.1	3.3	3.4

Table 9.1. Designed system specifications compared to a widefield system[88] designed only with stock optics.

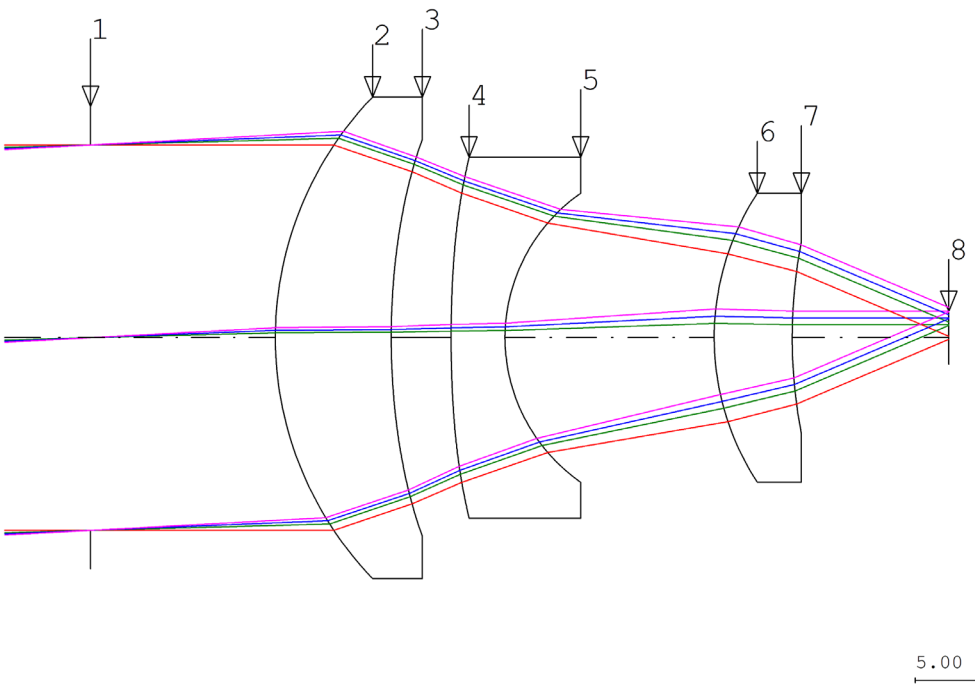

Surface		Y Radius	Thickness	Glass Code
STOP	Sphere		7.558903	
2	Sphere	14.56207	4.743832	CLRTRAN
3	Asphere	31.07585	2.447917	
4	Asphere	51.97814	2.202383	BAF2
5	Sphere	7.36805	8.555878	
6	Sphere	11.09889	3.190482	CLRTRAN
7	Sphere	21.47800	6.326050	

Aspheres		
Surface	**3**	**4**
Conic (K)	-1.50013E+00	4.32646E+01
4th order	3.46483E-05	2.57100E-05
6th order	2.00132E-07	9.91355E-07
8th order	-6.35477E-09	-7.54010E-08
10th order	1.04914E-10	1.67431E-09
12th order	-6.12798E-13	-1.59125E-11

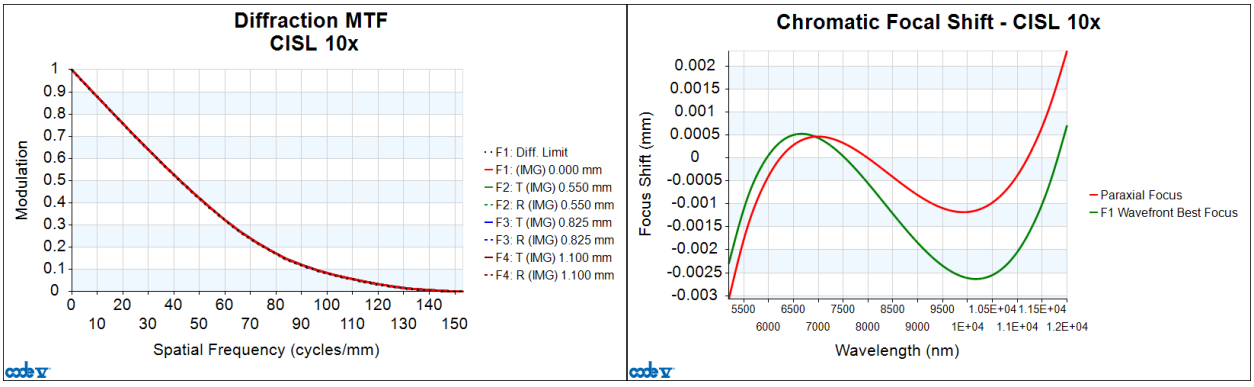

Figure 9.2. Optical design of the 10X/0.4NA microscope objective.

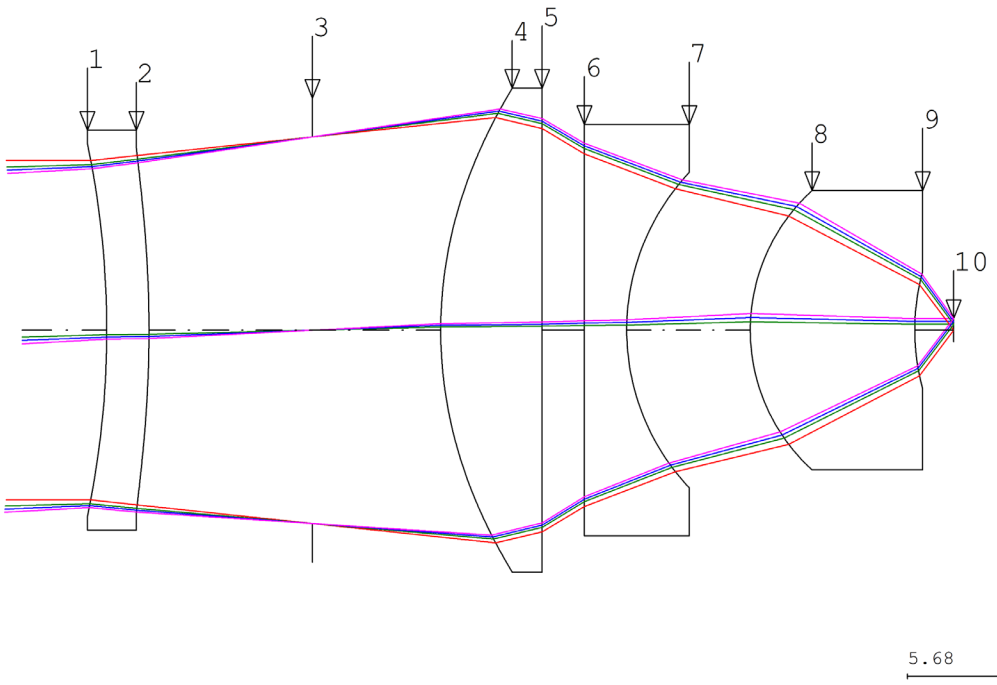

Surface		Y Radius	Thickness	Glass Code
1	Sphere	-42.81870	2.000000	
2	Asphere	-54.10282	7.717564	ZNSE
STOP	Sphere		6.058383	
4	Asphere	20.01517	4.783476	CLRTRAN
5	Sphere		2.000000	
6	Sphere		2.000000	BAF2
7	Sphere	10.85286	5.836154	
8	Sphere	8.89458	7.769199	ZNSE
9	Sphere	10.49225	1.835223	

Aspheres		
Surface	**2**	**4**
Conic (K)	9.91766E-01	-6.01705E-01
4th order	1.31296E-05	3.05056E-06
6th order	3.73500E-08	-1.48997E-08
8th order	-1.10605E-11	-4.60958E-11
10th order	2.09295E-12	9.45898E-15

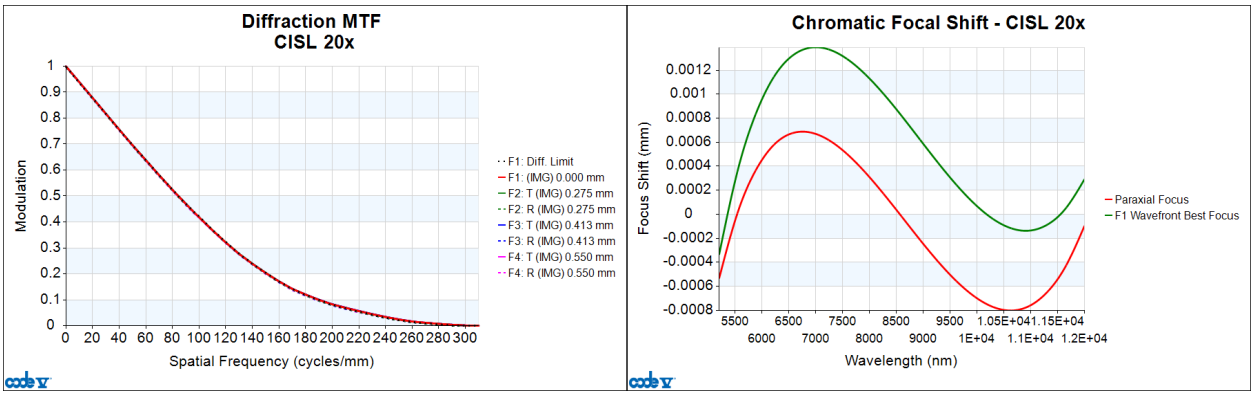

Figure 9.3. Optical design of the 20X/0.8NA microscope objective.

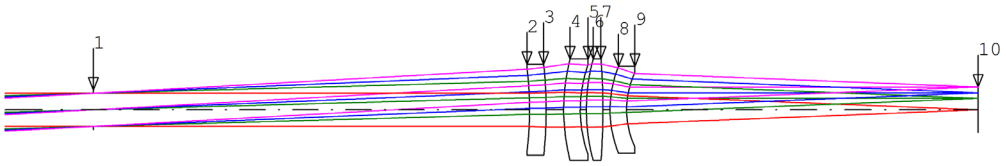

Surface		Y Radius	Thickness	Glass Code
STOP	Sphere		211.0000	
2	Asphere	-167.662	8.0000	GE
3	Sphere	-201.818	8.5000	
4	Sphere	100.663	8.0000	ZNSE
5	Sphere	65.245	3.0000	
6	Asphere	100.672	8.0000	IRG24
7	Sphere	-290.832	3.4000	
8	Sphere	56.146	8.0000	GE
9	Sphere	42.434	170.0000	

Aspheres		
Surface	**2**	**6**
Conic (K)	-5.11558E-03	5.50328E-03
4th order	-5.34824E-07	7.84189E-07
6th order	5.38176E-11	-1.86189E-10
8th order	-1.00920E-14	5.08952E-14
10th order	-1.02227E-18	1.07468E-17

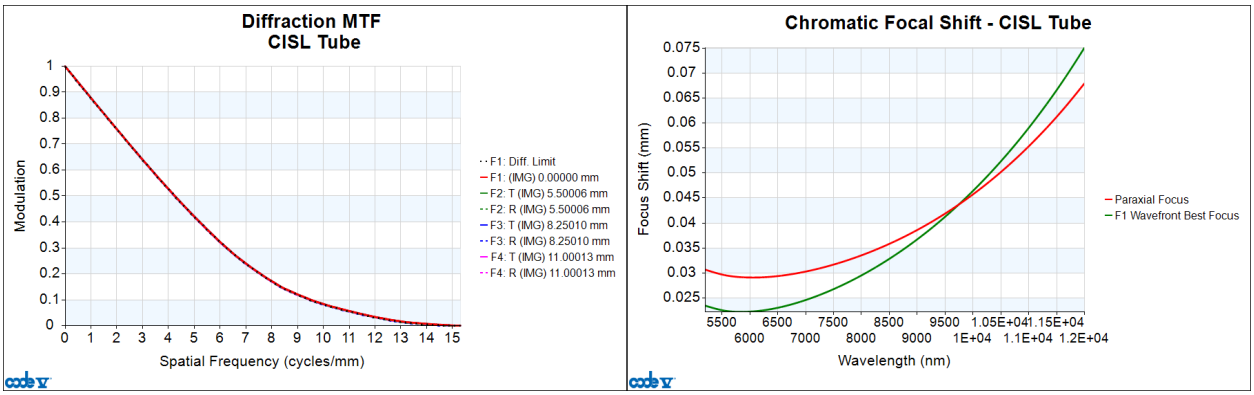

Figure 9.4. Optical design of the 200 mm EFL tube lens.

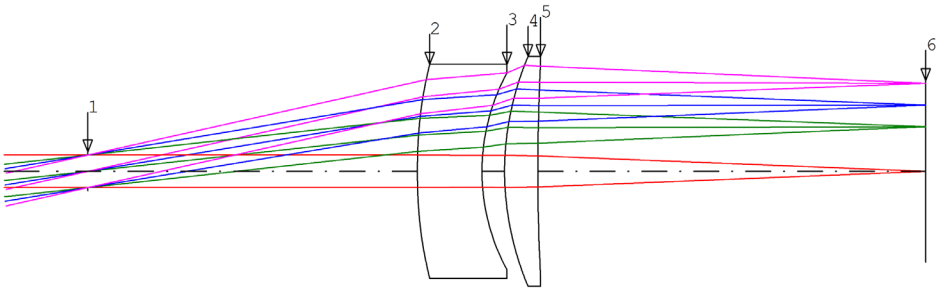

14.71 MM

Surface		Y Radius	Thickness	Glass Code
STOP	Sphere		40.326106	
2	Asphere	69.10727	7.900288	BAF2
3	Sphere	25.20355	2.770394	
4	Asphere	35.01744	4.060058	CLRTRAN
5	Sphere	254.05721	47.456475	

Aspheres		
Surface	**2**	**6**
Conic (K)	0.00000E+00	0.00000E+00
4th order	9.25519E-06	-2.75031E-06
6th order	3.34204E-08	4.69974E-09
8th order	-1.15535E-10	-4.81138E-11
10th order	-6.15874E-13	2.30915E-13

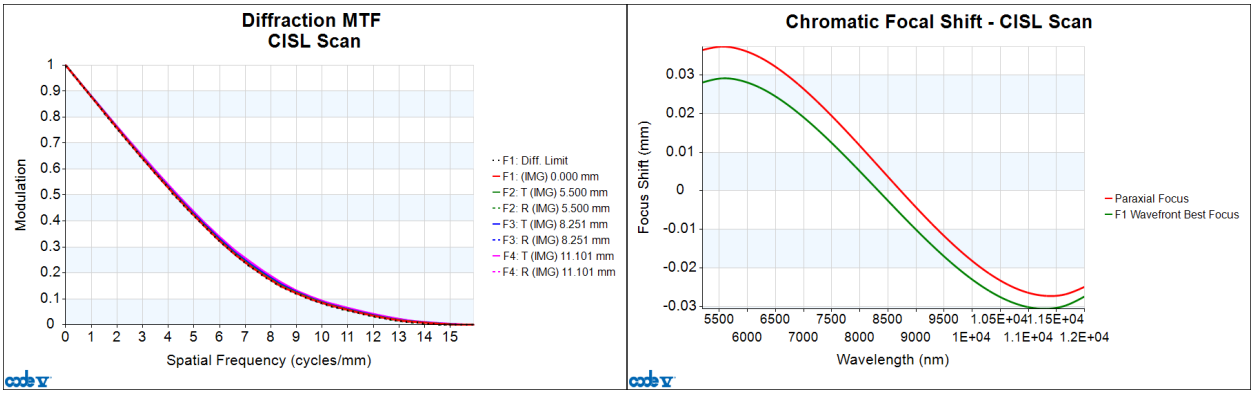

Figure 9.5. Optical design of the 4X scan lens.

PWL	AMTIR1	GAAS	GE	ZNSE	ZNS	CLRTRAN	GASIR1	BAF2	AMTIR2	IRG26	IG2	IG6
5000	2.511421	3.301047	4.016285	2.429527	2.246575	2.246616	2.507106	1.451024	2.779586	2.790898	2.510305	2.791030
5400	2.510366	3.299098	4.014072	2.428083	2.243982	2.244120	2.506113	1.448391	2.778575	2.789711	2.509278	2.789835
5800	2.509341	3.297266	4.012299	2.426603	2.241226	2.241463	2.505163	1.445543	2.777677	2.788621	2.508288	2.788738
6200	2.508326	3.295504	4.010856	2.425071	2.238295	2.238630	2.504233	1.442476	2.776855	2.787596	2.507314	2.787706
6600	2.507305	3.293778	4.009661	2.423476	2.235179	2.235608	2.503307	1.439184	2.776078	2.786608	2.506338	2.786711
7000	2.506269	3.292062	4.008659	2.421809	2.231868	2.232388	2.502372	1.435662	2.775327	2.785641	2.505347	2.785737
7400	2.505210	3.290338	4.007809	2.420063	2.228354	2.228958	2.501419	1.431905	2.774585	2.784682	2.504332	2.784770
7800	2.504122	3.288590	4.007078	2.418232	2.224628	2.225309	2.500440	1.427908	2.773837	2.783719	2.503286	2.783799
8200	2.503001	3.286806	4.006444	2.416310	2.220681	2.221430	2.499430	1.423664	2.773070	2.782746	2.502201	2.782818
8600	2.501845	3.284975	4.005888	2.414294	2.216504	2.217311	2.498383	1.419167	2.772275	2.781755	2.501073	2.781819
9000	2.500649	3.283088	4.005396	2.412179	2.212085	2.212942	2.497296	1.414409	2.771439	2.780742	2.499895	2.780797
9400	2.499414	3.281135	4.004958	2.409962	2.207415	2.208312	2.496163	1.409384	2.770552	2.779703	2.498665	2.779750
9800	2.498139	3.279110	4.004563	2.407640	2.202480	2.203408	2.494981	1.404083	2.769602	2.778635	2.497378	2.778672
10200	2.496821	3.277002	4.004205	2.405207	2.197269	2.198218	2.493747	1.398498	2.768578	2.777534	2.496029	2.777561
10600	2.495462	3.274804	4.003878	2.402662	2.191765	2.192728	2.492457	1.392619	2.767463	2.776398	2.494616	2.776416
11000	2.494061	3.272505	4.003577	2.399999	2.185953	2.186923	2.491108	1.386437	2.766243	2.775226	2.493133	2.775232
11400	2.492619	3.270095	4.003298	2.397217	2.179815	2.180788	2.489696	1.379940	2.764899	2.774014	2.491578	2.774009
11800	2.491137	3.267563	4.003038	2.394311	2.173332	2.174306	2.488217	1.373118	2.763407	2.772761	2.489946	2.772745
12200	2.489616	3.264898	4.002794	2.391277	2.166482	2.167457	2.486668	1.365958	2.761739	2.771466	2.488233	2.771438
12600	2.488057	3.262086	4.002563	2.388111	2.159243	2.160223	2.485045	1.358447	2.759862	2.770126	2.486435	2.770087
13000	2.486462	3.259113	4.002343	2.384809	2.151589	2.152580	2.483344	1.350570	2.757731	2.768741	2.484546	2.768689

Figure 9.6. Refractive indices of allowed glass codes over the designed wavelength range (PWL) (nm).

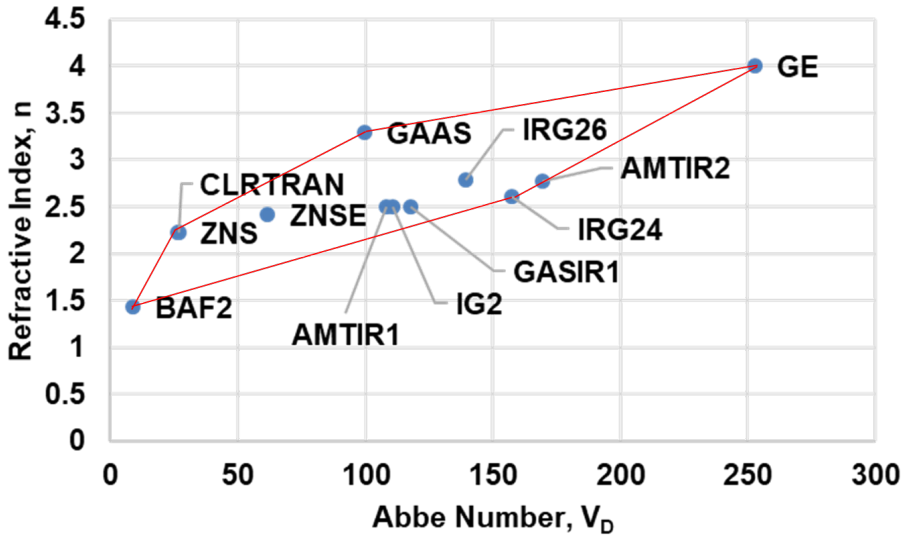

Figure 9.7. Glass map boundary of allowed glass codes for the optimizer over the designed wavelength range.

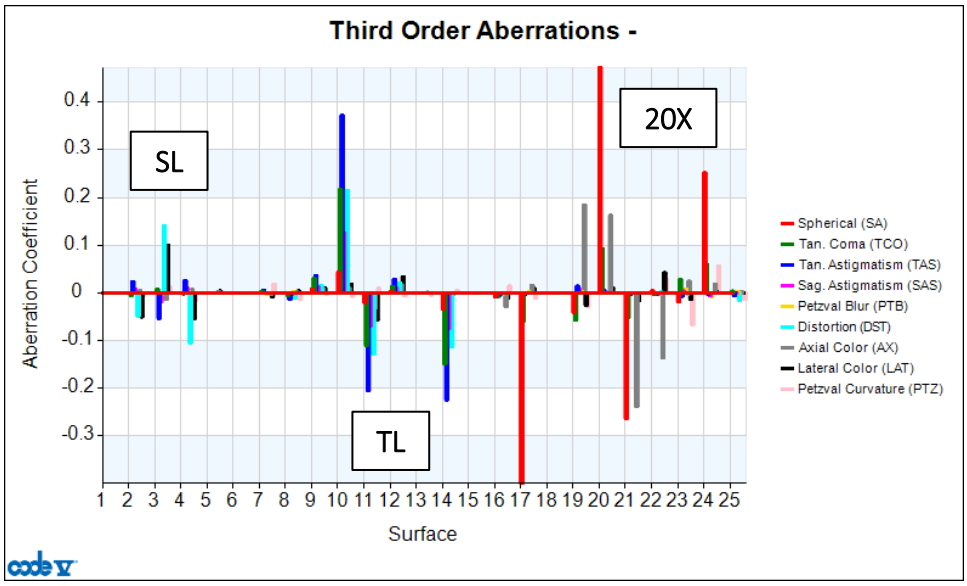

Figure 9.8. The distribution of third order aberration corrections over each optical surface in the scan lens (SL), tube lens (TL), and the 20X objective in the complete model.

9.4 Software

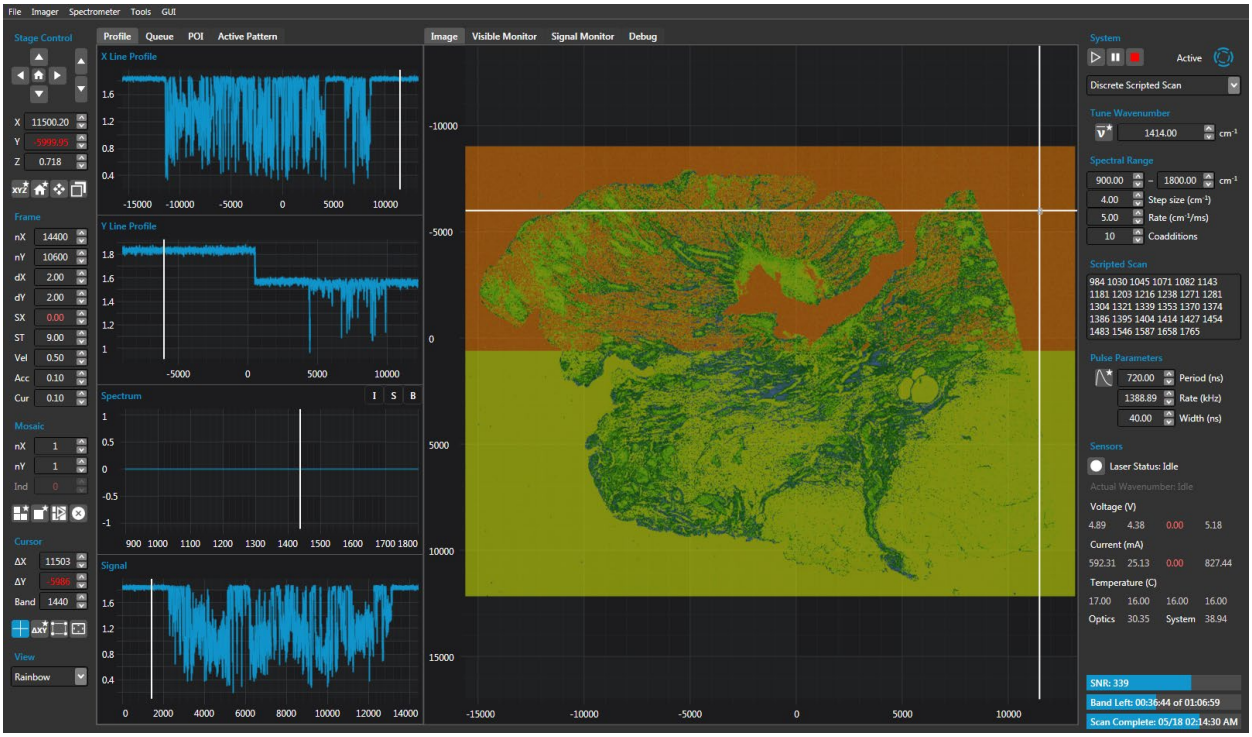

Figure 9.9. Source code repository hosted at https://github.com/yehkevin/QCL-PT

REFERENCES

(1) Bhargava, R.; Levin, I. W. Fourier Transform Infrared Imaging: Theory and Practice. *Anal. Chem.* **2001**, *73* (21), 5157–5167.

(2) Saptari, V. *Fourier Transform Spectroscopy Instrumentation Engineering*; SPIE Press, 2004; Vol. 61.

(3) Griffiths, P.; Haseth, J. A. De. *Fourier Transform Infrared Spectrometry, 2nd Ed.*; John Wiley & Sons: Hoboken, NJ, 2007.

(4) Okamoto, T.; Kawata, S.; Minami, S. Optical Method for Resolution Enhancement in Photodiode Array Fourier Transform Spectroscopy. *Appl. Opt.* **1985**, *24* (23), 4221.

(5) The Infracord® Double Beam Spectrophotometer. *Chem. Eng. News* **1957**, *35* (33), 74.

(6) Levin, I. W.; Bhargava, R. Fourier Transform Infrared Vibrational Spectroscopic Imaging: Integrating Microscopy and Molecular Recognition. *Annu. Rev. Phys. Chem.* **2005**, *56* (1), 429–474.

(7) Bhargava, R.; Wall, B. G.; Koenig, J. L. Comparison of the FT-IR Mapping and Imaging Techniques Applied to Polymeric Systems. *Appl. Spectrosc.* **2000**, *54* (4), 470–479.

(8) Mohlenhoff, B.; Romeo, M.; Diem, M.; Wood, B. R. Mie-Type Scattering and Non-Beer-Lambert Absorption Behavior of Human Cells in Infrared Microspectroscopy. *Biophys. J.* **2005**, *88* (5), 3635–3640.

(9) Bassan, P.; Byrne, H. J.; Bonnier, F.; Lee, J.; Dumas, P.; Gardner, P. Resonant Mie Scattering in Infrared Spectroscopy of Biological Materials – Understanding the 'Dispersion Artefact.' *Analyst* **2009**, *134* (8), 1586.

(10) Lee, J.; Gazi, E.; Dwyer, J.; Brown, M. D.; Clarke, N. W.; Nicholson, J. M.; Gardner, P. Optical Artefacts in Transflection Mode FTIR Microspectroscopic Images of Single Cells on a Biological Support: The Effect of Back-Scattering into Collection Optics. *Analyst* **2007**, *132* (8), 750.

(11) Budevska, B. O. Minimization of Optical Non-Linearities in Fourier Transform-Infrared Microspectroscopic Imaging. *Vib. Spectrosc.* **2000**, *24* (1), 37–45.

(12) Nishikawa, Y.; Nakano, T.; Noda, I. Detection of Reversible Nonlinear Dynamic Responses of Polymer Films by Using Time-Resolved Soft-Pulse Compression Attenuated Total Reflection Step-Scan Fourier Transform Infrared Spectroscopy. *Appl. Spectrosc.* **2012**, *66* (3), 312–318.

(13) Elkins, K. M. Rapid Presumptive "Fingerprinting" of Body Fluids and Materials by Atr Ft-Ir Spectroscopy. *J. Forensic Sci.* **2011**, *56* (6), 1580–1587.

(14) Navas, N.; Romero-Pastor, J.; Manzano, E.; Cardell, C. Benefits of Applying Combined Diffuse Reflectance FTIR Spectroscopy and Principal Component Analysis for the Study of Blue Tempera Historical Painting. *Anal. Chim. Acta* **2008**, *630* (2), 141–149.

(15) Holton, S. E.; Walsh, M. J.; Bhargava, R. Subcellular Localization of Early Biochemical Transformations in Cancer-Activated Fibroblasts Using Infrared Spectroscopic Imaging. *Analyst* **2011**, *136* (14), 2953.

(16) Davis, B. J.; Carney, P. S.; Bhargava, R. Theory of Midinfrared Absorption Microspectroscopy: I. Homogeneous Samples. *Anal. Chem.* **2010**, *82* (9), 3474–3486.

(17) Davis, B. J.; Carney, P. S.; Bhargava, R. Theory of Mid-Infrared Absorption Microspectroscopy: II. Heterogeneous Samples. *Anal. Chem.* **2010**, *82* (9), 3487–3499.

(18) Reddy, R.; Davis, B.; Carney, P. S.; Bhargava, R. Modeling Fourier Transform Infrared Spectroscopic Imaging of Prostate and Breast Cancer Tissue Specimens. In *2011 IEEE International Symposium on Biomedical Imaging: From Nano to Macro*; IEEE, 2011; pp 738–741.

(19) Snively, C. M.; Katzenberger, S.; Oskarsdottir, G.; Lauterbach, J. Fourier-Transform Infrared Imaging Using a Rapid-Scan Spectrometer. *Opt. Lett.* **1999**, *24* (24), 1841.

(20) Snively, C. M.; Koenig, J. L. Characterizing the Performance of a Fast FT-IR Imaging Spectrometer. *Appl. Spectrosc.* **1999**, *53* (2), 170–177.

(21) Reddy, R. K.; Bhargava, R. Accurate Histopathology from Low Signal-to-Noise Ratio Spectroscopic Imaging Data. *Analyst* **2010**, *135* (11), 2818–2825.

(22) Lewis, E. N.; Treado, P. J.; Reeder, R. C.; Story, G. M.; Dowrey, a E.; Marcott, C.; Levin, I. W. Fourier Transform Spectroscopic Imaging Using an Infrared Focal-Plane Array Detector. *Anal. Chem.* **1995**, *67* (19), 3377–3381.

(23) Bhargava, R.; Jones, M. W. Infrared Spectroscopic Imaging: An Integrative Approach to Pathologyle. In *Nanobiophotonics Contributors*; The McGraw-Hill Companies, Inc., 2010; p 201.

(24) Bhargava, R.; Mintz, G. S. Fourier Transform-Infrared Spectroscopic Imaging: The Emerging Evolution from a Microscopy Tool to a Cancer Imaging Modality. *Spectroscopy* **2007**, *22*.

(25) Nasse, M. J.; Walsh, M. J.; Mattson, E. C.; Reininger, R.; Kajdacsy-Balla, A.; Macias, V.; Bhargava, R.; Hirschmugl, C. J. High-Resolution Fourier-Transform Infrared Chemical Imaging with Multiple Synchrotron Beams. *Nat. Methods* **2011**, *8* (5), 413–416.

(26) Patterson, B. M.; Havrilla, G. J.; Marcott, C.; Story, G. M. Infrared Microspectroscopic Imaging Using a Large Radius Germanium Internal Reflection Element and a Focal Plane Array Detector. *Appl. Spectrosc.* **2007**, *61* (11), 1147–1152.

(27) Walsh, M. J.; Kajdacsy-Balla, A.; Holton, S. E.; Bhargava, R. Attenuated Total Reflectance Fourier-Transform Infrared Spectroscopic Imaging for Breast Histopathology. *Vib. Spectrosc.* **2012**, *60*, 23–28.

(28) Nakhleh, R. E. Patient Safety and Error Reduction in Surgical Pathology. *Arch. Pathol. Lab. Med.* **2008**, *132* (2), 181–185.

(29) Walsh, M. J.; German, M. J.; Singh, M.; Pollock, H. M.; Hammiche, A.; Kyrgiou, M.; Stringfellow, H. F.; Paraskevaidis, E.; Martin-Hirsch, P. L.; Martin, F. L. IR Microspectroscopy: Potential Applications in Cervical Cancer Screening. *Cancer Lett.* **2007**, *246* (1–2), 1–11.

(30) Reddy, R. K.; Bhargava, R. Chemometric Methods for Biomedical Raman Spectroscopy and Imaging; 2010; pp 179–213.

(31) Bhargava, R. Towards a Practical Fourier Transform Infrared Chemical Imaging Protocol for Cancer Histopathology. *Anal. Bioanal. Chem.* **2007**, *389* (4), 1155–1169.

(32) Kwak, J. T.; Hewitt, S. M.; Sinha, S.; Bhargava, R. Multimodal Microscopy for Automated Histologic Analysis of Prostate Cancer. *BMC Cancer* **2011**, *11* (1), 62.

(33) Bhargava, R.; Kong, R. Structural and Biochemical Characterization of Engineered Tissue Using FTIR Spectroscopic Imaging: Melanoma Progression as an Example. *SPIE Proc.* **2008**, *6870*, 687004-687004–687010.

(34) Fernandez, D. C.; Bhargava, R.; Hewitt, S. M.; Levin, I. W. Infrared Spectroscopic Imaging for

Histopathologic Recognition. *Nat. Biotechnol.* **2005**, *23* (4), 469–474.

(35) Keith, F. N.; Kong, R.; Pryia, A.; Bhargava, R. Data Processing for Tissue Histopathology Using Fourier Transform Infrared Spectral Data. In *2006 Fortieth Asilomar Conference on Signals, Systems and Computers*; IEEE, 2006; pp 71–75.

(36) Mackanos, M. A.; Contag, C. H. FTIR Microspectroscopy for Improved Prostate Cancer Diagnosis. *Trends Biotechnol.* **2009**, *27* (12), 661–663.

(37) Kelly, J. G.; Angelov, P. P.; Trevisan, J.; Vlachopoulou, A.; Paraskevaidis, E.; Martin-Hirsch, P. L.; Martin, F. L. Robust Classification of Low-Grade Cervical Cytology Following Analysis with ATR-FTIR Spectroscopy and Subsequent Application of Self-Learning Classifier EClass. *Anal. Bioanal. Chem.* **2010**, *398* (5), 2191–2201.

(38) Holman, H.-Y. N.; Martin, M. C.; Blakely, E. A.; Bjornstad, K.; Mckinney, W. R. IR Spectroscopic Characteristics of Cell Cycle and Cell Death Probed by Synchrotron Radiation Based Fourier Transform IR Spectromicroscopy. *Biopolymers* **2000**, *57* (6), 329–335.

(39) Hammiche, A.; German, M. J.; Hewitt, R.; Pollock, H. M.; Martin, F. L. Monitoring Cell Cycle Distributions in MCF-7 Cells Using Near-Field Photothermal Microspectroscopy. *Biophys. J.* **2005**, *88* (5), 3699–3706.

(40) Boydston-White, S.; Gopen, T.; Houser, S.; Bargonetti, J.; Diem, M. Infrared Spectroscopy of Human Tissue. V. Infrared Spectroscopic Studies of Myeloid Leukemia (ML-1) Cells at Different Phases of the Cell Cycle. *Biospectroscopy* **1999**, *5* (4), 219–227.

(41) Boydston-White, S.; Romeo, M.; Chernenko, T.; Regina, A.; Miljković, M.; Diem, M. Cell-Cycle-Dependent Variations in FTIR Micro-Spectra of Single Proliferating HeLa Cells: Principal Component and Artificial Neural Network Analysis. *Biochim. Biophys. Acta - Biomembr.* **2006**, *1758* (7), 908–914.

(42) Kong, R.; Bhargava, R. Characterization of Porcine Skin as a Model for Human Skin Studies Using Infrared Spectroscopic Imaging. *Analyst* **2011**, *136* (11), 2359–2366.

(43) Kong, R.; Reddy, R. K.; Bhargava, R. Characterization of Tumor Progression in Engineered Tissue Using Infrared Spectroscopic Imaging. *Analyst* **2010**, *135* (7), 1569–1578.

(44) Yamada, K. M.; Cukierman, E. Modeling Tissue Morphogenesis and Cancer in 3D. *Cell* **2007**, *130* (4), 601–610.

(45) Yang, Y.; Sulé-Suso, J.; Sockalingum, G. D.; Kegelaer, G.; Manfait, M.; El Haj, A. J. Study of Tumor Cell Invasion by Fourier Transform Infrared Microspectroscopy. *Biopolymers* **2005**, *78* (6), 311–317.

(46) Hartmann, M.; Hanh, B. D.; Podhaisky, H.; Wensch, J.; Bodzenta, J.; Wartewig, S.; Neubert, R. H. H. A New FTIR-ATR Cell for Drug Diffusion Studies. *Analyst* **2004**, *129* (10), 902–905.

(47) Boncheva, M.; Tay, F. H.; Kazarian, S. G. Application of Attenuated Total Reflection Fourier Transform Infrared Imaging and Tape-Stripping to Investigate the Three-Dimensional Distribution of Exogenous Chemicals and the Molecular Organization in Stratum Corneum. *J. Biomed. Opt.* **2008**, *13* (6), 064009.

(48) Andanson, J.-M.; Chan, K. L. A.; Kazarian, S. G. High-Throughput Spectroscopic Imaging Applied to Permeation through the Skin. *Appl. Spectrosc.* **2009**, *63* (5), 512–517.

(49) Kane, S. R.; Ashby, P. D.; Pruitt, L. A. ATR-FTIR as a Thickness Measurement Technique for Hydrated Polymer-on-Polymer Coatings. *J. Biomed. Mater. Res. Part B Appl. Biomater.* **2009**, *91B* (2), 613–620.

(50) Ribar, T.; Bhargava, R.; Koenig, J. L. FT-IR Imaging of Polymer Dissolution by Solvent Mixtures. 1. Solvents. *Macromolecules* **2000**, *33* (23), 8842–8849.

(51) Percot, A.; Zhu, X. X.; Lafleur, M. A Simple FTIR Spectroscopic Method for the Determination of the Lower Critical Solution Temperature OfN-Isopropylacrylamide Copolymers and Related Hydrogels. *J. Polym. Sci. Part B Polym. Phys.* **2000**, *38* (7), 907–915.

(52) Bhargava, R. Infrared Spectroscopic Imaging: The next Generation. *Appl. Spectrosc.* **2012**, *66* (10), 1091–1120.

(53) Bhargava, R.; Wang, S.; Koenig, J. L. FTIR Microspectroscopy of Polymeric Systems. *Adv. Polym. Sci.* **2003**, *163*, 137–191.

(54) Rao, G. G. N. G.; Karpf, A. External Cavity Tunable Quantum Cascade Lasers and Their Applications to Trace Gas Monitoring. *Appl. Opt.* **2011**, *50* (4), A100--A115.

(55) Reddy, R. R. K. R.; Walsh, M. M. J. M.; Schulmerich, M. V; Carney, P. S.; Bhargava, R. High-Definition Infrared Spectroscopic Imaging. *Appl. Spectrosc.* **2013**, *67* (1), 93–105.

(56) Faist, J.; Capasso, F.; Sivco, D. L.; Sirtori, C.; Hutchinson, A. L.; Cho, A. Y. Quantum Cascade Laser. *Science (80-.).* **1994**, *264* (5158), 553–556.

(57) Luo, G. P.; Peng, C.; Le, H. Q.; Pei, S. S.; Hwang, W.-Y.; Ishaug, B.; Um, J.; Baillargeon, J. N.; Lin, C.-H. Grating-Tuned External-Cavity Quantum-Cascade Semiconductor Lasers. *Appl. Phys. Lett.* **2001**, *78* (19), 2834.

(58) Capasso, F.; Spie, F. High-Performance Midinfrared Quantum Cascade Lasers. *Opt. Eng.* **2010**, *49* (11), 111102.

(59) Wysocki, G.; Curl, R. F.; Tittel, F. K.; Maulini, R.; Bulliard, J. M.; Faist, J.; Physics, A. Widely Tunable Mode-Hop Free External Cavity Quantum Cascade Laser for High Resolution Spectroscopic Applications. *Appl. Phys. B* **2005**, *81* (6), 769–777.

(60) Kosterev, A. A.; Tittel, F. K. Chemical Sensors Based on Quantum Cascade Lasers. *IEEE J. Quantum Electron.* **2002**, *38* (6), 582–591.

(61) Paldus, B. A.; Harb, C. C.; Spence, T. G.; Zare, R. N.; Gmachl, C.; Capasso, F.; Sivco, D. L.; Baillargeon, J. N.; Hutchinson, A. L.; Cho, A. Y. Cavity Ringdown Spectroscopy Using Mid-Infrared Quantum-Cascade Lasers. *Opt. Lett.* **2000**, *25* (9), 666–668.

(62) Kölhed, M.; Haberkorn, M.; Pustogov, V.; Mizaikoff, B.; Frank, J.; Karlberg, B.; Lendl, B. Assessment of Quantum Cascade Lasers as Mid Infrared Light Sources for Measurement of Aqueous Samples. *Vib. Spectrosc.* **2002**, *29* (1–2), 283–289.

(63) Namjou, K.; Cai, S.; Whittaker, E. A.; Faist, J.; Gmachl, C.; Capasso, F.; Sivco, D. L.; Cho, a Y. Sensitive Absorption Spectroscopy with a Room-Temperature Distributed-Feedback Quantum-Cascade Laser. *Opt. Lett.* **1998**, *23* (3), 219–221.

(64) Kole, M. R.; Reddy, R. K.; Schulmerich, M. V; Gelber, M. K.; Bhargava, R. Discrete Frequency Infrared Microspectroscopy and Imaging with a Tunable Quantum Cascade Laser. *Anal. Chem.* **2012**, *84* (23), 10366–10372.

(65) Phillips, M. C.; Ho, N. Infrared Hyperspectral Imaging Using a Broadly Tunable External Cavity Quantum Cascade Laser and Microbolometer Focal Plane Array. *Opt. Express* **2008**, *16* (3), 1836–1845.

(66) Guo, B.; Wang, Y.; Peng, C.; Luo, G. P.; Le, H. Q. Using Semiconductor Lasers. **2003**, *57* (7), 811–822.

(67) Davis, B. J.; Scott Carney, P.; Bhargava, R. Theory of Infrared Microspectroscopy for Intact Fibers. *Anal. Chem.* **2011**, *83* (2), 525–532.

(68) Bhargava, R.; Fernandez, D. C.; Hewitt, S. M.; Levin, I. W. High Throughput Assessment of Cells and Tissues: Bayesian Classification of Spectral Metrics from Infrared Vibrational Spectroscopic Imaging Data. *Biochim. Biophys. Acta* **2006**, *1758* (7), 830–845.

(69) Baker, M. J.; Trevisan, J.; Bassan, P.; Bhargava, R.; Butler, H. J.; Dorling, K. M.; Fielden, P. R.; Fogarty, S. W.; Fullwood, N. J.; Heys, K. a; et al. Using Fourier Transform IR Spectroscopy to Analyze Biological Materials. *Nat. Protoc.* **2014**, *9* (8), 1771–1791.

(70) Paschalis, E. P.; Verdelis, K.; Doty, S. B.; Boskey, a L.; Mendelsohn, R.; Yamauchi, M. Spectroscopic Characterization of Collagen Cross-Links in Bone. *J. Bone Miner. Res.* **2001**, *16* (10), 1821–1828.

(71) Lasch, P.; Haensch, W.; Naumann, D.; Diem, M. Imaging of Colorectal Adenocarcinoma Using FT-IR Microspectroscopy and Cluster Analysis. *Biochim. Biophys. Acta* **2004**, *1688* (2), 176–186.

(72) Matthäus, C.; Boydston-White, S.; Miljković, M.; Romeo, M.; Diem, M. Raman and Infrared Microspectral Imaging of Mitotic Cells. *Appl. Spectrosc.* **2006**, *60* (1), 1–8.

(73) Petibois, C.; Déléris, G. Chemical Mapping of Tumor Progression by FT-IR Imaging: Towards Molecular Histopathology. *Trends Biotechnol.* **2006**, *24* (10), 455–462.

(74) Gazi, E.; Dwyer, J.; Gardner, P.; Ghanbari-Siahkali, a; Wade, a P.; Miyan, J.; Lockyer, N. P.; Vickerman, J. C.; Clarke, N. W.; Shanks, J. H.; et al. Applications of Fourier Transform Infrared Microspectroscopy in Studies of Benign Prostate and Prostate Cancer. A Pilot Study. *J. Pathol.* **2003**, *201* (1), 99–108.

(75) Bhargava, R.; Levin, I. W. *Spectrochemical Analysis Using Infrared Multichannel Detectors*; Sheffield Analytical Chemistry Series; Wiley, 2008.

(76) Hirschmugl, C. J.; Gough, K. M. Fourier Transform Infrared Spectrochemical Imaging: Review of Design and Applications with a Focal Plane Array and Multiple Beam Synchrotron Radiation Source. *Appl. Spectrosc.* **2012**, *66* (5), 475–491.

(77) Kodali, A. K. A.; Schulmerich, M.; Ip, J.; Yen, G.; Cunningham, B. T.; Bhargava, R. Narrowband Midinfrared Reflectance Filters Using Guided Mode Resonance. *Anal. Chem.* **2010**, *82* (13), 5697–5706.

(78) Brandstetter, M.; Koch, C.; Genner, A.; Lendl, B. Measures for Optimizing Pulsed EC-QC Laser Spectroscopy of Liquids and Application to Multi-Analyte Blood Analysis. *SPIE Proc.* **2013**, *8993* (1), 89931U.

(79) Bassan, P.; Weida, M. J.; Rowlette, J.; Gardner, P. Large Scale Infrared Imaging of Tissue Micro Arrays (TMAs) Using a Tunable Quantum Cascade Laser (QCL) Based Microscope. *Analyst* **2014**, *139* (16), 3856–3859.

(80) Yeh, K.; Schulmerich, M.; Bhargava, R. Mid-Infrared Microspectroscopic Imaging with a Quantum Cascade Laser. In *SPIE*; Druy, M. A., Crocombe, R. A., Eds.; 2013; Vol. 8726, p 87260E.

(81) Guo, B.; Wang, Y.; Peng, C.; Luo, G. P.; Le, H. Q. Multi-Wavelength Mid-Infrared Micro-Spectral Imaging Using Semiconductor Lasers. *Appl. Spectrosc.* **2003**, *57* (7), 811–822.

(82) Kröger, N.; Egl, A.; Engel, M.; Gretz, N.; Haase, K.; Herpich, I.; Kränzlin, B.; Neudecker, S.; Pucci, A.; Schönhals, A.; et al. Quantum Cascade Laser-Based Hyperspectral Imaging of Biological Tissue. *J. Biomed.*

Opt. **2014**, *19* (11), 111607.

(83) Cazes, J. *Analytical Instrumentation Handbook*; CRC Press, 2004.

(84) Hoult, R. A.; Ragusa, R. P. Detector Preamplifier for Use with a MCT Detector. US4682022 A, 1987.

(85) Mayerich, D.; Walsh, M. J.; Kadjacsy-Balla, A.; Ray, P. S.; Hewitt, S. M.; Bhargava, R. Stain-Less Staining for Computed Histopathology. *Technology* **2015**, *3* (1), 27–31.

(86) Diem, M.; Griffiths, P. R.; Chalmers, J. M. *Vibrational Spectroscopy for Medical Diagnosis*; Wiley Chichester, 2008; Vol. 40.

(87) Liu, J.-N.; Schulmerich, M. V; Bhargava, R.; Cunningham, B. T. Optimally Designed Narrowband Guided-Mode Resonance Reflectance Filters for Mid-Infrared Spectroscopy. *Opt. Express* **2011**, *19* (24), 24182–24197.

(88) Yeh, K.; Kenkel, S.; Liu, J.-N.; Bhargava, R. Fast Infrared Chemical Imaging with a Quantum Cascade Laser. *Anal. Chem.* **2015**, *87* (1), 485–493.

(89) Pilling, M. J. J.; Gardner, P.; Henderson, A.; Brown, M. D. M. D. M. D.; Bird, B.; Clarke, N. W. W.; Brown, M. D. M. D. M. D.; Clarke, N. W. W.; Gardner, P.; Henderson, A.; et al. High Throughput Quantum Cascade Laser (QCL) Spectral Histopathology : A Practical Approach towards Clinical Translation. *Faraday Discuss.* **2016**, *00* (0), 1–20.

(90) Haase, K.; Kröger-Lui, N.; Pucci, A.; Schönhals, A.; Petrich, W. Real-Time Mid-Infrared Imaging of Living Microorganisms. *J. Biophotonics* **2016**, *9* (1–2), 61–66.

(91) Kröger-Lui, N.; Gretz, N.; Haase, K.; Kränzlin, B.; Neudecker, S.; Pucci, A.; Regenscheit, A.; Schönhals, A.; Petrich, W. Rapid Identification of Goblet Cells in Unstained Colon Thin Sections by Means of Quantum Cascade Laser-Based Infrared Microspectroscopy. *Analyst* **2015**, *140* (7), 2086–2092.

(92) Hu, M.; Yao, J.; Cai, L.; Bachman, K. E.; Van Den Brû Le, F.; Velculescu, V.; Polyak, K. Distinct Epigenetic Changes in the Stromal Cells of Breast Cancers. *Nat. Genet.* **2005**, *37* (8), 899–905.

(93) Hanahan, D.; Coussens, L. M. Accessories to the Crime: Functions of Cells Recruited to the Tumor Microenvironment. *Cancer Cell* **2012**, *21* (3), 309–322.

(94) Finak, G.; Bertos, N.; Pepin, F.; Sadekova, S.; Souleimanova, M.; Zhao, H.; Chen, H.; Omeroglu, G.; Meterissian, S.; Omeroglu, A.; et al. Stromal Gene Expression Predicts Clinical Outcome in Breast Cancer. *Nat. Med.* **2008**, *14* (5), 518–527.

(95) Beck, A. H.; Sangoi, A. R.; Leung, S.; Marinelli, R. J.; Nielsen, T. O.; van de Vijver, M. J.; West, R. B.; van de Rijn, M.; Koller, D. Systematic Analysis of Breast Cancer Morphology Uncovers Stromal Features Associated with Survival. *Sci. Transl. Med.* **2011**, *3* (108), 108ra113-108ra113.

(96) Heijs, B.; Abdelmoula, W. M.; Lou, S.; Bruijn, I. H. B.; Dijkstra, J.; Bovée, J. V. M. G.; McDonnell, L. A.; Briaire-de Bruijn, I. H.; Dijkstra, J.; Bovée, J. V. M. G.; et al. Histology-Guided High-Resolution Matrix-Assisted Laser Desorption Ionization Mass Spectrometry Imaging. *Anal. Chem.* **2015**, *87* (24), 11978–11983.

(97) Chaurand, P.; Schwartz, S. A.; Billheimer, D.; Xu, B. J.; Crecelius, A.; Caprioli, R. M. Integrating Histology and Imaging Mass Spectrometry. *Anal. Chem.* **2004**, *76* (4), 1145–1155.

(98) Cornett, D. S.; Reyzer, M. L.; Chaurand, P.; Caprioli, R. M. MALDI Imaging Mass Spectrometry: Molecular Snapshots of Biochemical Systems. *Nat. Methods* **2007**, *4* (10), 828–833.

(99) Schwamborn, K.; Caprioli, R. M. Molecular Imaging by Mass Spectrometry — Looking beyond Classical Histology. *Nat. Rev. Cancer* **2010**, *10* (9), 639–646.

(100) Calligaris, D.; Caragacianu, D.; Liu, X.; Norton, I.; Thompson, C. J.; Richardson, A. L.; Golshan, M.; Easterling, M. L.; Santagata, S.; Dillon, D. A.; et al. Application of Desorption Electrospray Ionization Mass Spectrometry Imaging in Breast Cancer Margin Analysis. *Proc. Natl. Acad. Sci.* **2014**, *111* (42), 15184–15189.

(101) Baker, M. J.; Faulds, K. Fundamental Developments in Clinical Infrared and Raman Spectroscopy. *Chem. Soc. Rev.* **2016**, *45* (7), 1792–1793.

(102) Greenleaf, J. F.; Bahn, R. C. Clinical Imaging with Transmissive Ultrasonic Computerized Tomography. *IEEE Trans. Biomed. Eng.* **1981**, *BME-28* (2), 177–185.

(103) Orringer, D. A.; Pandian, B.; Niknafs, Y. S.; Hollon, T. C.; Boyle, J.; Lewis, S.; Garrard, M.; Hervey-Jumper, S. L.; Garton, H. J. L.; Maher, C. O.; et al. Rapid Intraoperative Histology of Unprocessed Surgical Specimens via Fibre-Laser-Based Stimulated Raman Scattering Microscopy. *Nat. Biomed. Eng.* **2017**, *1* (2), 27.

(104) Shemonski, N. D.; South, F. a.; Liu, Y.-Z.; Adie, S. G.; Scott Carney, P.; Boppart, S. a.; Carney, P. S.; Boppart, S. a. Computational High-Resolution Optical Imaging of the Living Human Retina. *Nat. Photonics* **2015**, *9* (June), 1–11.

(105) Holton, S. E.; Bergamaschi, A.; Katzenellenbogen, B. S.; Bhargava, R. Integration of Molecular Profiling and Chemical Imaging to Elucidate Fibroblast-Microenvironment Impact on Cancer Cell Phenotype and Endocrine Resistance in Breast Cancer. *PLoS One* **2014**, *9* (5), e96878.

(106) Wald, N.; Bordry, N.; Foukas, P. G.; Speiser, D. E.; Goormaghtigh, E. Identification of Melanoma Cells and Lymphocyte Subpopulations in Lymph Node Metastases by FTIR Imaging Histopathology. *Biochim. Biophys. Acta* **2016**, *1862* (2), 202–212.

(107) Benard, A.; Desmedt, C.; Smolina, M.; Szternfeld, P.; Verdonck, M.; Rouas, G.; Kheddoumi, N.; Rothé, F.; Larsimont, D.; Sotiriou, C.; et al. Infrared Imaging in Breast Cancer: Automated Tissue Component Recognition and Spectral Characterization of Breast Cancer Cells as Well as the Tumor Microenvironment. *Analyst* **2014**, *139* (5), 1044–1056.

(108) Mayerich, D.; Walsh, M.; Schulmerich, M.; Bhargava, R. Real-Time Interactive Data Mining for Chemical Imaging Information: Application to Automated Histopathology. *BMC Bioinformatics* **2013**, *14*, 156.

(109) Suhalim, J. L.; Boik, J. C.; Tromberg, B. J.; Potma, E. O. The Need for Speed. *J. Biophotonics* **2012**, *5* (5–6), 387–395.

(110) Kwak, J. T.; Kajdacsy-Balla, A.; Macias, V.; Walsh, M.; Sinha, S.; Bhargava, R. Improving Prediction of Prostate Cancer Recurrence Using Chemical Imaging. *Sci. Rep.* **2015**, *5*, 8758.

(111) Fabian, H.; Thi, N. A. N.; Eiden, M.; Lasch, P.; Schmitt, J.; Naumann, D. Diagnosing Benign and Malignant Lesions in Breast Tissue Sections by Using IR-Microspectroscopy. *Biochim. Biophys. Acta* **2006**, *1758* (7), 874–882.

(112) Verdonck, M.; Wald, N.; Janssis, J.; Yan, P.; Meyer, C.; Legat, A.; Speiser, D. E.; Desmedt, C.; Larsimont, D.; Sotiriou, C.; et al. Breast Cancer and Melanoma Cell Line Identification by FTIR Imaging after Formalin-Fixation and Paraffin-Embedding. *Analyst* **2013**, *138* (14), 4083–4091.

(113) Fabian, H.; Lasch, P.; Boese, M.; Haensch, W. Infrared Microspectroscopic Imaging of Benign Breast Tumor Tissue Sections. *J. Mol. Struct.* **2003**, *661–662* (1–3), 411–417.

(114) Tian, P.; Zhang, W.; Zhao, H.; Lei, Y.; Cui, L.; Wang, W.; Li, Q.; Zhu, Q.; Zhang, Y.; Xu, Z. Intraoperative Diagnosis of Benign and Malignant Breast Tissues by Fourier Transform Infrared Spectroscopy and Support Vector Machine Classification. *Int. J. Clin. Exp. Med.* **2015**, *8* (1), 972–981.

(115) Gao, T.; Feng, J.; Ci, Y. Human Breast Carcinomal Tissues Display Distinctive FTIR Spectra: Implication for the Histological Characterization of Carcinomas. *Anal. Cell. Pathol.* **1999**, *18*, 87–93.

(116) Kumar, S.; Desmedt, C.; Larsimont, D.; Sotiriou, C.; Goormaghtigh, E. Change in the Microenvironment of Breast Cancer Studied by FTIR Imaging. *Analyst* **2013**, *138* (14), 4058–4065.

(117) Bai, Y.; Slivken, S.; Kuboya, S.; Darvish, S. R.; Razeghi, M. Quantum Cascade Lasers That Emit More Light than Heat. *Nat. Photonics* **2010**, *4* (2), 99–102.

(118) Yao, Y.; Hoffman, A. J. A. A. J.; Gmachl, C. F. C. Mid-Infrared Quantum Cascade Lasers. *Nat. Photonics* **2012**, *6* (June), 432–439.

(119) Kröger, N.; Egl, A.; Engel, M.; Gretz, N.; Haase, K.; Herpich, I.; Kränzlin, B.; Neudecker, S.; Pucci, A.; Schönhals, A.; et al. Quantum Cascade Laser–Based Hyperspectral Imaging of Biological Tissue. *J. Biomed. Opt.* **2014**, *19* (11), 111607.

(120) Tiwari, S.; Raman, J.; Reddy, V.; Ghetler, A.; Tella, R. P.; Han, Y.; Moon, C. R.; Hoke, C. D.; Bhargava, R. Towards Translation of Discrete Frequency Infrared Spectroscopic Imaging for Digital Histopathology of Clinical Biopsy Samples. *Anal. Chem.* **2016**, *88* (20), 10183–10190.

(121) Pilling, M. J.; Henderson, A.; Gardner, P. Quantum Cascade Laser Spectral Histopathology: Breast Cancer Diagnostics Using High Throughput Chemical Imaging. *Anal. Chem.* **2017**, *89* (14), 7348–7355.

(122) Hughes, C.; Clemens, G.; Bird, B.; Dawson, T.; Ashton, K. M.; Jenkinson, M. D.; Brodbelt, A.; Weida, M.; Fotheringham, E.; Barre, M.; et al. Introducing Discrete Frequency Infrared Technology for High-Throughput Biofluid Screening. *Sci. Rep.* **2016**, *6* (February).

(123) Sage, D.; Donati, L.; Soulez, F.; Fortun, D.; Schmit, G.; Seitz, A.; Guiet, R.; Vonesch, C.; Unser, M. DeconvolutionLab2 : An Open-Source Software for Deconvolution Microscopy. *Methods* **2017**.

(124) Mittal, S.; Yeh, K.; Leslie, L. S.; Kenkel, S.; Kajdacsy-Balla, A.; Bhargava, R. Simultaneous Cancer and Tumor Microenvironment Subtyping Using Confocal Infrared Microscopy for All-Digital Molecular Histopathology. *Proc. Natl. Acad. Sci.* **2018**, *115* (25), E5651–E5660.

(125) ur Rehman, I.; Movasaghi, Z.; Rehman, S. *Vibrational Spectroscopy for Tissue Analysis*; CRC Press, 2012.

(126) Leslie, L. S.; Wrobel, T. P.; Mayerich, D.; Bindra, S.; Emmadi, R.; Bhargava, R. High Definition Infrared Spectroscopic Imaging for Lymph Node Histopathology. *PLoS One* **2015**, *10* (6), e0127238.

(127) Elmore, J. G.; Longton, G. M.; Carney, P. A.; Geller, B. M.; Onega, T.; Tosteson, A. N. A.; Nelson, H. D.; Pepe, M. S.; Allison, K. H.; Schnitt, S. J.; et al. Diagnostic Concordance Among Pathologists Interpreting Breast Biopsy Specimens. *JAMA* **2015**, *313* (11), 1122–1132.

(128) Huang, M. L.; Hess, K.; Candelaria, R. P.; Eghtedari, M.; Adrada, B. E.; Sneige, N.; Fornage, B. D. Comparison of the Accuracy of US-Guided Biopsy of Breast Masses Performed with 14-Gauge, 16-Gauge and 18-Gauge Automated Cutting Needle Biopsy Devices, and Review of the Literature. *Eur. Radiol.* **2016**, 1–6.

(129) Wrobel, T. P.; Kole, M. R.; Bhargava, R. Emerging Trends and Opportunities in Discrete Frequency Infrared and Raman Spectroscopic Imaging. *Spectroscopy* **2016**, *31* (13), 1–19.

(130) Wrobel, T. P.; Bhargava, R. Infrared Spectroscopic Imaging Advances as an Analytical Technology for Biomedical Sciences. *Anal. Chem.* **2018**, *90* (3), 1444–1463.

(131) Tiwari, S.; Reddy, V. B.; Bhargava, R.; Raman, J. Computational Chemical Imaging for Cardiovascular Pathology: Chemical Microscopic Imaging Accurately Determines Cardiac Transplant Rejection. *PLoS One* **2015**, *10* (5), e0125183.

(132) Kuepper, C.; Kallenbach-Thieltges, A.; Juette, H.; Tannapfel, A.; Großerueschkamp, F.; Gerwert, K. Quantum Cascade Laser-Based Infrared Microscopy for Label-Free and Automated Cancer Classification in Tissue Sections. *Sci. Rep.* **2018**, *8* (1), 7717.

(133) Bassan, P.; Sachdeva, A.; Kohler, A.; Hughes, C.; Henderson, A.; Boyle, J.; Shanks, J. H.; Brown, M.; Clarke, N. W.; Gardner, P. FTIR Microscopy of Biological Cells and Tissue: Data Analysis Using Resonant Mie Scattering (RMieS) EMSC Algorithm. *Analyst* **2012**, *137* (6), 1370–1377.

(134) Bambery, K. R.; Wood, B. R.; McNaughton, D. Resonant Mie Scattering (RMieS) Correction Applied to FTIR Images of Biological Tissue Samples. *Analyst* **2012**, *137* (1), 126–132.

(135) Schönhals, A.; Kröger-Lui, N.; Pucci, A.; Petrich, W. On the Role of Interference in Laser-Based Mid-Infrared Widefield Microspectroscopy. *J. Biophotonics* **2018**, No. March, 1–7.

(136) Ran, S.; Berisha, S.; Mankar, R.; Shih, W.-C.; Mayerich, D. Mitigating Fringing in Discrete Frequency Infrared Imaging Using Time-Delayed Integration. *Biomed. Opt. Express* **2018**, *9* (2), 832.

(137) Yeh, K.; Bhargava, R. Discrete Frequency Infrared Imaging Using Quantum Cascade Lasers for Biological Tissue Analysis. In *SPIE*; Mahadevan-Jansen, A., Petrich, W., Eds.; 2016; Vol. 9074, p 970406.

(138) Lu, F.; Jin, M.; Belkin, M. a. Tip-Enhanced Infrared Nanospectroscopy via Molecular Expansion Force Detection. *Nat. Photonics* **2014**, *8* (4), 307–312.

(139) Kenkel, S.; Mittal, A.; Mittal, S.; Bhargava, R. Probe-Sample Interaction-Independent Atomic Force Microscopy-Infrared Spectroscopy: Toward Robust Nanoscale Compositional Mapping. *Anal. Chem.* **2018**, *90* (15), 8845–8855.

(140) Dazzi, A.; Glotin, F.; Carminati, R. Theory of Infrared Nanospectroscopy by Photothermal Induced Resonance. *J. Appl. Phys.* **2010**, *107* (12), 124519.

(141) Ramer, G.; Aksyuk, V. A.; Centrone, A. Quantitative Chemical Analysis at the Nanoscale Using the Photothermal Induced Resonance Technique. *Anal. Chem.* **2017**, *89* (24), 13524–13531.

(142) Pleitez, M. A.; Lieblein, T.; Bauer, A.; Hertzberg, O.; von Lilienfeld-Toal, H.; Mäntele, W. In Vivo Noninvasive Monitoring of Glucose Concentration in Human Epidermis by Mid-Infrared Pulsed Photoacoustic Spectroscopy. *Anal. Chem.* **2013**, *85* (2), 1013–1020.

(143) Zhang, D.; Li, C.; Zhang, C.; Slipchenko, M. N.; Eakins, G.; Cheng, J. X. Depth-Resolved Mid-Infrared Photothermal Imaging of Living Cells and Organisms with Submicrometer Spatial Resolution. *Sci. Adv.* **2016**, *2* (9), 1–8.

(144) Erer, T. H. B.; Randstetter, M. A. B.; Ochreiner, A. R. H.; Anger, G. R. L.; Ärzinger, W. O. M.; Urgholzer, P. E. B.; Endl, B. E. L.; Berer, T.; Brandstetter, M.; Hochreiner, A.; et al. Remote Mid-Infrared Photoacoustic Spectroscopy with a Quantum Cascade Laser. *Opt. Lett.* **2015**, *40* (15), 3476.

(145) Tiwari, S.; Raman, J.; Reddy, V.; Dawson, M.; Bhargava, R. Translation of Infrared Chemical Imaging for Cardiovascular Evaluation. *Prog. Biomed. Opt. Imaging - Proc. SPIE* **2016**, *9704*.

(146) Lambrechts, P.; Boerlage, M.; Steinbuch, M. Trajectory Planning and Feedforward Design for Electromechanical Motion Systems. *Control Eng. Pract.* **2005**, *13* (2), 145–157.

(147) Mayerich, D.; van Dijk, T.; Walsh, M. J.; Schulmerich, M. V.; Scott Carney, P.; Bhargava, R.; Carney, P. S.; Bhargava, R. On the Importance of Image Formation Optics in the Design of Infrared Spectroscopic Imaging Systems. *Analyst* **2014**, *139* (16), 4031–4036.

(148) Jágerská, J.; Jouy, P.; Tuzson, B.; Looser, H.; Hugi, A.; Mangold, M.; Soltic, P.; Faist, J.; Emmenegger, L. Multi-Color Laser Spectroscopy with a Dual-Wavelength Quantum Cascade Laser. *CLEO 2014* **2014**, No. 2, 3–4.

(149) Jouy, P.; Bonetti, Y.; Hans, K.; Gianella, M.; Sigrist, M. W.; Mangold, M.; Tuzson, B.; Emmenegger, L.; Wagli, P.; Homsy, A.; et al. Multi-Wavelength QCL Based MIR Spectroscopy for Fluids and Gases. *2013 Conf. Lasers Electro-Optics* **2013**, 2 pp.-2 pp.

(150) Gmachl, C.; Sivco, D. L.; Baillargeon, J. N.; Hutchinson, A. L.; Capasso, F.; Cho, A. Y. Quantum Cascade Lasers with a Heterogeneous Cascade: Two-Wavelength Operation. *Appl. Phys. Lett.* **2001**, *79* (5), 572–574.

(151) Rauter, P.; Capasso, F. Multi-Wavelength Quantum Cascade Laser Arrays. *Laser Photonics Rev.* **2015**, *9* (5), 452–477.

(152) Schnell, M.; Carney, P. S.; Hillenbrand, R. Synthetic Optical Holography for Rapid Nanoimaging. *Nat. Commun.* **2014**, *5*, 1–10.

(153) Yeh, K.; Lee, D.; Bhargava, R. Multicolor Discrete Frequency Infrared Spectroscopic Imaging. *Anal. Chem.* **2019**, *91* (3), 2177–2185.